Cavity Optics in Organic Semiconductors: From Light-Extraction of OLEDs to Exciton-Polaritons

by

Yue Qu

A dissertation submitted in partial fulfillment
of the requirements for the degree of
Doctor of Philosophy
(Electrical Engineering)
in the University of Michigan
2020

Doctoral Committee:

Professor Stephen R. Forrest, Chair
Associate Professor Hui Deng
Assistant Professor Parag B. Deotare
Professor Mackillo Kira

Yue Qu

quyue@umich.edu

ORCID ID: 0000-0001-9645-7483

To my grandfather

To my parents

To Jingshu

Acknowledgements

This dissertation could not have been accomplished without the mentorship and support from many people. I am humbly grateful to the people who helped me along the journey as a researcher to this dissertation.

First, I acknowledge my thesis advisor, Prof. Stephen R. Forrest, for his intellectual and financial support. Throughout my time in graduate school, Prof. Forrest inspired me with his exceptional insight, passion and dedication to perfection. I am also grateful to his trust, encouragement and patience, which help me overcome difficulties in my graduate school.

Also, I feel extremely lucky to work with the remarkable group of lab mates, from whom I learned so much. I am particularly thankful to Michael Slootsky as my mentor, who carefully trained me and introduced me to nanofabrication and device modeling, and to Yifan Zhang and Jaesang Lee, who taught me how to grow and test devices. I owe thanks to Anurag Panda, Xiao Liu, Quinn Burlingame, Caleb Coburn and Dejiu Fan, with whom the conversations often led to insights and creative ideas. I also thank Jongchan Kim and Xiaheng Huang for the great experience in working together as a team on OLED outcoupling; Shaocong Hou and Kan Ding, without whom I doubt the work on exciton-polaritons would have been possible; Yongxi Li and Xiaozhou Che for graciously involving me in their work and sharing insights on OPV. My thanks also goes to other OCMers for the enjoyable time we spent in the lab and beyond: Kyusang, Xin, Kevin, Olga, Byeongseop, Qi, Byungjun, Boning, Chanho, Xinjing, Jeff, Claire,

Hafiz and ones I forgot to mention. A special mention goes to Eva Ruff, who helped me untangle administrative issues, making my research and personal life easier than it should be.

Most importantly, my family has been an unendingly source of support and love during my journey up to this point. I am grateful to Jingshu who has been a constant inspiration during my graduate school. My thanks to my recent passed grandfather, to my parents and to Jingshu for their love, sacrifice and care. Without support from them, this work certainly would not have been accomplished. Therefore, my dissertation is dedicated to them.

Table of Contents

List of Tables

.

List of Figures

Abstract

Organic optoelectronics has been an active topic of research and development over the past decades. While organic photovoltaic cells, transistors and other organic electronics are still in transition to commercialization, organic light-emitting devices have revolutionized displays of mobile phones and TVs. Due to the intrinsic properties of organic materials, electron-hole pairs, called excitons, are responsible for optical transitions and, thus, are crucial to organic optoelectronics. Understanding exciton-photon interactions and managing photons are critical to high performance light-emitting devices. This thesis aims at understanding this topic and providing potential solutions.

The first part of this thesis focuses on the optical power distribution in organic light-emitting diodes and providing practical solutions to the limited light-extraction efficiencies. We begin by reviewing the operation and optics of light-emitting devices and modeling methods for device optics. Based on our calculations, we identify the problem of extracting light trapped in high refractive index regions of the devices, and propose principles of designs for light-extraction structures. Different light-extraction methods are demonstrated for both bottom and top-emitting devices.

The second part of the thesis deals with the physics and application of the strong coupling of exciton and photons in organic semiconductors. A new particle, called the exciton-polariton, emerges as a result from the strong coupling between Frenkel excitons in organic materials and photons. We review the progress of organic exciton-polariton research in the topic of polariton

lasing and long-range transport. We demonstrate the polariton laser threshold dependence on temperature and on amplified spontaneous emission. Additionally, we show Frenkel excitons in an amorphous organic film couple with Bloch surface wave. The coupling strength reaches the ultra-strong coupling regime by controlling the organic film thickness. The propagation of the exciton-polaritons with different coupling strengths shows that the more photonic fraction results in longer transport.

Chapter 1

Introduction

Optoelectronic devices convert energy or signals between optical and electrical forms. They are prevalent in our daily life and cutting-edge scientific research. While most optoelectronic devices in commercial products are made of inorganic materials, organic optoelectronics have unique advantages due to the intrinsic properties of organic semiconductors. Among them, organic light-emitting diodes (OLEDs) are the most successful in commercialization, which can be widely found in mobile phones nowadays. Other organic optoelectronic devices are still in research and development or in the early stage of commercialization, such as organic photovoltaics (OPVs), organic thin film transistors, and organic semiconductor lasers.

This thesis focuses on the exciton-photon interactions in organic semiconductors. In this chapter, we review the fundamental physics of organic semiconductors required to understand the topic of this dissertation.

1.1 Solid classification

According to the type of bonding interactions between the constituent blocks, solids are classified as covalent, ionic metallic or molecular. The majority of organic solids belong to the last class, whose building blocks are carbon-based molecules. Within a single molecule, all atoms are held together through covalent bonds. Between molecules, they are held together

through van der Waals forces, which are considerably weaker than covalent or ionic bonds. [1,2] Therefore, organic materials have unique mechanical, optical and electronic properties compared with the covalent solids, such as silicon (Si), germanium, and other inorganic semiconductors, as shown in Table 1.1. For example, due to the low bonding strength and the resulting amorphous structure, organic solids are softer and less rigid than inorganic solids, which allows organic optoelectronics to be curved, flexible, and even stretchable. [3]

Table 1.1 A comparison of bulk physical properties between inorganic and organic semiconductors

Property	**Inorganics**	**Organics**
Bond type	Covalent/Ionic	Van der Waals
Charge Transport	Band Transport	Polaron Hopping
Charge Mobility	~1000 $cm^2/V \cdot s$	<1 $cm^2/V \cdot s$
Dielectric Constant	~10	~3-4
Exciton Species	Wannier-Mott	Frenkel
Exciton Binding Energy	~1-10meV	~0.1-1eV
Exciton Radius	~10nm	~1nm
Hardness	Hard	Soft

Organic materials can be further categorized into three different types: small molecules, polymers and biological. Small molecules have well-defined molecular weight. They can consist of a single unit, called monomers, or a well-defined number of repeat units, called oligomers [2]. If the organic molecule consists of many monomers or oligomers and its chain length is

indefinite, the molecule is known as a polymer. The term *organic semiconductor* usually refers to small molecules and polymers, since they both have been used as the active materials in optoelectronic and electronic devices. Because this thesis focuses on small molecule organic semiconductors, we will use organic materials, for short in the rest of this dissertation.

1.2 Electronic structures in organic semiconductors

1.2.1 Van der Waals force

Different from the covalent bond which is formed by shared electrons between atoms, van der Waals forces originate from dipole interactions [4,5] without forming new electron orbitals between molecules. This force is classified into three different cases: fixed dipole-fixed dipole, dipole-induced dipole and induced dipole-induced dipole interactions. The induced dipole arises from countering a fixed dipole nearby or from fluctuations of the electronic distribution within a molecule. All these three forces are attractive and the interaction energy falls off as $1/r^6$, where r is the distance between the molecular dipoles. Considering the repulsion of the electronic orbitals due to Pauli exclusion, the system can be approximated using a Lennard-Jones potential:

$$U(r) = 4\varepsilon\left[\left(\frac{\sigma}{r}\right)^{12} - \left(\frac{\sigma}{r}\right)^{6}\right] \tag{1.1}$$

where σ is the particle distance at equilibrium and ε corresponds to the attraction strength.

1.2.2 Intra-molecular bonding

Within an organic molecule, the atoms are bonded by covalent bonds through the shared electron orbitals. The interactions between atom levels cause an energy splitting in the new system, resulting in bonding and anti-bonding molecular orbitals, as shown in Fig. 1.1. In the ground state of a stable closed-shell molecule, the bonding orbitals are filled with two electrons

while the anti-bonds remain empty. In the molecules, there are two types of covalent bonds: σ bonds and π bonds. An σ bond can be formed between *s* or *p* atomic orbitals in the head-on geometry, which is symmetric around the axis between two nuclei. A π bond is formed through *p* orbitals interacting side-by-side. The σ bonds are stronger than the π bonds. Usually σ bonds provide a delocalized electron cloud shared by conjugated atoms within the molecule. Since the σ molecular orbital and the corresponding anti-bonding have typically less energy splitting, they are usually the frontier orbitals in organic molecules.

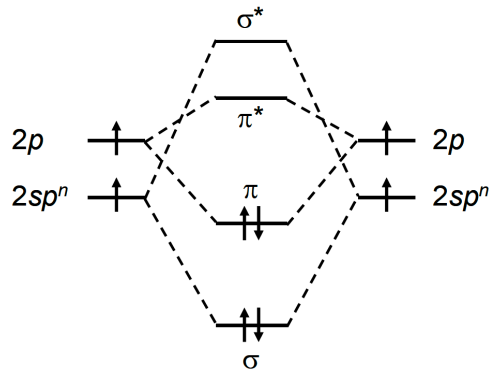

Figure 1.1 Formation of σ and π molecular orbitals and the corresponding anti-bonds σ* and π*, formed from the atomic orbitals of two adjacent atoms.

1.2.3 Molecular orbital energy

Due to the weak intermolecular interactions and the random orientation of molecules, electronic energy levels and the optical transitions of organic solids retain characteristics of individual molecules. For energy levels, organic semiconductors have discrete orbitals with a relatively narrow bandwidth. In contrast, crystalline inorganic semiconductors exhibit a band gap energy between the continuous conduction and valence bands. Both conduction and valence bands have large bandwidths, on the order of several electron volts.

Among all the orbitals filled with electrons, the one with the highest energy is called highest occupied molecular orbital (HOMO). Similarly, the one has the lowest energy among all the empty orbitals is called lowest unoccupied molecular orbital (LUMO). The deeper orbitals are denoted as HOMO-*i* and LUMO+*i* states, as shown in Fig. 1.2. The frontier molecular orbitals of organic semiconductors refer to the HOMO and LUMO. The forbidden gap between HOMO and LUMO is defined as an energy gap. The frontier orbitals play an important role in the optical and electrical properties of organic semiconductors, since they are related to the energies of injected charges and the excitons. As mentioned above, the frontier molecular orbitals are usually π bonds.

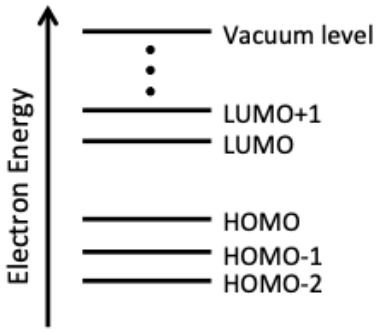

Figure 1.2 Organic molecule orbital energies. Orbitals are measured from the vacuum level. The HOMO and LUMO are analogous to the valence and conduction bands of inorganic semiconductors.

When an electron is added or removed from the charge-neutral molecule, this molecule becomes an anion or cation, respectively. The charged molecule undergoes a geometric distortion to reach a new equilibrium in the new electronic manifold. The average intermolecular distance may also change due to polarization of the surroundings. Thus, the charged molecules are strongly coupled with lattice distortion or phonons, which forms a new quantum quasi-particle called a polaron. For simplicity in the rest of this thesis, hole and electrons refer to the positive and negative polarons, respectively.

Due to the weak van der Waals force, organic semiconductors have limited electron interactions between molecules. Considering the strong lattice distortion surrounding the charged molecules, charges in organic semiconductors are self-trapped and highly localized on each molecule. Charge transport between molecules generally is hopping-like and thermally assisted. Thus, the charge mobility in amorphous organic solids is temperature dependent. At room temperature, the mobility in organic semiconductors can be many orders of magnitude lower than that of crystalline inorganic counterparts. For example, the electron mobility in Si is <1400 $cm^2/V \cdot s$ while in the amorphous Bathophenanthroline (BPhen), commonly used as an electron transport material, the mobility is 6×10^{-4} $cm^2/V \cdot s$. Crystalline organic films have higher charge mobility than amorphous ones because of their developed bands. For crystalline Anthracene, electron mobility is 3 $cm^2/V \cdot s$. [6]

1.3 Excitons in organic semiconductors

1.3.1 Excitons: definition and types

When an electron is excited to the LUMO, a hole is left in the HOMO. The electron-hole pair bound through Coulomb force is called an exciton. The excitons in organic semiconductors are commonly Frenkel excitons which have a high binding energy and small a radius (Table 1.1). Frenkel excitons are usually localized on single molecules. In contrast, inorganic semiconductors commonly have Wannier-Mott (WM) excitons with a radius that is large compared to the lattice constant. They have rather small binding energy on the order of tens of milli-electron volts. Thus, WM excitons are usually only stable at low temperature or in special energetic structures such as quantum wells. A charge transfer (CT) exciton forms where the hole and electron sit on different but nearby molecules or lattice sites when the Coulomb interaction between nearest

neighbors is sufficient. The schematic presentation of three types of excitons is shown in Fig. 1.3.

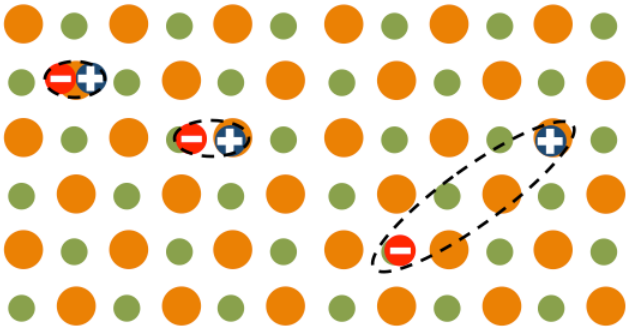

Figure 1.3 A schematic presentation of the three types of excitons: (from left to right) localized Frenkel exciton, intermediate charge-transfer exciton, and extended Wannier-Mott exciton. The green and orange dots denote the lattice sites, which can be molecules in organic semiconductors or atoms in inorganic semiconductors.

1.3.2 The Born-Oppenheimer approximation

The energy of an exciton relative to the ground state can be calculated using the single electron Hamiltonian. However, even the simplest molecules are too complex for analytic solution. Most molecular physics relies on the Born-Oppenheimer approximation: the electronic motion can be separated from that of the nuclei. The different nuclear arrangements contribute to different potential energies. Thus, we hold the nuclear position fixed and solve for the electron energy in a static potential. This allows us to construct a molecular potential energy surface as a function of configuration coordinates. The potential energy of a polyatomic molecule can be too complex to create a multidimensional potential plot. A simplified model of the anharmonic Morse potential of a diatomic molecule can give us a qualitative intuition, as shown in Fig. 1.4. Near the energy minimum, the potential line is approximately harmonic, resulting in a series of discrete vibrational energy states with equal energy gaps between them.

The analog of the Born-Oppenheimer approximation in optical transition is the Franck-Condon principle. It states that electronic transitions occur in a stationary nuclear framework. Thus, the nuclear configuration of a molecule is unchanged during the absorption or emission of a photon. As shown in Fig. 1.4, the transition arrow must be vertical during optical transitions. After the electronic transition, the molecule will relax and obtain its equilibrium nuclear configuration within the electronic manifold. As a result, the optical transition always occurs from the ground vibrational state (v = 0), which is called Kasha's rule. Therefore, the relative possibilities of transitions are not only proportional to the magnitudes of the electronic transition dipole moment between the initial and final electronic states, but also the overlap of the two vibrational modes in their respective electronic states.

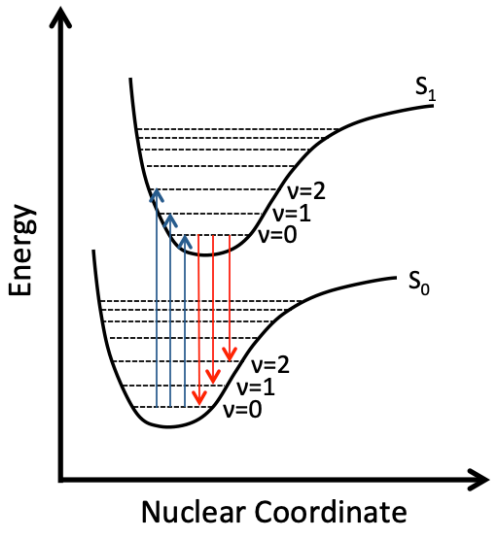

Figure 1.4 Ground state (S_0) and excited state (S_1) energies in the molecular configuration coordinate.

1.3.3 Spin

Electrons are Fermions with spin angular momentum s = ½. Depending on the symmetry of the spin wave functions, excitons can be either spin antisymmetric singlets or symmetric triplets. The total wave function of an exciton is the product of the spin and spatial wave

functions. The Pauli principle states that the total wavefunction must be antisymmetric with respect to the interchange of any pair of electrons. Thus, the spatial and spin wavefunctions must have opposite symmetry. Thus, the singlet spatial wavefunction ψ_s is symmetric and the triplet spatial wavefunction ψ_T is antisymmetric:

$$\psi_S = \frac{1}{\sqrt{2}}[\varphi_1(1)\varphi_2(2) + \varphi_1(2)\varphi_2(1)] \tag{1.2}$$

$$\psi_T = \frac{1}{\sqrt{2}}[\varphi_1(1)\varphi_2(2) - \varphi_1(2)\varphi_2(1)] \tag{1.3}$$

where φ_1 and φ_2 are the wavefunctions for the HOMO and LUMO, respectively, 1 and 2 in the parentheses are indices for the two electrons. The energies of the two states ca n be calculated:

$$E_S = \frac{e^2}{4\pi\varepsilon_0}\left\langle \psi_S \left| \frac{1}{r_{12}} \right| \psi_S \right\rangle = J + K \tag{1.4}$$

$$E_T = \frac{e^2}{4\pi\varepsilon_0}\left\langle \psi_T \left| \frac{1}{r_{12}} \right| \psi_T \right\rangle = J - K \tag{1.5}$$

where J and K are the Coulomb and exchange energies:

$$J = \frac{e^2}{4\pi\varepsilon_0}\left\langle \varphi_1(1)\varphi_2(2) \left| \frac{1}{r_{12}} \right| \varphi_1(1)\varphi_2(2) \right\rangle \tag{1.6}$$

$$K = \frac{e^2}{4\pi\varepsilon_0}\left\langle \varphi_1(1)\varphi_2(2) \left| \frac{1}{r_{12}} \right| \varphi_1(2)\varphi_2(1) \right\rangle \tag{1.7}$$

The triplet state is lower in energy than the singlet state by twice the exchange energy, as shown in Fig. 1.4.

1.3.4 Radiative transitions

According to the Pauli exclusion principle, electrons are disallowed from occupying the same quantum state at the same time. Because most organic molecules in the ground state have a fully occupied outer orbital, it requires the pairs of electrons in the ground state to possess different spins, resulting in zero net spin. Since the optical transition only occurs between

wavefunctions of similar spatial symmetry, this indicates that the exciton and ground state must have the same spin symmetry. Thus, the probabilities of the optical transitions between the ground state and the excited state are proportional to the magnitude of the dipole moment between the initial and final electronic states, the overlap of the two vibrational modes in their respective electronic states, and the conservation of the spin. However, an important exception to this selection rule occurs in the presence of spin-orbit coupling.

Photon absorption usually results in singlet excitons due to the selection rule. The excitons quickly relax to the vibrational ground state ($\sim 10^{12}$ s^{-1}, $v = 0$). The spin-disallowed non-radiative transition between the singlet and triplet is called intersystem crossing (ISC). The transition rate is usually slow and does not significantly impact the singlet emission in a fluorescent system. The ISC rate can be increased as spin-orbit coupling is enhanced within the molecule, mixing the singlet-triplet character.

Photon emission from excited singlet state is called fluorescence. The decay is rapid with a radiative rate $k_r \sim 10^9$ s^{-1}. Although triplet to singlet transitions are forbidden under the processes described above, certain second order effects may mix singlet and triplet, such as spin-orbit coupling, resulting in the radiative decay of a triplet to be weakly allowed. [7–9] Photon emission from triplets is called phosphorescence with a radiative rate $k'_r < 10^6$ s^{-1}.

1.3.5 Non-radiative transitions

Similar to the vibrational modes mentioned above, any molecule or lattice geometric distortion may introduce energy levels additional to ones demonstrated in Fig. 1.4, such as σ bond rotational modes. The non-radiative transition converts electronic energy into phonons through these energy levels. Thus, the non-radiative rate (k_{nr}) heavily depends on the geometric structures of molecules and their vibrational and rotational modes. Intuitively, we may present

non-radiative decay as Fig. 1.5, competing against the radiative rate. This leads to the definition of luminescence quantum yield:

$$\phi = \frac{k_r}{k_r + k_{nr}} \tag{1.8}$$

When the non-radiative decay rate is large enough to be comparable with the radiative decay, the possibility of an exciton generating a photon is reduced. Since low temperature can slow molecular vibrations, the non-radiative decay rate can be modulated, leading molecules to have higher quantum yields at cryogenic temperatures.

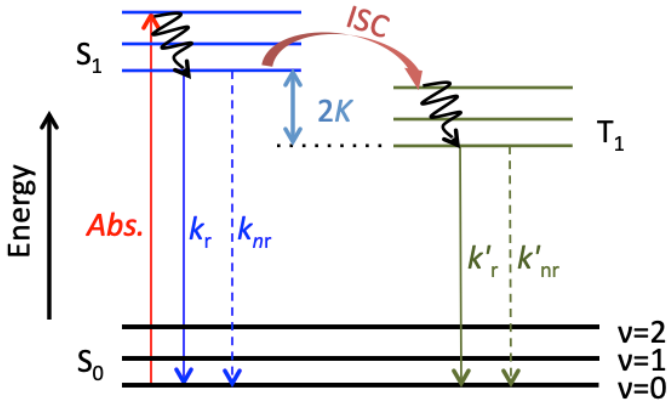

Figure 1.5 Jablonski diagram showing radiative and non-radiative transitions. Absorption occurs from the ground state to singlet state. The exciton relaxes to its vibrational ground state. The molecule can further decay to the ground state radiatively (fluorescence, k_r), non-radiatively (k_{nr}), or become a triplet through intersystem crossing (ISC). Emission (phosphorescence) or non-radiative relaxation proceeds from the triplet-excited state.

1.4 Exciton-photon interactions

The interaction between excitons and photons is ubiquitous in optoelectronics, such as light-emitting diodes (LED) and lasers. Several phenomena occur depending on coupling levels, such as modification of the radiative emission rate from dipoles (called Purcell effect), [10] or generation of new quantum states called polaritons. In the following two sections, we will discuss the interactions between excitons and photons.

1.4.1 Spontaneous emission near interfaces

In the weak-coupling regime, the two oscillators, photons and excitons, interact in a perturbative regime. Nevertheless, the radiative decay rate and the emitting optical power distribution from the excitons can be strongly modified. The probability of spontaneous emission of an exciton can be estimated using Fermi's golden rule:

$$k_r = \frac{2\pi}{\hbar}|\langle\psi_f|\vec{\boldsymbol{d}}\cdot\vec{\boldsymbol{E}}|\psi_i\rangle|^2\rho_{ph} \propto E^2\rho_{ph}|\langle\chi_f|\chi_i\rangle|^2|\langle\varphi_f|\hat{d}|\varphi_i\rangle|^2|\langle\phi_f|\phi_i\rangle|^2 \qquad (1.9)$$

where χ, φ and ϕ are electron spin, electronic and nuclei spatial wavefunctions of the final (subscript *f*) and initial (subscript *i*) states, *E* is the electric field amplitude of a photon, and ρ_{ph} is the photonic mode density (PMD). As the emitter surroundings change, both electric field amplitude and PMD varies. Then the radiative rate can be either enhanced or suppressed as expressed in Eq. 1.9, resulting in a shorter or longer exciton lifetime. Since the non-radiative rate is unchanged with the surrounding, the exciton lifetime can be modulated more effectively for an emitter with a high quantum yield.

There are two main ways to view the PMD: firstly, as vacuum fluctuations, which is an essentially quantum-mechanical [11,12]; secondly, through the ability of the structure surrounding the emitter to support the emitted electromagnetic modes, which is a classical viewpoint. [13] Both views provide the same quantitative answers to the same problems [14] since the quantum treatment of light is only different from the classical model in the predictions on the statistical property of the optical field.

Optical power distributions and the Purcell effect are important to understand the physics of organic light emitting devices (OLEDs), which are related to the light-extraction efficiency and the exciton dynamics. The detailed model using Eq. 1.9 and its application in OLEDs will be the main theme of the first part of this thesis.

1.4.2 Exciton-polaritons

When excitons sit inside a cavity in the strong coupling regime, the energy may oscillate between two states, an excited emitter with an empty cavity mode and an emitter in ground state with the cavity populated with a photon. [15] If the resonant exchange of energy between the cavity and the emitter is of greater probability (coupling strength, g) than the photon transmission through the cavity boundary (cavity photon decay, γ) and the exciton decay (κ), then the allowed frequencies of the cavity will be split due to the strong coupling between the cavity and the exciton. This phenomenon is called strong coupling between the excitons and photons. In the limit of strong light-matter interactions, one can no longer treat the excitons and photons separately. We must consider the new modes of the system that are in the form of a mixture of photons and excitons. This new eigenstate is called exciton-polariton or cavity-polariton. This new particle requires slow damping of both excitons and photons and a large exciton-photon coupling strength, *i.e*. a combination of a confined optical mode and large exciton oscillator strength. Exciton-polaritons have the properties of both photons and excitons. Using the mixture properties of exciton-polaritons for lasing and long-rang propagation is the main theme of the second part of this thesis.

1.5 Reference

[1] E. Silinsh and V. Capek, *Organic Molecular Crystals: Interaction, Localization, and Transport Phenomena* (1994).

[2] M. Pope and C. E. Swenberg, *Electronic Processes in Organic Crystals and Polymers* (1999).

[3] S. R. Forrest, Nature **428**, 911 (2004).

[4] C. Kittel, *Introduction to Solid State Physics* (Wiley New York, 1976).

[5] N. W. Ashcroft and N. D. Mermin, *Solid State Physics* (2005).

[6] R. G. Kepler, Phys. Rev. **119**, 1226 (1960).

[7] H. Yersin, *Highly Efficient OLEDs with Phosphorescent Materials* (Wiley Online Library, 2008).

[8] C. Adachi, M. A. Baldo, M. E. Thompson, and S. R. Forrest, J. Appl. Phys. **90**, 5048 (2001).

[9] M. A. Baldo, D. F. O'Brien, Y. You, A. Shoustikov, S. Sibley, M. E. Thompson, and S. R. Forrest, Nature **395**, 151 (1998).

[10] E. M. Purcell, H. C. Torrey, and R. V Pound, Phys. Rev. **69**, 37 (1946).

[11] H. Khosravi and R. Loudon, Proc. R. Soc. London. Ser. A Math. Phys. Sci. **433**, 337 (1991).

[12] H. Khosravi and R. Loudon, Proc. R. Soc. London. Ser. A Math. Phys. Sci. **436**, 373 (1992).

[13] R. R. Chance, A. Prock, and R. Silbey, Adv. Chem. Phys **37**, 1 (1978).

[14] W. L. Barnes, J. Mod. Opt. **45**, 661 (1998).

[15] J. M. Raimond, M. Brune, and S. Haroche, Rev. Mod. Phys. **73**, 565 (2001).

Part I Light Extraction in Organic Light-Emitting Devices

Chapter 2

Organic Light-Emitting Diodes and Device Optics

In this chapter, we review the basic principles of organic light-emitting diodes (OLEDs) and their optics.

2.1 Basics of organic light emitting devices

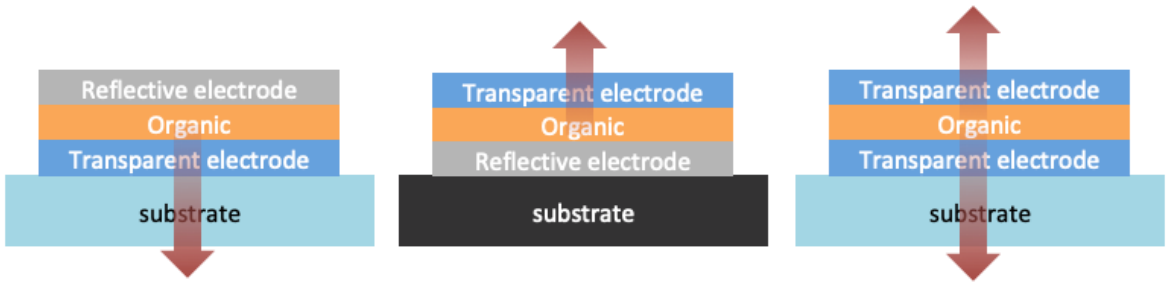

Figure 2.1 Organic light-emitting device types. Organic light-emitting devices can be categorized into (left) bottom-emitting, (middle) top-emitting and (right) transparent OLEDs, according to the emission direction relative to substrates. The red arrows indicate emission directions. Indium tin oxide (ITO) and thin metal films are typically used as transparent electrodes.

An OLED consists of organic layers sandwiched between two contacts. The electrical active region sits on a substrate. Under bias, electrical current is injected into the organic materials though contacts: holes from the anode and electrons from the cathode. These two carrier species can form excitons in the organic material and emit photons. Part of the generated photons travel into the air through the transparent electrode. Based on the transparency of the bottom and top electrodes, the devices can be categorized into top-emitting, bottom-emitting, and transparent OLEDs, as shown in Fig. 2.1. Indium tin oxide (ITO) and thin metal films are usually used as

bottom and top transparent electrodes, respectively. Bottom-emitting and transparent OLEDs require transparent substrates which are usually made of glass.

2.1.1 Metrics of OLED efficiency performance

Since the first modern multilayer OLED was introduced by Tang and VanSlyke [1], more sophisticated organic materials and device structures have been applied to improve performances. There are several commonly used metrics of OLED performance. The external quantum efficiency (η_{EQE}) is the ratio of photons emitted into air to charges injected into devices and can be expressed as follows:

$$\eta_{EQE} = \eta_{LE} \times \eta_{CB} \times \eta_{EF} \times \eta_{QY} = \eta_{LE} \times \eta_{IQE} \tag{2.1}$$

where η_{LE} is the light extraction efficiency or outcoupling efficiency, the ratio of the photons emitted into air to the photons generated, η_{CB} is the charge balance efficiency, the ratio of charges forming excitons to the charges injected into the device, η_{EF} is the exciton forming efficiency, the ratio of excitons eventually transferred to luminescent chromophores to the total excitons formed, and η_{QY} is the quantum yield, the ratio of photons generated to the excitons on chromophores. The latter three terms combine into the internal quantum efficiency (η_{IQE}). η_{IQE} can be close to unity when using a highly emissive phosphorescence emitter [2] and multiple functional organic layers [3] to confine charges and excitons to the chromophores. However, η_{LE} is usually only 20% due to the refractive index difference between the emissive layers and air. All efficiencies are unitless.

It is also important to quantify the OLED energy consumption efficiency. Another two standard metrics of OLED performance are the power conversion efficiency (η_{PCE}), which is the ratio of optical output power to the electrical input power, and luminance efficacy (η_{LE}), which is the ratio of luminous flux to the electrical input power with a unit of lm/W. η_{PCE} measures not

only the utility of quantum particles, but also the power of them. For example, for a device with η_{EQE} = 100%, η_{PCE} can be low if the device needs high bias voltages or emits low energy photons. Therefore, energy level alignment between different organic materials and high mobility are necessary to minimize energy loss and to keep the device drive voltage low.

2.1.2 OLED structure and operation

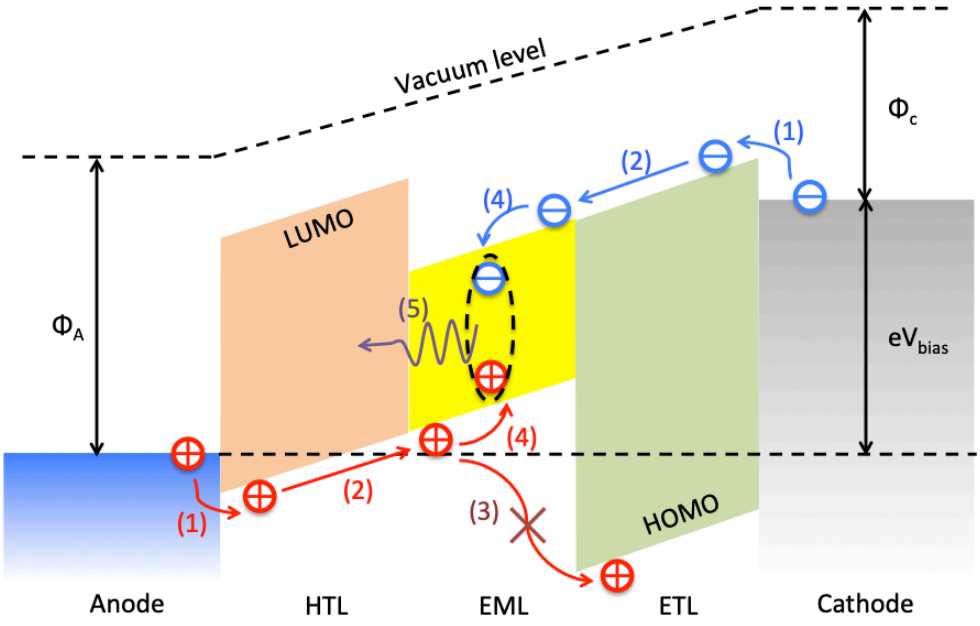

Figure 2.2 Operation of an OLED with three layers: (1) electrons are injected from the cathode into ETL. The work functions ($\Phi_{C/A}$) of the electrodes need to be aligned with HOMO/LUMO of the organic layers. (2) ETL conducts electrons into EML. (3) The HOMO level gap between ETL and EML prevents holes leaking into ETL. Therefore, both charges are confined and (4) form excitons in EML. (5) Excitons recombine and emit photons.

High performance OLEDs typically consist of the following layers: electron injection layer, electron transport layer (ETL), emissive layer (EML), hole transport layer (HTL) and hole injection layer, as shown in Fig. 2.2. Some devices also have hole/electron blocking layers between the ETL/HTL, respectively, and the EML to confine charges forming the excitons. The charge injection layers help the charge injected into transport layers from electrodes, as shown as step 1 in Fig. 2.2. Some commonly used charge injection layers include MoO_x and LiF, which are hole and electron injection layers, respectively. Charge transport materials are designed with

high mobility to minimize the energy loss during charge transport to the EML. The electron transport materials usually have similar LUMO levels with EMLs, while the hole transport materials have similar HOMO levels, as shown in Fig. 2.2. Large energy differences between the EML and charge transport layers results in either energy loss or barriers, depending on whose energy is lower. To prevent the charges leaking out of EML without forming excitons, the ETL/HTL usually has deeper HOMO/shallower LUMO than the EML. The EML usually consists of two or more materials to form a host-guest system. The host material provides sufficient charge transport and separate high quantum yield chromophore guest material. The spatial separation of the guest material prevents bi-exciton quenching. The guest chromophores usually have lower exciton energy than the host and other organic layers to prevent exciton transfer.

2.1.3 OLED efficiency characterization

To evaluate the efficiency of OLEDs, accurate and reliable measurement methods are necessary. Standardized measurement and calculation [4] of OLED efficiency have been established. The data needed to calculate OLED efficiency metrics includes: current injected into the device (I_{in}), device bias voltage (V_b), photon flux (J_{ph}) and spectrum ($\phi(\lambda)$). We can calculate average energy ($\overline{E_{ph}}$) or average luminance ($\overline{L_{ph}}$) per photon using the photopic response and measured emission spectrum from OLEDs. The metrics can be calculated as:

$$\eta_{EQE} = \frac{eJ_{ph}}{I_{in}} \tag{2.2}$$

$$\eta_{PCE} = \frac{\overline{E_{ph}} \times J_{ph}}{V_b \times I_{in}} \tag{2.3}$$

$$\eta_{LE} = \frac{\overline{L_{ph}} \times J_{ph}}{V_b \times I_{in}} \tag{2.4}$$

The J_{ph} can be measured using a photodiode to convert photon flux into measurable photocurrent (I_{ph}). Therefore, photodiode responsivity and spectrum $\phi(\lambda)$ are needed to calculate J_{ph}.

To capture all the light coming out of an OLED, a large area photodiode is usually placed immediately beneath the device. A small air gap between the photodiode and the OLED substrate can prevent extra light-extraction from the substrate modes. Meanwhile, the OLED substrate edges are covered to prevent the photodiode from capturing substrate mode leakage, as shown in Fig. 2.3. To measure the optical power trapped inside the substrate, an index-matching fluid (IMF) with the same index as the OLED substrate is applied between it and the photodiode, allowing all light entering the substrate to be captured by the photodiode, as shown in Fig. 2.3.

Figure 2.3 Photon flux measurements using a large aperture photodiode. Right, to prevent the photodiode capturing substrate modes leaked from substrate edges, the edges are covered. There is a small air gap between the substrate and photodiode to prevent extra light extraction from the substrate modes. Left, to measure substrate modes, index-matching fluid (IMF) is applied between the substrate and the photodiode.

2.2 Dipole emission near interfaces

In most OLEDs, exciton-photon interaction is in the weak-coupling regime. The radiative decay rate and optical power distribution from the excitons can be vastly different from those in free space. More generally, exciton emission in an OLED is a result of spontaneous emission of an emitter near interfaces. Both quantum [5,6] and classical [7–11] models are able to solve this problem. In this section, we review the classical picture of exciton emission in a cavity.

2.2.1 Classical CPS model

Chance, Prock and Silbey (CPS) [11] modeled a point dipole near interfaces, with electric field described by the dyadic Green's function. This technique calculates the dipole lifetime and the wavevector distribution. Since then, many others developed equivalent approaches based on the same concept. The details of such theories can be found in the literature and compared in depth by Sipe. [7]

The key is to derive an expression for the electric field reflected back to the dipole position by the environment. This can be done using the following conceptual steps: [8]

(1) Expand the dipole field as a summation of a complete set, such as plane waves and Bessel functions, characterized by different wavevectors in the plane of the interface.

(2) Evaluate the reflection coefficient for each of these wavevector components, taking account of the distance between the emitter and the surface, and the refractive index of the intervening materials. If there is more than one interface, an equivalent interface is necessary.

(3) Sum these reflected fields to calculate the total reflected field.

(4) Combine the reflected field with the source field of the dipole to deduce the spontaneous emission rate.

(5) Do the above for all dipole orientations.

In the CPS model, the equation of motion of the dipole is expressed as:

$$\ddot{\boldsymbol{p}} + \omega_0 \boldsymbol{p} = \frac{e^2}{m} \boldsymbol{E}_r - b_0 \dot{\boldsymbol{p}} \tag{2.5}$$

where ω_0 is the resonant angular frequency in the absence of damping, m is the effective mass, e is the electric charge, E_r is the reflected field at the dipole position r, and b_0 is the damping

constant in free space. The reflected field, E_r, works on the dipole and oscillate at the same frequency $\Omega = \omega - ib/2$:

$$p = p_0 \exp(-i\Omega t) = p_0 \exp\left(-i\omega t - \frac{b}{2}t\right) \tag{2.6}$$

$$E_r = E_{r0} \exp(-i\Omega t) \tag{2.7}$$

where ω and b are the frequency and damping rate in the presence of the reflected field E_r. The dependence of ω and b on E_r can be derived from Eq. 2.5:

$$b/b_0 = 1 + \frac{e^2}{m\omega b_0 p_0} Im(E_{r0}) \tag{2.8}$$

$$\Delta\omega = \omega - \omega_0 = \frac{b^2}{8\omega} + \frac{e^2}{2m\omega_0 p_0} Re(E_{r0}) \tag{2.9}$$

The frequency shift $\Delta\omega$ is quite small compared to the dipole resonant frequency ω_0 especially in the weak-coupling regime. Therefore, the frequency shift is usually not taken into consideration. We now introduce the quantum yield of the emitter: $q = b_r / b_0$, where b_r is the radiative decay constant. This definition is consistent with Eq. 1.8. In the classical picture, b_r can be expressed as following:

$$b_r = \frac{2n\omega e^2}{3mc^3} \tag{2.10}$$

We can rewrite Eq. 2.8 as:

$$b/b_0 = 1 + \frac{3qc^2}{2n\omega^3 p_0} \mathrm{Im}(E_{r0}) \tag{2.11}$$

2.2.2 Dyadic Green's function method

We see from Eqs. 2.8, 2.9 and 2.11 that the damping rate b and frequency shift $\Delta\omega$ are related to the out-of-phase and the in-phase components of the reflective field. So the problem is

now reduced to calculating the reflected field at the dipole position. To solve, we need to expand the emission field as a summation of a complete set. Plane wave functions (transfer matrix) are usually applied. However, different eigenfunctions can make the problem easier for the specific interfaces surrounding the emitter and the coordinate we choose. In the rest of this section, we use dyadic Green's function method to solve this problem.

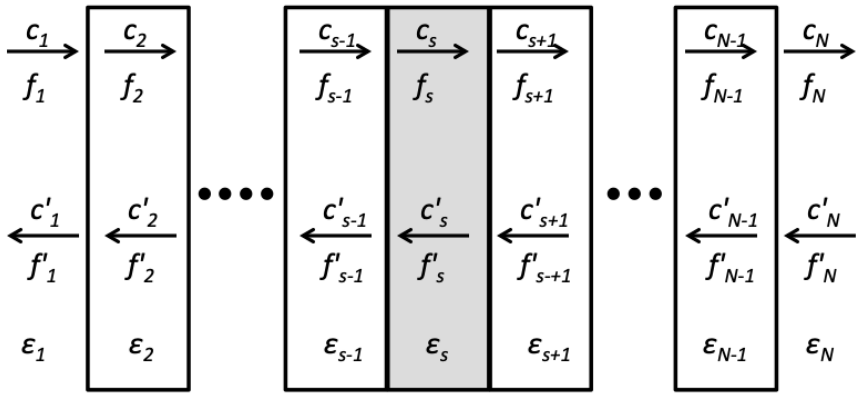

Figure 2.4 Coefficients and index of the general multilayer structure for the OLED optical simulation.

We begin the calculation with the expression for the electric field emitted from an oscillating current, using the electric field dyadic Green's function.

$$\boldsymbol{E}(\boldsymbol{R}) = i\omega\mu \int \boldsymbol{G}(\boldsymbol{R}|\boldsymbol{R}') \cdot \boldsymbol{J}(\boldsymbol{R}')\, d\boldsymbol{R}' \tag{2.12}$$

where $\boldsymbol{G}(\boldsymbol{R}|\boldsymbol{R}')$ is the dyadic Green's function for electric field, and $\boldsymbol{J}(\boldsymbol{R}')$ the oscillating current. For a two-dimensional symmetric multilayer stack, the Green's function can be expressed as the summation of two independent sets of eigenfunctions in cylindrical coordinates:

$$\boldsymbol{M}_{\boldsymbol{nk}_{\boldsymbol{o}}}^{\boldsymbol{e}}(h) = e^{ihz}\left[\mp\frac{nJ_n(kr)}{r}\begin{matrix}sin\\cos\end{matrix}n\phi\hat{r} - \frac{\partial J_n(kr)}{\partial r}\begin{matrix}cos\\sin\end{matrix}n\phi\hat{\phi}\right] \tag{2.13}$$

$$\boldsymbol{N}_{\boldsymbol{nk}_{\boldsymbol{o}}}^{\boldsymbol{e}}(h) = \frac{e^{ihz}}{\sqrt{k^2+h^2}}\left[ih\frac{\partial J_n(kr)}{\partial r}\begin{matrix}cos\\sin\end{matrix}n\phi\hat{r} \mp inh\frac{J_n(kr)}{r}\begin{matrix}sin\\cos\end{matrix}n\phi\hat{\phi} + k^2 J_n(kr)\begin{matrix}cos\\sin\end{matrix}n\phi\hat{z}\right] \tag{2.14}$$

where k and h are the amplitudes of the parallel and perpendicular components of the wavevector. J_n is the Bessel function of the first type of order n. The non-scattering and scattering Green's function can be written as [11]

$$\boldsymbol{G_0}(\boldsymbol{R}|\boldsymbol{R'}) = \frac{i}{4\pi}\int_{\mathbf{0}}^{\infty} dk \sum_{\substack{n=0 \\ t=e,o}}^{\infty} \frac{2-\delta_{n0}}{kh} \begin{bmatrix} \boldsymbol{M}_{nkt}(h)\boldsymbol{M'}_{nkt}(-h) + \boldsymbol{N}_{nkt}(h)\boldsymbol{N'}_{nkt}(-h) \\ \boldsymbol{M}_{nkt}(-h)\boldsymbol{M'}_{nkt}(h) + \boldsymbol{N}_{nkt}(-h)\boldsymbol{N'}_{nkt}(h) \end{bmatrix} \begin{matrix} z > 0 \\ z \leq 0 \end{matrix} \quad (2.15)$$

$$\boldsymbol{G_{sj}}(\boldsymbol{R}|\boldsymbol{R'}) = \frac{i}{4\pi}\int_{\mathbf{0}}^{\infty} dk \sum_{\substack{n=0 \\ t=e,o}}^{\infty} \frac{2-\delta_{n0}}{kh} [\, c_j \boldsymbol{M}_{nkt}(-h_j)\boldsymbol{M'}_{nkt}(h_s) + f_j \boldsymbol{N}_{nkt}(-h_j)\boldsymbol{N'}_{nkt}(h_s)$$

$$+ c'_j \boldsymbol{M}_{nkt}(h_j)\boldsymbol{M'}_{nkt}(h_s) + f'_j \boldsymbol{N}_{nkt}(h_j)\boldsymbol{N'}_{nkt}(h_s) \,] \quad (2.16)$$

where j indicates the j^{th} layer and s denotes the layer in which the emitter sits. We define the dipole position as $z = 0$. The coefficients c, f, c' and f' are Fresnel coefficients correspond to the different direction of propagation and can be determined using the boundary condition at layer interfaces, as shown in Fig. 2.4. Note that the total Green's function should be the addition of non-scattering and scattering parts. We can use Eq. 2.12 to calculate the electric field distribution. $\boldsymbol{G}(\boldsymbol{R}|\boldsymbol{R'})$ is a dyadic function, which has the form of a 3-by-3 matrix to be multiplied by the 3-by-1 current vector $\boldsymbol{J}(\boldsymbol{R'})$. The three components of the current vector denote three directions the dipole orients: two axes parallel to the layer plane (one transverse electric dipole, TE and one transverse magnetic dipole, TM) and one axis in the perpendicular (TM) direction. Since the dipole orientation is random in amorphous organic materials in OLEDs, the amplitude ratio of these three components is 1:1:1. So the isotropic decay rate is

$b_{iso}=b^{\perp TM}/3+b^{\parallel TM}/3+b^{\parallel TE}/3$. Expanding the field in terms of the Green's function, Eq. 2.11 can be rewritten as:

$$b^{\perp TM}/b_0 = 1 - q + q\{1 + \frac{3}{2}Re[\int_0^\infty dk \frac{{k_s}^3}{h_s({h_s}^2 + {k_s}^2)^{\frac{3}{2}}}({f_s} + {f'}_s)]\} \tag{2.17}$$

$$b^{\parallel TM}/b_0 = 1 - q + q\{1 + \frac{3}{2}Re[\int_0^\infty dk \frac{{k_s}^2}{h_s({h_s}^2 + {k_s}^2)^{\frac{3}{2}}}({f_s} - {f'}_s)]\} \tag{2.18}$$

$$b^{\parallel TE}/b_0 = 1 - q + q\{1 + \frac{3}{2}Re[\int_0^\infty dk \frac{k_s}{h_s({h_s}^2 + {k_s}^2)^{\frac{1}{2}}}({c_s} + {c'}_s)]\} \tag{2.19}$$

where *f* and *c* are Fresnel coefficients for each mode and each propagation direction.

We also use this method to calculate the power distribution inside the device, which can be obtained using the Poynting vector across interfaces. For a two-dimensional symmetric multilayer stack, the Poynting vector in *z* direction can be expressed as:

$$Re(\int S_{z,j}^{\perp TM}\, dA)$$

$$= \frac{3q}{4}Re[\int_0^\infty du \frac{u^3(\sqrt{\varepsilon})^*}{|1-u^2|\sqrt{\varepsilon}}\left(\frac{\varepsilon_j}{\varepsilon_s} - u^2\right)^{\frac{1}{2}}\left({f'}_j e^{ih_j z} - f_j e^{-ih_j z}\right)\left({f'}_j e^{ih_j z} + f_j e^{-ih_j z}\right)^*] \tag{2.20}$$

$$Re(\int S_{z,j}^{\parallel TM}\, dA)$$

$$= \frac{3q}{4}Re[\int_0^\infty du \frac{u^3(\sqrt{\varepsilon})^*}{(\sqrt{\varepsilon})}\left(\frac{\varepsilon_j}{\varepsilon_s} - u^2\right)^{\frac{1}{2}}\left({f'}_j e^{ih_j z} - f_j e^{-ih_j z}\right)\left({f'}_j e^{ih_j z} + f_j e^{-ih_j z}\right)^*] \tag{2.21}$$

$$Re\left(\int S_{z,j}^{\parallel TE}\, dA\right)$$

$$= \frac{3q}{4} Re\left[\int_0^{\infty} du \frac{u}{|1-u^2|}\left(\frac{\varepsilon_j}{\varepsilon_s} - u^2\right)^{\frac{1}{2}*} \left(c'_j e^{ih_j z} + c_j e^{-ih_j z}\right)\left(c'_j e^{ih_j z} + c_j e^{-ih_j z}\right)^*\right]$$

(2.22)

where $u = k/(k^2+h^2)^{1/2}$, or the normalized parallel component of the wavevector, which denotes the power transfer directions. These integrals denote the net power transfer across a layer interface and the Poynting vectors are functions of u. We can set up two artificial interfaces sandwiching the emitter, and expand the energy transfer in terms of direction to study the optical power distribution inside OLEDs. This is the main topic of the next section.

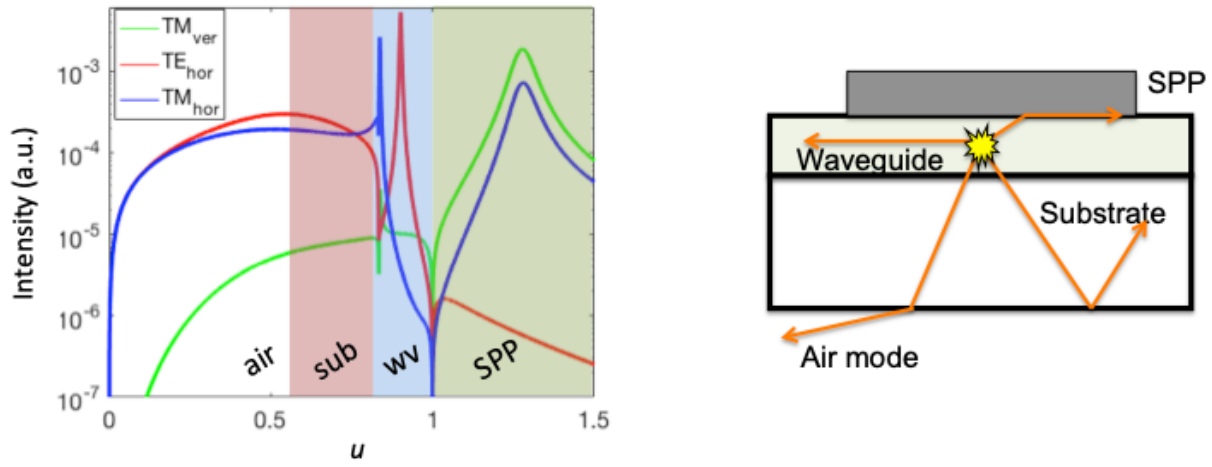

Figure 2.5 Power distribution of an OLED. Left, $u=k_{||}/k_s$ denotes the direction of optical power. k_s indicates the wavevector amplitude in the source layer. When $u>1$, the optical wave is an evanescent wave in emission layer. In OLEDs, the green area ($u>1$) is the surface plasmon mode; the blue area ($n_{sub}/n_{org}<u<1$) is the waveguide modes; the red area ($n_{air}/n_{org}< u< n_{sub}/n_{org}$) is the substrate modes; the white area is the air modes. Note that the surface plasmon mode is a TM mode, and the waveguide modes include both TM and TE modes. The vertical dipole couples more into the waveguide and surface plasmon modes, contributing less to the light-extraction efficiency. Right, the schematic illustration for each mode.

2.3 Exciton emission in OLEDs

In this section, we describe exciton emission in OLEDs using the dyadic Green's function. We first discuss the optical distribution and optical loss in OLEDs, and light extraction efficiency dependence on device structure. Then we discuss the exciton emission rate and the dependence of exciton lifetime on device structure.

2.3.1 Optical power distribution in OLEDs

OLEDs are thin-film devices with flat interfaces. Since photons are generated in the organic materials with higher refractive index compared to air, only a fraction of optical power emitted from excitons can eventually come into air. Thus, a calculation method is necessary for us to study and understand OLED optics.

The power transfer across two artificial interfaces sandwiching the emitter as a function of propagation direction shows the optical power distribution inside OLEDs. As an example, Fig. 2.5 shows the optical power distribution (λ = 500 nm) inside a conventional bottom-emitting OLED. For simplicity, in this simulation we use a 100 nm silver cathode, a 120 nm organic layer with an index n_{org} = 1.7, a 100 nm ITO with an index n_{ITO} = 1.7 and a semi-infinite glass substrate with an index n_{sub}=1.5. $u = k_{||} / k_s$ is the parallel component of the wavevector normalized to the wavevector in the emission layer. The plot shows the optical power in different directions. For example, when u = 0, the optical power transfers perpendicularly to the device interfaces. The power distributions generated from three different dipole orientations are demonstrated separately. The three data sets share four different optical modes that are marked with different colors in Fig. 2.5:

(1) when $u < n_{air} / n_{org}$, the optical power can escape from all high-index materials and eventually comes into the air. We call this part of the optical power air modes.

(2) when $n_{air} / n_{org} < u < n_{sub} / n_{org}$, the optical power is trapped inside the substrate due to total internal reflection at the glass/air interface and reflection from the metal electrode, which we call substrate modes. The major loss of the substrate modes results from the reflection at the metal interface. For example, the aluminum reflectivity is less than 90% in the visible regime.

(3) when $n_{sub} / n_{org} < u < 1$, the optical power is trapped in the organic (n_{org} = 1.6-2) and ITO (n_{ITO} = 1.8-2.1) region, due to the total internal reflection at the organic/glass interface and reflection from the metal electrode, which is called waveguide modes. Since the thicknesses of ITO and organic layers are on the sub-wavelength scale, standing waves in the perpendicular direction between two reflectors are required to form these modes. Therefore, unlike the air and substrate modes, the propagation constants of waveguide modes are discrete. The major loss of these modes is absorption by the metal contact. Since the spatial penetration into the metal electrode is different for each waveguide mode as shown in Fig. 2.6, the propagation attenuation coefficients are different. Generally, the waveguide modes can travel tens of microns before dissipation.

(4) when $u > 1$, the TM light is trapped at the metal interface, which is called the surface plasmon mode or surface plasmon polaritons (SPPs). Since the SPP mode is tightly confined at the metal interface, the optical loss is big with an attenuation coefficient up to 1 μm^{-1}.

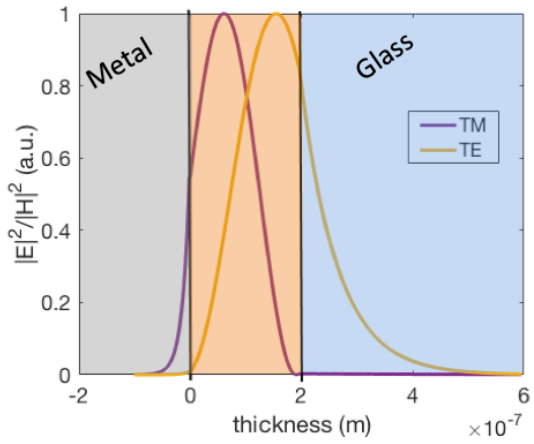

Figure 2.6 TE_0 and TM_0 modal profiles in an OLED, with $n_{ITO} = n_{org} = 1.7$, $n_{sub} = 1.5$.

In a flat structure like a conventional OLED, all these modes cannot couple to each other due to photon momentum conservation along the interfaces. Therefore, the waveguide and SPP modes can only transfer into heat, while the substrate modes can leak out at the substrate edges.

The optical power distribution for different dipole orientations are different, as shown in Fig. 2.5. The horizontal dipoles are more likely to couple into the air and substrate modes than the vertical dipole, while the vertical dipole couples most power into SPPs. So the horizontal dipoles are preferred for high light extraction efficiency. The TE and TM horizontal dipoles couple into different waveguide modes, and TM couples to SPPs while TE does not. However, since the TE and TM are only defined in the OLED plane we study, in reality a horizontal dipole couples to both TE and TM modes at the same time, just in different directions.

Figure 2.7 shows the total optical power distribution across the visible regime. This simulation uses the same OLED structure as mentioned above. The optical power distribution varies with different emission wavelengths. As the wavelength increases, the TM waveguide mode (left) gradually fades while the TE waveguide mode (right) power increases; the intensity

peak of the air and substrate modes gradually moves toward the substrate normal direction (low u) and moves back to the substrate horizontal at a turning point wavelength of $\lambda \sim 550$nm. Thus, there is more optical power emitted into air modes at that wavelength; the SPP mode is quite strong across the whole visible regime.

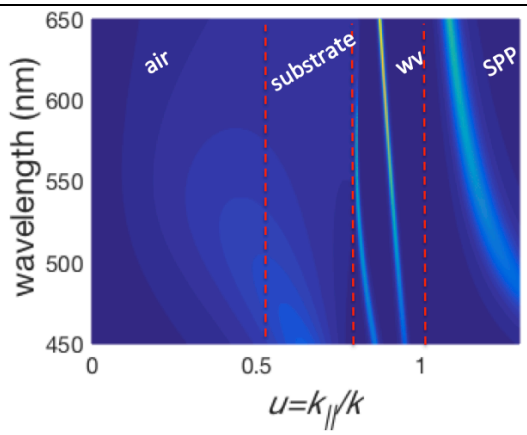

Figure 2.7 Power distribution of an OLED *vs.* different emission wavelength.

For a monochromic OLED, the optical power distribution depends on device structures, as shown in Fig. 2.8. The power fraction of each mode is calculated from the total energy transfer across the layer interfaces over u of each mode. The 'Abs.' in Fig. 2.8 denotes the metal absorption since other materials in the simulation are lossless. The loss is calculated as the energy transfer into the metal across the organic/metal interface. The simulation calculates time average power flux, and all waveguided optical power eventually dissipates into the metal electrode. Therefore, metal absorption would be exaggerated if power flux across the metal surface with all u was included. Therefore, we only treat the energy transfer with $u < n_{sub} / n_{org}$ as absorption, and categorize the power with $u > n_{sub} / n_{org}$ into waveguide and SPP modes.

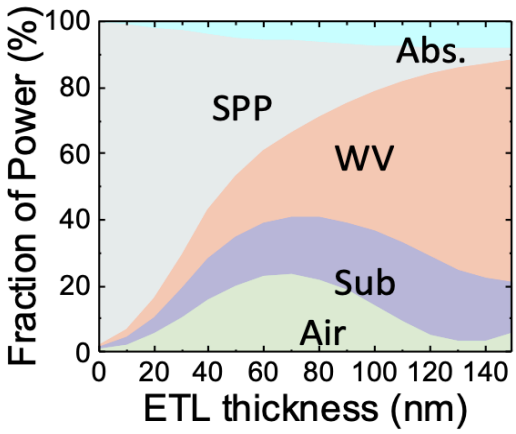

Figure 2.8 Power distributions *vs.* different ETL thickness, with an emission wavelength λ = 540nm. The thickness of ITO, HTL and EML are 100nm, 40nm and 10nm, respectively. For simplicity we use 1.7 as the refractive indices of ITO and organic layers.

The ETL thickness is the distance between the excitons and the organic/metal interface. As the ETL thickness increases, the air and substrate modes go up and down together, with a peak around 20% and 40%, respectively, at an ETL thickness of 65nm. This ETL thickness enables the highest light extraction efficiency because excitons are at a field anti-node. Thus, other emission wavelengths require different ETL thicknesses for the optimal light extraction efficiency. The waveguide modes and SPPs monotonically increase and decrease as the ETL gets thicker, respectively. Excitons couple into SPPs through a near-field evanescent wave. Thus, the separation between the emitter and the metal surface can strongly suppress the coupling rate. When the ETL is smaller than 40 nm, the SPP coupling is the dominant optical loss channel. At the local efficiency maximum with an ETL thickness of 65nm, the SPP loss is ~40%, while the waveguide mode loss is ~20%. As the ETL gets thicker, the waveguide modes gradually become the dominant loss channel.

2.3.2 Exciton emission rate in OLEDs

In Section 2.2 we discussed a classical method to calculate the radiative rate modulation by the cavity. Here we use the CPS model to study the exciton lifetime in conventional OLED structures. We focus on the optical modulation of the emitter radiative rate. The lifetime change due to bi-excitonic interactions is beyond the scope of this section. As shown in Fig. 2.8, optical power distribution from excitons varies with ETL thickness. Here we use the same OLED structures as Fig. 2.9 with varying ETL thickness to study exciton emission rate. The emission wavelength is λ = 540nm.

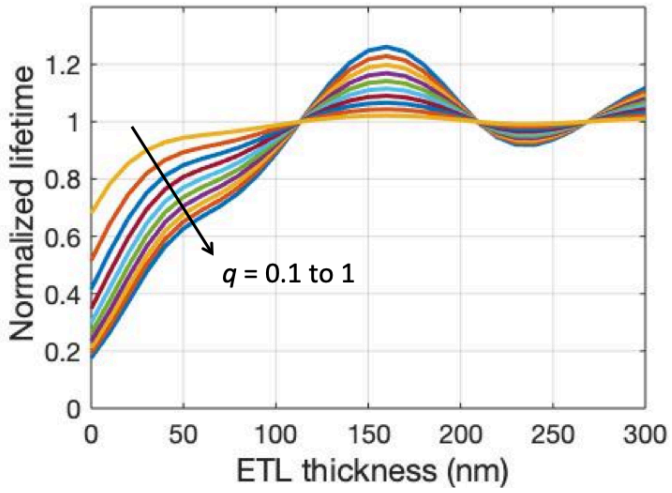

Figure 2.9 Calculated lifetimes of excitons with different quantum yield (QY) in OLED stacks with different ETL thickness. The q ranges 0.1 to 1 with a step of 0.1. The lifetime is normalized to the lifetime of an exciton in the free space.

As shown in Eq. 2.11, the exciton lifetime depends on the out-of-phase component of reflected electric field, Im(E_{r0}), at the exciton position and the quantum yield q of the emitter. As the ETL thickness changes, the exciton lifetime varies due to different Im(E_{r0}), while q demonstrates the sensitivity of an exciton to the reflected field, as shown in Fig. 2.9. As q decreases, the lifetime modulation by the environment is less. When q = 0, the lifetime is independent on the surroundings since the exciton can only decay through non-radiative

channels. When ETL is smaller than 50nm, the exciton lifetime is shortened due to SPP coupling. When the ETL is larger than 100nm, the lifetime goes up and down around relative lifetime of 1. This oscillation results from the varying coupling strength with the air and substrate modes. To quantitatively demonstrate the contribution from each mode to the lifetime modulation, we calculate the second term in Eq. 2.8 over *u*, as shown in Fig. 2.10. The lifetime modulation from air and substrate modes oscillates around zero. We can see from Fig. 2.8 and 2.10 that the ETL thickness, which the shortens the lifetime most, results in highest quantum efficiency. The lifetime modulation from waveguide modes is always negative, which contributes to longer exciton lifetime. On the contrary, SPPs always shorten the exciton lifetime. Since excitons couple to SPPs through near-field evanescent waves, the effects from SPP mode disappear when the ETL thickness is larger than 150nm.

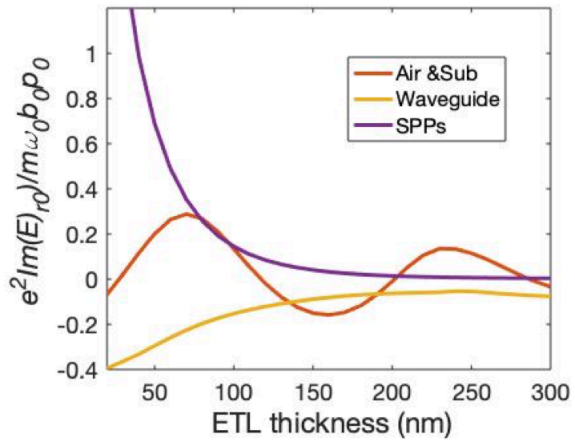

Figure 2.10 Contribution from each mode to the exciton lifetime modulation. The y-axis is the second term in Eq. 2.8.

2.4 Previous work on OLED light extraction

Electrophosphorescent organic light emitting devices (PHOLEDs) can yield 100% internal quantum efficiency (η_{IQE}). [2,12] This leads to an external quantum efficiency (η_{EQE}) of ~20%for OLEDs on glass [13] without outcoupling enhancements. As mentioned above, the remaining emitted photons are trapped in the substrate due to total internal reflection at the glass-air interface, [14] are guided within the organic material layers and the transparent anode due to their high refractive indices compared to glass, [15] and are dissipated at the organic/cathode interface by exciting the SPP mode. [16,17]

2.4.1 Substrate mode outcoupling

The substrate modes account for ~20% optical power trapped for bottom-emitting devices. The substrate modes result from the total internal reflection. The escaping cone is determined by Snell's law $\sin \theta_{critical}=1/n_{sub}$ where n_{sub} and $\theta_{critical}$ are the substrate index and critical angle less than that which the light can escape through the interface, respectively. In the case of glass substrates, $\theta_{critical} = 42°$.

The light extraction methods for this fraction of optical power mainly seek to expand the escape cone, redirect the trapped light and provide subsequent reflection from the metal cathode additional opportunities to transmit into air. The methods can be roughly classified into two types: the geometric corrugation of the substrate interface or optical scattering centers using refractive index contrast. Typically, corrugation is in the multi-micron scale without obvious Mie or Rayleigh scattering. This structure can be seen as planar interfaces with different tilting angles next to each other, which reflect or bend but not scatter the light. Therefore, ray approximation can still be applied. The corrugation enlarges the escape cone and reflects light back into the substrate in different directions, which has another chance to enter the escape cone after

reflection from the metal electrode. A typical example using substrate interface corrugation is microlens arrays, [18,19] as shown in Fig. 2.11.

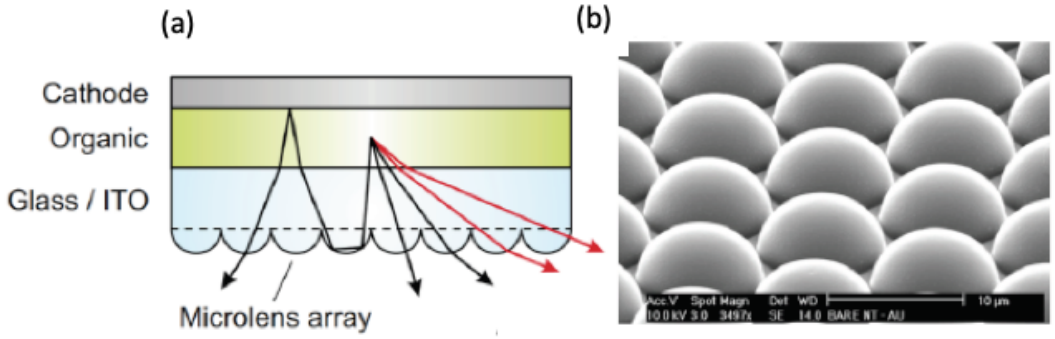

Figure 2.11 External microlens arrays for substrate mode extraction. (a) Principles of operation of the microlens array. (Brütting *et al*., 2013) The black and red arrows indicate the light travelling inside and outside the original escaping cone, respectively. (b) Image of a hexagonal array of hemispherical microlens with a diameter of 10 microns. (Sun *et al.*, 2008)

The microlens has the same index as the glass substrate. The light traveling outside the original escaping cone is incident on the microlens curved surfaces and hence can escape. However, the transmission at angles within the escape cone is usually reduced compared to a planar substrate-air interface. This fraction of optical power is redirected back into the device and reflected by the metal contact before escaping from the device, shown as the black ray in Fig 2.11. The shape of the microlens is important because it determines the enlarged escape zone and the reflection direction. Therefore, random roughening usually cannot compete with the performance of microlens arrays.

The scattering centers usually have nano-scale or micron-scale structures with a feature size comparable with the emission wavelength. The optical waves incident on these centers, are scattered into all directions. The scattering pattern depends on the ratio of the wavelength to the feature size of the scatterer according to Mie theory. Therefore, the size and density of scattering particles play important roles to optimize the light extraction performance. The scattering layer

can either be put between the substrate and transparent anode or at the substrate-air interface. The former outcouples not only the substrate modes but also the waveguide and SPP modes, which will be discussed in the next subsection. Therefore, the light extraction enhancement is significantly improved compared with substrate back surface treatment.

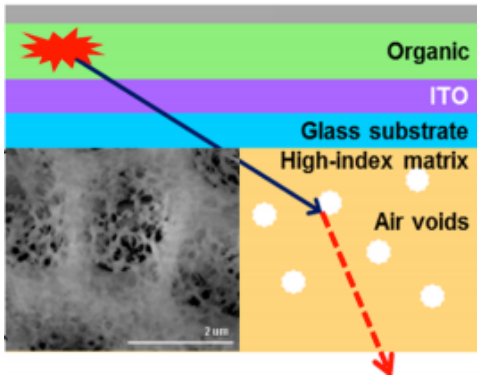

Figure 2.12 Principles of operation of a scattering film by Koh *et al*. The micrograph on the left-bottom shows the sub-micron scale voids in the high index polyimide film.

The scattering centers are usually immersed in a matrix. A large index contrast between the matrix and the scattering centers is desired. The index of the scattering centers can be higher or lower than that of the matrix. [20–22] Koh *et al*. [21] demonstrated a high index polyimide layer with an index $n > 1.7$, inside which has low index voids are immersed. This film can be attached at the back of the substrate and enhances light-extraction efficiency by nearly 80%, corresponding to 70%-80% of the substrate modes.

The substrate modes can be entirely extracted using a large hemispherical lens attached to the emitting surface of the substrate. However, this method is usually not practical due to the large size of the lens. To extract all the substrate modes, propagation from any spot on the OLED emitting surface to lens surface should be within 42° to the lens surface normal. Therefore, as the lens size is reduced, and the efficiency drops as more light fails to meet this requirement.

2.4.2 Waveguide modes outcoupling

The waveguide modes and SPPs together account for up to 50% of the generated optical power. The fraction of waveguide modes depends on the structure of OLEDs. For the EML sitting at the first anti-node, the waveguide modes account for 20-30% of the generated power. Thicker organic layers, as in the multilayer white OLEDs, can support high order TE and TM modes, resulting in more trapping power in these modes. Since the waveguide modes are trapped in the ITO and organic layers, the outcoupling of these modes requires structures in close proximity to, or even within the OLED active layers. Many solutions may lead to reduced manufacturing yield or unwanted change in electrical characteristics of devices.

The most straightforward method to outcouple the waveguide modes is to use a high index substrate, which is comparable to that of the active region. [23–25] If the index of the substrate is higher than the active region, there is no waveguide mode. Followed by a substrate light extraction structure, the high index substrate may result in effective performance. For example, using a large hemisphere lens with the same index, all optical power but SPPs can be extracted into air. Therefore, the enhancement factor of this method varies with the fraction of SPPs that mainly depend on the distance between excitons to the metal surface. However, the high index substrate is significantly more costly than glass and raises concerns about toxicity and environmental impact, [26] making this strategy incompatible with practical applications.

Another simple strategy to reduce the waveguided optical power is to use a strong cavity. [27,28] This method does not redirect the waveguided optical power into air, but forces excitons to emit into the substrate normal direction. However, since the cavity has only one resonant frequency, this method is limited to monochromatic devices. The structures using this strategy are usually simple to fabricate and scale up, with intuitive optical designs. It would be

quite useful in the applications using single color devices, such as pixels in displays. Wang *et al*. demonstrated a simple cavity using two metallic electrodes with a high index layer between the substrate and the anode, which optimizes the cavity for the emission wavelength. This design can boost the external quantum efficiency to 60% with an external lens for a green OLED.

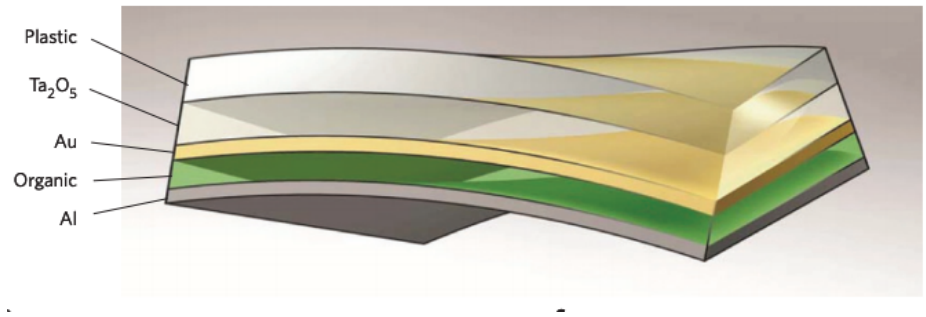

Figure 2.13 Schematic presentation of the work by Wang *et al*. The efficiency can be up to 60% with a quite simple optical design.

Optical gratings or photonic crystals placed within or near the OLED active region can also modulate the photonic mode density to extract light. [29,30] A grating usually has a periodic or multi-periodic structure with a sub-wavelength feature size. When placed near the emitting excitons, the gratings couple the waveguide and SPP modes into air and substrate modes. Therefore, the SPPs can also be suppressed. This method also modifies the exciton emission pattern, which has a strong dependence on emitting wavelengths. Although this structure can scatter guided modes effectively, the strong dispersion needs an optical diffuser to remove the wavelength and viewing angle dependence.

Bocksrocker *et al.* [29] placed a TiO_2 optical grating directly onto the ITO using laser interference lithography. A PEDOT: PSS conductive polymer is spin-coated for planarization and then a white OLED (WOLED) is completed by depositing the organic layers and the cathode, schematically presented in Fig. 2.14. This optical grating within the electrical active

region of the WOLED extracts waveguide modes and SPPs simultaneously, introducing a strong wavelength dependent emission pattern inside the substrate. The microlens array at the glass-air interface extracts the substrate modes and, as an optical diffuser, reduces the strong dispersion introduced by the grating. The emission coming out of the substrates shows a uniform white emission without grating features with an enhancement factor of four in light extraction compared to a conventional WOLED on a flat glass substrate.

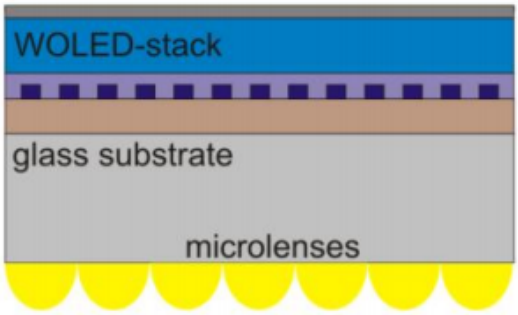

Figure 2.14 Schematic presentation of the work by Bocksrocker *et al*. The optical grating right next to the OLED active region extracts waveguide and SPP modes into the substrate. External microlens array extracts the substrate modes and at the same time reduces the angle dependence of the white emission as an optical diffuser.

Multi-periodic [31] or semi-randomized grating structures [32] also show good performance for guided optical power extraction. Koo *et al*. demonstrate a spontaneous formed buckling surface, on which the OLED achieves doubled efficiency at green wavelengths and quadrupled at red wavelengths. The spontaneous formed buckling is produced using a 10 nm Al on a PDMS layer and heated together to 100° C. The buckles are formed after cooling due to the different thermal expansion of the two materials. The number of the Al and PDMS pairs can control the depth of the corrugation. This rippled surface functions as a mold, which is pressed onto a resin film spun on the glass substrate and transfers the buckled pattern. After resin curing, the mold is peeled-off, followed by deposition of OLED active layers, as shown in Fig. 2.15. The

pattern of the buckled surface is 2-dimensional and isotropic with a characteristic buckling period of Λ = 400 nm. The Fourier transform of the pattern shows a clear spatial period with a broad full width at half maximum.

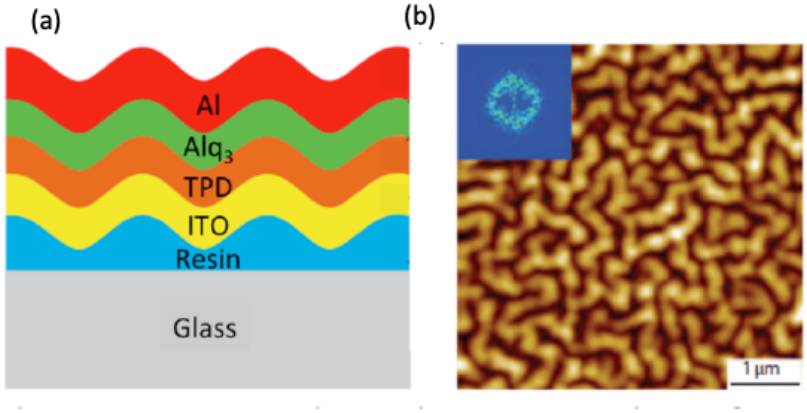

Figure 2.15 (a) Schematic presentation of an OLED on a buckled UV-curable resin surface. (b) An atomic force micrograph of a buckled surface. The inset shows a Fourier transform of the patterns, demonstrating a broad yet clear spatial period of the rippled surface.

Another strategy is to use micron-scale structures within or near the active region to scatter the trapped waveguided optical power. Different from the optical gratings, these structures do not modulate the exciton spontaneous emission profile but only scatter the waveguide modes into different directions. The SPP mode is usually tightly confined at the metal interface. Unless the structure introduces a corrugated electrode or intrudes into the active region, it is not effective for SPPs extraction. [32,33] One example using this strategy is the low index grid proposed by Sun *et al*. and further optimized by Slootsky *et al*. [33–35] This grid is fabricated directly onto the ITO with a period of Λ = 6 µm embedded in the OLED active region, as shown in Fig. 2.16, which introduces a corrugated surface. Since the grid is made of an insulator SiO_2, this structure does not change the OLED electrical characteristics. The grid has been shown to be effective in light extraction, resulting in an enhancement factor of 2.3 with the

external microlens array. However, this method reduces effective electrical active region area and material utility, since the devices on top of the gridlines are no longer functioning.

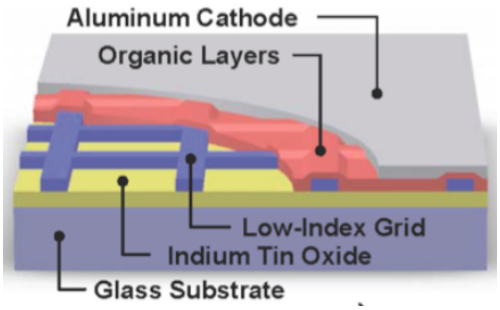

Figure 2.16 Schematic presentation of an OLED using a low index grid for light extraction. The low-index grid sits directly onto the ITO inside the active region with a period of Λ = 6 μm. The gridline width is 1 μm.

A flat layer with a scattering structure embedded between the transparent anode and the substrate is a quite popular strategy in recent years, which apparently does not have the shortcomings mentioned above. Nanoparticle scattering films placed between the transparent anode and substrate [36,37] is one of the first structures using this strategy, but to our knowledge there is no direct evidence of its effectiveness in extracting waveguided light. Recently, Jeon *et al*. demonstrated a random-patterned vacuum nano-hole array embedded inside a high-index material between the ITO and the substrate (Fig. 2.17), which boosts WOLED efficiency up to η_{EQE} = 78% and η_{LE} = 164 lm/W with the help of a large external hemispherical lens. [38] To ensure the flatness of the surface that supports the OLED active region, the vacuum nano structures are fabricated between the high index Si_3N_4 layer and the glass substrate. The Si_3N_4 layer confines the waveguided light due to its high index and moves the power away from the absorptive metal electrode while the nano-voids scatter the optical power into the substrate.

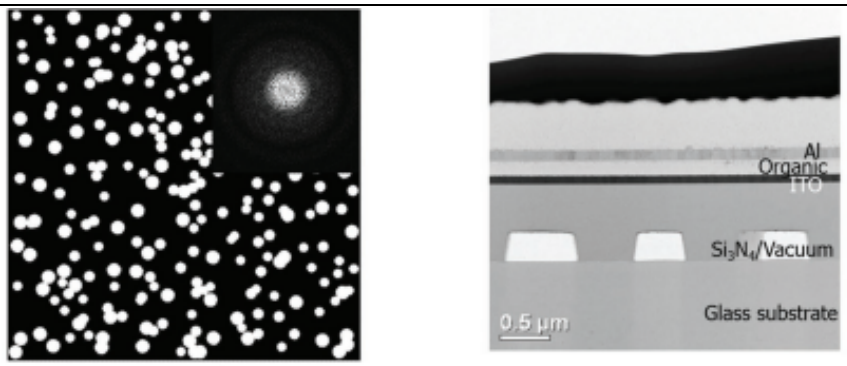

Figure 2.17 The top-view and cross-section of the light extraction structure proposed by Jeon *et al.* The white dots on the left figure are the vacuum nano-holes embedded in the high index Si_3N_4 layer. Inset: Fourier transfer of spatial patterning of the voids.

2.4.3 SPPs outcoupling

Since the SPPs are tightly confined at the metal interface, the light extraction structures have to be within the active region or introduce metal interface corrugation to extract this fraction of light. These structures usually also extract waveguide modes, discussed in the previous subsection, such as the optical grating, low-index grids and spontaneously formed buckling surfaces. SPPs also suffer from a large extinction coefficient up to 1 μm^{-1}, and hence the structure needs to have a small feature size to be effective. A way to suppress SPPs is to increase the distance between the excitons to the metal surface, reducing the SPP coupling in the first place. This strategy can be seen in many device designs, including ones discussed in the next chapters.

2.4.4 Molecular dipole alignment

As discussed in the previous sections, the horizontal dipoles are more likely to emit photons into the air and substrate modes, while the vertical dipoles tend to couple into the waveguide and SPPs. Manipulation of the molecular dipole orientation within the emission layer to favor emission into the out-of-plane directions has been a quite popular topic [39–41]. Many

works have been done from the perspective of molecular design and the growth techniques. [42–46] Even a perfect horizontally oriented emission layer can still benefit from light extraction structures, achieving higher device performance.

2.5 Principles of outcoupling design in this thesis

In the rest of Part I, we will demonstrate four new light-extraction schemes for OLEDs, all of which are designed according to the following principles.

(1) Light extraction structures should not intrude into the device active region. To maintain the yield and the electrical characteristics of OLEDs, light extraction structures should be outside the active region and keep the electrical active region flat. The ideal light extraction structures should be embedded into the substrate, which boosts the device performance without introducing changes on the OLED deposition condition or electrical characteristics.

(2) The structure should be easy to fabricate and scalable. Photonic crystals or optical gratings are efficient to extract trapped light. However, these structures have a feature size of hundreds of nanometers, making the fabrication slow and expensive, not compatible with practical applications. For example, a commercial OLED lamp needs to be efficient and low-cost and the lighting panel has a size of ~10 m^2 during the fabrication stage. Slow fabrication processes of photonic crystals, such as electron beam lithography, make the product unprofitable.

(3) The optical structures should be independent on emission wavelength or viewing angles. The color uniformity across all viewing angles is an important standard for lighting lamps and displays screens. Furthermore, independence on the emission wavelength makes the OLED device design and fabrication easier

since there is no need to change the OLED active layers according to the light extraction structures.

Limited light extraction efficiency has been a universal problem for most luminescent materials and devices. Due to the wide applications of lighting and displays, the best ideas are necessarily the least complicated. In recent years, light extraction of OLED has been continuously improving. However, the most widely applied techniques may not be the ones guaranteeing the best device performance, as it must be simple and low-cost.

2.5 Reference

[1] C. W. Tang and S. A. VanSlyke, Appl. Phys. Lett. **51**, 913 (1987).

[2] C. Adachi, M. A. Baldo, M. E. Thompson, and S. R. Forrest, J. Appl. Phys. **90**, 5048 (2001).

[3] G. He, O. Schneider, D. Qin, X. Zhou, M. Pfeiffer, and K. Leo, J. Appl. Phys. **95**, 5773 (2004).

[4] S. R. Forrest, D. D. C. Bradley, and M. E. Thompson, Adv. Mater. **15**, 1043 (2003).

[5] H. Khosravi and R. Loudon, Proc. R. Soc. London. Ser. A Math. Phys. Sci. **436**, 373 (1992).

[6] H. Khosravi and R. Loudon, Proc. R. Soc. London. Ser. A Math. Phys. Sci. **433**, 337 (1991).

[7] J. E. Sipe, Surf. Sci. **105**, 489 (1981).

[8] W. L. Barnes, J. Mod. Opt. **45**, 661 (1998).

[9] R. R. Chance, A. Prock, and R. Silbey, J. Chem. Phys. **60**, (1974).

[10] K. Celebi, T. Heidel, and M. Baldo, Opt. Express **15**, 327 (2007).

[11] R. R. Chance, A. Prock, and R. Silbey, Adv. Chem. Phys **37**, 1 (1978).

[12] M. A. Baldo, D. F. O'Brien, Y. You, A. Shoustikov, S. Sibley, M. E. Thompson, and S. R. Forrest, Nature **395**, 151 (1998).

[13] W. Brütting, J. Frischeisen, T. D. Schmidt, B. J. Scholz, and C. Mayr, Phys. Status Solidi **210**, 44 (2013).

[14] A. Chutinan, K. Ishihara, T. Asano, M. Fujita, and S. Noda, Org. Electron. Physics, Mater. Appl. **6**, 3 (2005).

[15] V. Bulovic, V. B. Khalfin, G. Gu, P. E. Burrows, D. Z. Garbuzov, and S. Forrest, Phys. Rev. B. Condens. Matter **58**, 3730 (1998).

[16] L. H. Smith, J. A. E. Wasey, I. D. W. Samuel, and W. L. Barnes, Adv. Funct. Mater. **15**, 1839 (2005).

[17] S. Nowy, B. C. Krummacher, J. Frischeisen, N. A. Reinke, and W. Brütting, J. Appl. Phys. **104**, 123109 (2008).

[18] S. Möller and S. R. Forrest, J. Appl. Phys. **91**, (2002).

[19] Y. Sun and S. R. Forrest, Nat Phot. **2**, 483 (2008).

[20] T. Yamasaki, K. Sumioka, and T. Tsutsui, Appl. Phys. Lett. **76**, (2000).

[21] T.-W. Koh, J. A. Spechler, K. M. Lee, C. B. Arnold, and B. P. Rand, ACS Photonics **2**, 1366 (2015).

[22] K. M. Lee, R. Fardel, L. Zhao, C. B. Arnold, and B. P. Rand, Org. Electron. **51**, 471 (2017).

[23] S. Mladenovski, K. Neyts, D. Pavicic, A. Werner, and C. Rothe, Opt. Express **17**, 7562 (2009).

[24] T. Nakamura, N. Tsutsumi, N. Juni, and H. Fujii, J. Appl. Phys. **97**, (2005).

[25] S. Reineke, F. Lindner, G. Schwartz, N. Seidler, K. Walzer, B. Lüssem, and K. Leo, Mater. Res. Soc. Symp. Proc. **1212**, 17 (2010).

[26] S.-J. Lee and J. Cooper, Electron. Environ. 2008. ISEE 2008. IEEE Int. Symp. 1 (2008).

[27] J. Brodeur, R. Arguel, S. Hafezian, F. Barachati, and S. Kéna-Cohen, Appl. Phys. Lett. **113**, 41105 (2018).

[28] Z. B. Wang, M. G. Helander, J. Qiu, D. P. Puzzo, M. T. Greiner, Z. M. Hudson, S. Wang, Z. W. Liu, and Z. H. Lu, Nat. Photonics **5**, 753 (2011).

[29] T. Bocksrocker, J. B. Preinfalk, J. Asche-Tauscher, A. Pargner, C. Eschenbaum, F. Maier-Flaig, and U. Lemme, Opt. Express **20**, A932 (2012).

[30] Y. R. Do, Y. C. Kim, Y.-W. Song, C.-O. Cho, H. Jeon, Y.-J. Lee, S.-H. Kim, and Y.-H. Lee, Adv. Mater. **15**, 1214 (2003).

[31] M. Bremer, N. Beck, H. Lüder, and M. Gerken, in *Solid-State Org. Light.* (Optical Society of America, 2015).

[32] W. H. Koo, S. M. Jeong, F. Araoka, K. Ishikawa, S. Nishimura, T. Toyooka, and H. Takezoe, Nat Phot. **4**, 222 (2010).

[33] M. Slootsky and S. R. Forrest, Opt. Lett. **35**, 1052 (2010).

[34] S. Möller and S. R. Forrest, J. Appl. Phys. **91**, 3324 (2002).

[35] M. Slootsky and S. R. Forrest, Appl. Phys. Lett. **94**, 163302 (2009).

[36] H.-W. Chang, J. Lee, S. Hofmann, Y. Hyun Kim, L. Müller-Meskamp, B. Lüssem, C.-C. Wu, K. Leo, and M. C. Gather, J. Appl. Phys. **113**, (2013).

[37] C.-H. Chang, K.-C. Tien, C.-C. Chen, M.-S. Lin, H.-C. Cheng, S.-H. Liu, C.-C. Wu, J.-Y. Hung, Y.-C. Chiu, and Y. Chi, Org. Electron. **11**, 412 (2010).

[38] S. Jeon, S. Lee, K.-H. Han, H. Shin, K.-H. Kim, J.-H. Jeong, and J.-J. Kim, Adv. Opt. Mater. 1701349 (n.d.).

[39] T. D. Schmidt, D. S. Setz, M. Flämmich, J. Frischeisen, D. Michaelis, B. C. Krummacher, N. Danz, and W. Brütting, Appl. Phys. Lett. **99**, (2011).

[40] M. Flämmich, J. Frischeisen, D. S. Setz, D. Michaelis, B. C. Krummacher, T. D. Schmidt, W. Brütting, and N. Danz, Org. Electron. **12**, 1663 (2018).

[41] J. Frischeisen, D. Yokoyama, C. Adachi, and W. Brütting, Appl. Phys. Lett. **96**, 073302 (2010).

[42] T. D. Schmidt, T. Lampe, M. R. Daniel Sylvinson, P. I. Djurovich, M. E. Thompson, and W. Brütting, Phys. Rev. Appl. **8**, 1 (2017).

[43] M. J. Jurow, C. Mayr, T. D. Schmidt, T. Lampe, P. I. Djurovich, W. Brütting, and M. E. Thompson, Nat. Mater. **15**, 85 (2016).

[44] T. Lampe, T. D. Schmidt, M. J. Jurow, P. I. Djurovich, M. E. Thompson, and W. Brütting, Chem. Mater. **28**, 712 (2016).

[45] J. Kim, T. Batagoda, J. Lee, D. Sylvinson, K. Ding, P. J. G. Saris, U. Kaipa, I. W. H. Oswald, M. A. Omary, M. E. Thompson, and S. R. Forrest, Adv. Mater. **31**, 1900921 (2019).

[46] J. Song, K.-H. Kim, E. Kim, C.-K. Moon, Y.-H. Kim, J.-J. Kim, and S. Yoo, Nat. Commun. **9**, 3207 (2018).

Chapter 3

Enhanced Light Extraction from Organic Light-Emitting Devices Using a Sub-Anode Grid

In the last chapter, we recognize the roots of limited light-extraction in OLEDs, and review different outcoupling strategies employed in previous works. In this chapter, we demonstrate a simple and practical means to extract waveguided light.

3.1 Introduction

In this chapter, we demonstrate a sub-anode grid by inserting a planar grid layer consisting of two transparent materials with different refractive indices between the indium tin oxide (ITO) anode and glass substrate, as shown in Fig. 3.1(a). Outcoupling by this grid has minimal impact on wavelength, viewing angle and molecular dipole alignment [1], making it useful for a broad range of display and lighting applications. By positioning the grid *outside* of the device active region, this approach is unique in that it allows for complete freedom in varying its dimensions and materials from which it is made without impacting the optical and electrical characteristics of the device itself. Hence, both the grid and the OLED can be independently optimized to deliver the highest performance. We use full wave electromagnetic simulations to analyze the quantum efficiency dependence on the sub-anode grid geometric parameters and refractive indices, and show that the experimental results are consistent with simulations. The grid is effective in outcoupling almost all waveguided light into the substrate, improving the

substrate and air mode quantum efficiency (η_{SA}) from (33±2)% for conventional devices, to (40±2)%. Using a thick electron transport layer that decouples the waveguided light from lossy surface plasmon modes gives a (1.50±0.08) enhancement in η_{SA} compared to OLEDs lacking the grid.

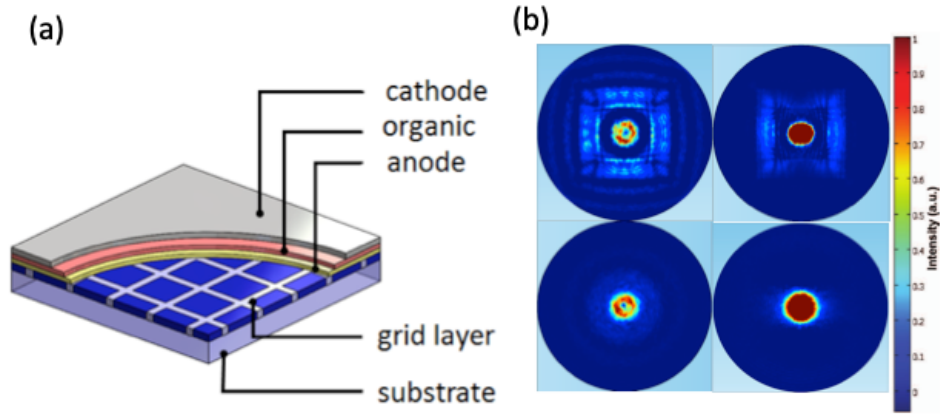

Figure 3.1 (a) Schematic cut-away view of an organic light emitting diode (OLED) with a sub-anode grid. (b) Polar plot of the simulated power intensity into the glass substrate for vertical and horizontal dipole orientations, with and without the sub-anode grid. For these simulations, refractive indices of the material in which the grid is embedded (n_{host}) and the grid itself (n_{grid}) are 2.2 and 1.5, respectively. Top left: vertical dipole emission for an OLED with the grid. Top right: horizontal dipole emission with the grid. Bottom left: vertical dipole emission without the grid. Bottom right: horizontal dipole emission without the grid.

3.2 Optical analysis

Using finite-element method analysis (COMSOL Multiphysics [2]), we investigated the OLED quantum efficiency dependence of a grid placed between the glass substrate and the ITO anode and that is comprised of a pair of materials with different refractive indices. The simulated device consists of a semi-infinite glass substrate, the sub-anode grid layer, a 70 nm thick anode, a 120 nm thick organic layer stack comprising the OLED active region, and a semi-infinite Al cathode with refractive indices at a wavelength of λ = 510 nm of n_{glass} = 1.5, n_{ITO} = 1.8, n_{org} = 1.7 and n_{Al} = 0.96+6.45i, respectively. For computational efficiency, the simulation domain was

restricted to a single sub-anode grid unit cell. Light emission is generated by a randomly oriented radiating molecular dipole placed at the center of the emissive region and decomposed into its vertical and horizontal components [3]. All power emitted from the dipole into the glass substrate is integrated in the half-space bounded by the reflecting cathode. This is used to calculate the enhancement in outcoupling due to the sub-anode grid, which is the ratio of the power in the substrate and air modes obtained using the grid, to that of a conventional device lacking the grid. To benefit from the outcoupling afforded by the grid, additional substrate outcoupling strategies must be employed; microlens arrays [4] provide the most efficient and cost effective technique for this purpose. Hence, for our analysis we assume that such methods are used to obtain the total enhancement in η_{EQE}.

The color maps in Fig. 3.1(b) show the radiated power intensity into the substrate with and without a $(5\ \mu m)^2$ square sub-anode grid surrounded by 1 μm grid lines. The refractive indices of the grid itself (n_{grid}) and the material in which it is embedded (the "host", with n_{host}) are 1.5 and 2.2, respectively. The majority of the photons radiated from vertical dipoles are trapped in the high index waveguide, while horizontal dipoles outcouple most of the power into the substrate in the azimuthal direction. Therefore, as shown in the polar radiation patterns in Fig. 3.1b, the enhancement due to the grid is more pronounced for vertical than for horizontal dipoles. In both cases, the waveguided optical power is scattered into the substrate at the inner edges of the grid.

In Fig. 3.2 we show the calculated dependence of enhancement on the refractive index difference ($\Delta n = n_{host} - n_{grid}$) of the grid and host materials. Here, η_{SA} is plotted *vs.* Δn, with each value of n_{host} indicated. Increasing the index contrast between the host and grid materials leads to enhanced scattering of trapped waveguide modes into the substrate. For this geometry,

the peak enhancement is 1.39 for n_{host} = 2.2 and n_{grid} = 1.2. The enhancements of a homogeneous layer with various refractive indices (at n_{host} = n_{grid}), shown in Fig. 3.2, inset, are much smaller than that for the sub-anode grid, indicating the increased outcoupling efficiency results from scattering rather than weak microcavity effects.

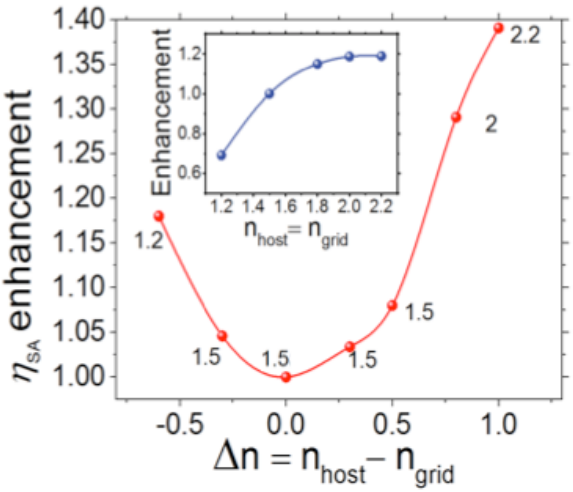

Figure 3.2 Substrate and air mode quantum efficiency (η_{SA}) enhancement dependence on host and grid material refractive index difference (Δn = n_{host} - n_{grid}), with each value of n_{host} indicated. Inset: Efficiency enhancement for OLEDs with different neat host material layers (i.e. n_{grid} = n_{host}) that underlie the transparent anode shown for comparison.

Using the relatively high-contrast combination of n_{host} = 2.2 and n_{grid} = 1.5, we then varied the grid layer thickness for two different patterns: (3 μm)^2 squares with 1 μm wide grid lines, and hexagons with 3 μm sides separated by 1 μm grid lines. From Fig. 3.3a we find that the 160 nm thick sub-anode grid layer thickness results in maximum outcoupling enhancements of 1.37 and 1.42 for both square and hexagonal grids, respectively.

Using a square grid with an optimum thickness of 160 nm, we examined the importance of grid line width and periodicity for n_{host} = 2.2 and n_{grid} = 1. The width was varied from 0.5 μm to 2.5 μm for periodicities of 3 μm and 5 μm. As the grid width increases, light extraction initially increases and reaches peak enhancements of 1.77 and 1.83, respectively. The

enhancement then decreases for grid widths exceeding half of their periodicities, as shown in Fig. 3.3(b).

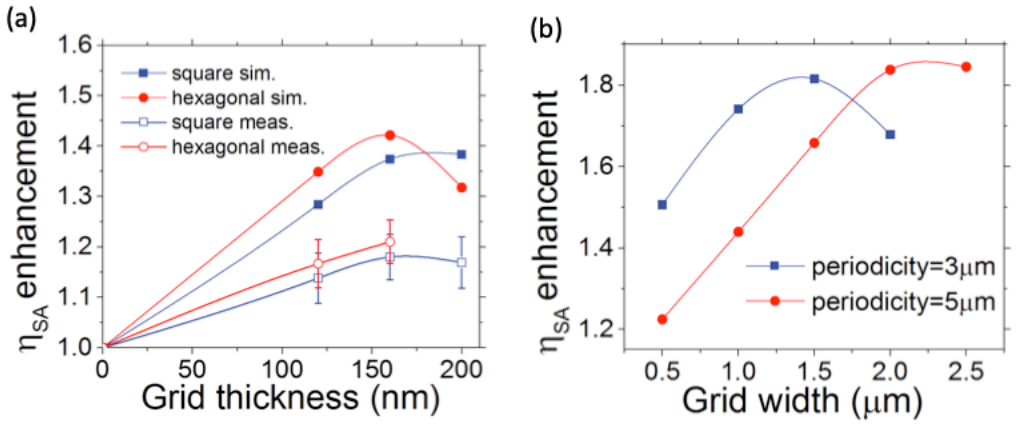

Figure 3.3 (a) Simulated (sim.) and measured (meas.) values of η_{SA} enhancement of square and hexagonal buried sub-anode grids *vs*. grid thickness. (b) Geometric pattern dependence on grid width, with periodicities of 3 μm and 5 μm, and n_{grid} = 1, n_{host} = 2.2. The differences between simulated and measured enhancements are due to coupling to surface plasmon modes not accurately accounted for in the simulations.

To study the origin of outcoupled optical power using the sub-anode grid, we compared the measured quantum efficiencies with the simulated power distribution assuming different ETL thicknesses for a conventional device. The detailed analytical solution employing Green's function analysis follows previous procedures [5–7] giving the results (curves) plotted in Fig. 3.5 for the device structures described in Ch. 2. The η_{EQE} increases to a peak of 16% as ETL thickness increases from 20 nm to 50 nm. Then, η_{EQE} decreases when the ETL thickness is >60 nm. As the ETL thickness is increased from 20 to 90 nm, the waveguide and substrate modes also increase.

3.3 Sub-anode grid fabrication

To achieve a high refractive index contrast between the grid and host materials while maintaining a smooth and planar scattering layer, two different fabrication processes have been developed as shown in Fig. 3.4. In both designs, TiO_2 is used as the high-index host (n = 2.2).

The low-index grid consists of either SiO_2 (n=1.5, "buried grid") or an air-filled void (n = 1.0, "air grid"). Three kinds of sub-anode grids were fabricated: $(3\ \mu m)^2$ square and 3 μm side-length hexagonal buried grids surrounded by 1 μm wide grid lines with thicknesses of 120 nm, 160 nm and 200 nm, and a $(3\ \mu m)^2$ square by 1 μm wide grid line by 160 nm thick air grid. A 340 nm thick, 3 μm side-length hexagonal grid by 1 μm wide grid line buried grid was also fabricated for combination with a 240 nm thick ETL PHOLED.

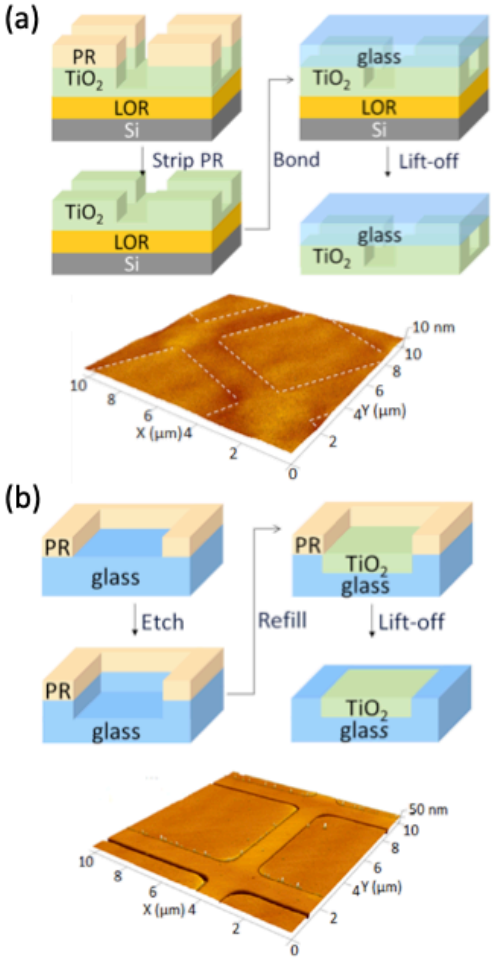

Figure 3.4 (a) The air sub-anode grid fabrication process also showing an atomic force microscope (AFM) image of the grid layer surface before ITO deposition. Dashed lines indicate the position of the grid. The root-mean-square (rms) roughness of the surface is 0.6 nm. (b) The buried grid fabrication process and the corresponding AFM image. The rms roughness of the surface is 1.1 nm. The step height between the glass and filling material is < 8 nm. Note the protrusions near the grid edges. Here, LOR and PR denote lift-off resist and photoresist, respectively.

The fabrication sequence for the air-grid is shown in Fig. 3.4a. A 200 nm thick TiO_2 film is deposited by e-beam evaporation on a Si wafer pre-coated with a 300 nm thick sacrificial lift-off resist (LOR) (MicroChem LOR 3A) (4000 rpm, 180^o C, 3 min). Photoresist (PR) (Microposit S1813) is subsequently spin-coated at 4000 rpm and cured at 105^o C for 90 sec. The grid pattern is photolithographically defined using an I-line AutoStep exposure system (GCA AS200) with exposure time of 0.33 sec, followed by partial removal of the TiO_2 to a depth of 160 nm by 32:10:8 sccm Cl_2:Ar:BCl_3 inductively-coupled plasma (LAM 9400) at 5 mTorr and 500W RF power with 100W bias. The PR is subsequently removed using oxygen plasma cleaning at 800W for 3 min. Since the etched depth is less than the total thickness of pre-deposited TiO_2 film, an overlayer is formed to flatten the surface. The Si wafer with the patterned film is cleaned using sonication in deionized (DI) water to remove residual particles, while the glass substrates are cleaned using acetone sonication and hot isopropanol. Both the TiO_2 and the glass substrates are treated with oxygen plasma to make them hydrophilic. A sodium silicate solution (Sigma-Aldrich) diluted to 2 vol.% with DI water is spin-coated on the glass substrate. Immediately, the glass and the TiO_2 film on the Si wafer are brought into contact and pressed by hand to form a bond to the glass [8]. Then the assembly is annealed at 20 MPa and 90° C for 1 hr, and cooled under pressure for ~12 hr. To remove the sacrificial LOR and release the TiO_2 film from the Si wafer, the assembly is diced into (15 mm)^2 squares, which are soaked in Remover PG (MicroChem) at 80°C to dissolve the sacrificial LOR to leave a covered air grid on the glass substrate.

The buried grid is fabricated directly on the glass substrate following the process in Fig. 3.4b. A bilayer photoresist (300 nm thick MicroChem LOR3A and 3 μm thick Shipley SPR220-3.0) is spun at 4000 rpm onto the pre-baked (200^o C, 5 min) glass substrate, lithographically

patterned (AutoStep, 0.33 sec exposure time), and developed to form an undercut profile that reduces sidewall deposition. The substrate is etched using a capacitively-coupled 1:1 CF_4:CHF_3 plasma (Plasmatherm 790) at 100W. The trench is imaged using AFM at several points in the process to achieve the desired depth. Then, TiO_2 is deposited by electron beam evaporation at 1 Å/s to a thickness equal to the etched depth to evenly fill in the openings in the SiO_2. A silicon blank is put alongside the PHOLED substrate to monitor the deposition thickness in real time. The refilling thickness error is reproducibly controlled to within 30 nm. The photoresist is lifted-off by dissolving the LOR as above. The residual photoresist is removed using oxygen plasma. Then the grid wafer is singulated into $(1.5\ cm)^2$ squares. We note that polishing following grid filling is also a potential means for achieving a planar surface prior to ITO deposition. Figure 3.4 also shows atomic force microscope images of both the air and buried grid surfaces.

The root-mean-square roughness of the two grids are 0.6 nm and 1.1 nm, respectively. The step height between the glass and buried grid material is < 8 nm. The slight troughs and peaks visible on either side of the grid result from shadowing and sidewall deposition. However, after annealing protrusions with heights ranging from 10 nm to 100 nm are found at the intersections of the air grid lines formed by differential expansion of the ITO and TiO_2 under low pressure. Despite these surface irregularities, PHOLEDs deposited onto both buried and air grid substrates exhibited ~70% yield.

After grid preparation, a 70 nm thick ITO layer is sputter-deposited in a chamber with an Ar pressure of 10^{-3} Torr at a rate of 0.6 Å/s, followed by annealing for 4 hr at 250° C. The ITO coated substrates are cleaned by sequential rinsing in acetone and hot isopropanol, followed by exposure to ultraviolet-ozone immediately prior to PHOLED layer deposition. Organic materials and metal cathodes are deposited by vacuum thermal evaporation at a base pressure of 5×10^{-7}

torr and at rates of 1-2 Å/s. The green PHOLED structure is as follows: 70 nm ITO/ 2 nm MoO_3/ 40 nm 4,4'-Bis(carbazol-9-yl)biphenyl (CBP)/ 15 nm 15 wt% tris(2-phenylpyridine)iridium(III) ($Ir(ppy)_3$) doped in CBP/ 65 nm 2,2',2''-(1,3,5-Benzinetriyl)-tris(1-phenyl-1-H-benzimidazole) (TPBi) ETL/ 1 nm LiF/ Al. Two devices with the same layer scheme are used for comparison with each sub-anode grid PHOLED: a conventional device and one with a neat TiO_2 layer underlying the ITO, and with the same thickness as that of the grid. The thick-ETL (240 nm) PHOLED with a 340 nm thick hexagonal buried sub-anode grid layer has the structure: grid layer/70 nm ITO/ 2 nm MoO_3/ 40 nm tris(4-carbazoyl-9-ylphenyl)amine (TcTa)/ 15 nm 15 wt% $Ir(ppy)_3$ doped in CBP/ 10 nm 4,7-diphenyl-1,10-phenanthroline (BPhen)/ 230 nm BPhen:Li/ Al.

The refractive indices of materials were measured using a variable angle spectroscopic ellipsometer (J. A. Woollam WVASE32). Current-voltage-luminance (*I-V-L*) characteristics were collected using a semiconductor parameter analyzer (HP-4156A) and a calibrated Si photodiode. The electroluminescence spectra were measured using an Ocean Optics (Winter Park, FL) miniature fiber-optics spectrometer. Index-matching fluid (IMF) with a refractive index of 1.508 was applied between the glass substrate and the Si photodiode to detect all photons in the air and substrate modes, thus eliminating the need for attachment of a microlens array while allowing a direct measurement of waveguide light extraction enhancement. Then η_{EQE} and η_{SA} were calculated using standard methods [9].

3.4 Experimental results

The current density-voltage (*J-V*) characteristics of all devices are identical over the PHOLED operating range from 0 V to 15 V (corresponding to current densities from 10^{-6} mA/cm^2 to 300 mA/cm^2), as shown in Fig. 3.6a. However, the air grid devices exhibited a significantly higher leakage at well below the turn-on voltage (V < 2.5 V), corresponding to dark

currents 0.01 to 0.1 mA/cm^2 compared to the other devices with ~10^{-5} to 10^{-3} mA/cm^2 over this same voltage range. The thick-ETL PHOLED give lower operating voltage than conventional devices at the same luminance.

To verify the simulated dependence on the sub-anode grid thickness, (3 μm)^2 squares and 3 μm side-length hexagonal buried grid devices η_{SA} were measured for grid thicknesses ranging from 120 nm to 200 nm and compared with simulations in Fig. 3.3a. Here, η_{SA} is measured using index-matching fluid between glass substrate and the detector surface to simulate results obtained using microlens arrays or other substrate mode outcoupling schemes. The measured and simulated dependences follow almost identical trends, although the absolute value of η_{SA} enhancement is lower for the measured devices than determined from simulations due to the overestimate of the outcoupling from surface plasmon modes (see below) in the latter case.

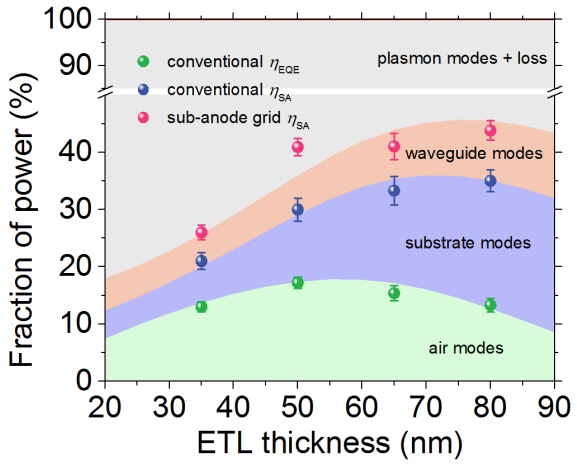

Figure 3.5 External quantum efficiencies (η_{EQE}) and η_{SA} of buried sub-anode grid PHOLEDs and conventional devices (data points) compared with the simulated power distribution of the conventional devices (curves) *vs.* electron transport layer (ETL) thickness using Green's function analysis.

Figure 3.5 shows the measured η_{EQE} and η_{SA} of conventional PHOLEDs compared to the η_{SA} of the 160 nm sub-anode grid devices (data points), along with the power distribution in devices as a function of ETL thickness (curves). The η_{SA} of sub-anode grid PHOLEDs is

comparable to the sum of the combined air, substrate and waveguide modes of conventional devices, indicating that the grid is effective in outcoupling waveguided optical power into the substrate. The external quantum efficiency, assuming efficient substrate mode outcoupling, is then the sum of the substrate plus air modes, with the sub-anode grid adding the waveguide modes to the total.

Figures 3.6b shows enhancements in η_{SA} relative to a conventional device at a current density of 1 mA/cm^2. These enhancements are approximately independent of the current (and hence brightness) over the operating range of the PHOLEDs from 0.1 mA/cm^2 to 100 mA/cm^2. We find that the efficiency enhancements of the conventional and the uniform TiO_2 sub-anode layer devices are nearly equivalent. Similarly, the two buried grid devices give almost the same efficiency enhancements, increasing from η_{SA} = (33±2)% for the conventional device, to (40±2)%, resulting in an increase in η_{EQE} from (15±1)% to (18±1)%. Since thick-ETL PHOLEDs have decreased coupling to plasmon modes [10], a 340 nm thick sub-anode grid substantially increases η_{SA} of an optimized control device with a 240 nm-thick ETL from (12±1)% to (18±1)%, corresponding to an enhancement of (1.50±0.08) in Fig. 3.6b.

The emission spectra of the devices in Fig. 3.6b are shown in Fig. 3.6c. The spectral peak of the device with the uniform TiO_2 layer is red-shifted by $\Delta\lambda$ = 40 nm from λ = 510 nm for the conventional device due to weak microcavity effects. None of the spectral peaks of the grid devices are shifted. A broader spectrum is observed in buried grid devices, also a result of minor microcavity effects. In contrast, the air grid device spectrum is slightly narrower than the control. The angular dependence of the emission intensity profile from sub-anode devices is a nearly perfect Lambertian, see Fig. 3.6d, indicating once again the presence of only very minor microcavity effects.

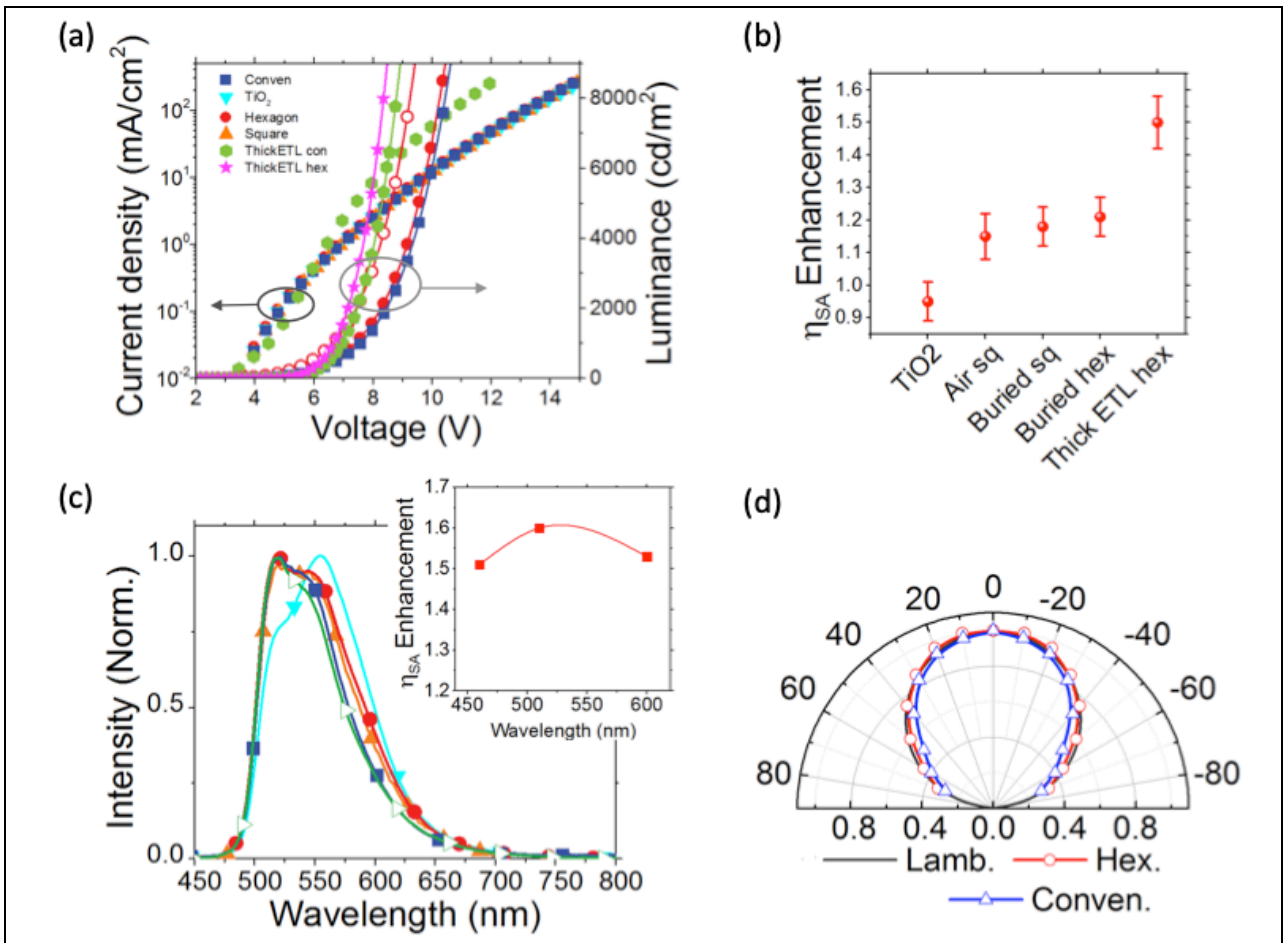

Figure 3.6 Device characteristics. (a) Current density-voltage (*J*-*V*, scattered makers) characteristics of conventional, TiO_2 control, buried hexagonal and square grid devices and thick ETL control device, and luminance-voltage (*L*-*V*, line-connected markers) of conventional, buried hexagonal with (hollow circles) and without (solid circle) index matching fluid and thick ETL devices with and without the buried hexagonal grid. (b) Enhancements in η_{SA} compared to a conventional PHOLED at J = 1 mA/cm^2, for a homogeneous TiO_2 layer, square buried and air grid, and buried hexagonal grids beneath the anode. Also shown is the enhancement of a 240 nm thick ETL buried hexagonal grid device, compared thick ETL conventional PHOLED. (c) Spectra of the PHOLED with a homogeneous TiO_2 sub-anode layer, square air (hollow triangles) and buried grid devices, and a buried hexagonal grid device. Inset: Enhancement in η_{SA} for a 245 nm thick grid for a white OLED, with spectral peaks at 460 nm, 510 nm and 600 nm. (d) Polar plot of luminous intensity of conventional devices (Conven.) and the device with the buried hexagonal grid (Hex.), compared with a Lambertian profile (Lamb.). The hexagonal grid and Lambertian profiles are indistinguishable. The angular error is 3^o.

The color dependence of the grid is further investigated by finite-element simulations. The calculated enhancement factor for a white OLED [11] is shown in Fig. 3.6c inset with a 245 nm thick square buried sub-anode grid and with a 70 nm thick ITO and 120 nm thick organic layer. Following previous white OLED designs, the distances of the blue, green and red emitters

to the metal surface are 40 nm, 60 nm and 70 nm, respectively [12]. As shown in Fig. 3.6c, inset, the enhancement factor is nearly constant at 1.57±0.04 across the visible wavelength range from 460 nm, to 600 nm.

3.5 Discussion

Since both η_{EQE} and η_{SA} of the conventional devices are equal to those of PHOLEDs with a uniform layer of TiO_2 positioned between the anode and the glass substrate, we conclude that the outcoupling enhancements only arise from scattering waveguide modes by the grids. The scattering is a consequence of the mismatch between waveguide modes in the microcavities formed by the organic, ITO layers and the grid. The refractive index difference between the grid and host materials controls the modal profiles within these two cavities: in the low index gridline region, the optical power is concentrated in the organic and ITO layers, whereas higher order waveguide modes are concentrated in the high index host region. As shown in Fig. 3.2, a larger index difference between the two materials comprising the sub-anode grid results in an increased outcoupling efficiency. The thickness of the grid is another parameter that determines the waveguide mode profiles. As shown in Fig. 3.3a, the simulated and measured relationship between outcoupling efficiency and the grid thickness share identical trends, despite the differences in the grid patterns (i.e. square and hexagonal).

The sub-anode grid outcouples nearly all power of the waveguide modes, as shown in Fig. 3.5. However, since the grid is positioned far from the cathode surface, it provides little perturbation to surface plasmon modes tightly confined at the organic-metal interface, making this significant fraction of power difficult to extract. This is clearly apparent in Fig. 3.3a, where the measured enhancement is ~15% lower than predicted from simulation. Since the surface plasmon mode power is mainly determined by the ETL thickness [13,14], to limit the excitation

of these modes by the waveguided light, the distance between the cathode and the emission layer must be increased. In our work we use a 240 nm thick ETL to ensure minimal coupling to plasmon polaritons. This results in a 50% increase in η_{SA} as shown in Fig. 3.6b, with the grid thickness, 340 nm, optimized for the chosen thicknesses of organic and ITO layers. An optimized optical structure is also achievable by tuning the thickness of hole transport layer (HTL) to manipulate the waveguide profiles within the two cavities, which provides an alternative means of tuning the spectrum, and to further reduce the color dependence of the sub-anode grid.

Contrary to expectations from the simulation in Fig. 3.2, η_{SA} is the almost same for air as for the buried grids, see Fig. 3.6b. The lower than expected quantum efficiency of devices with air grids results from leakage current caused by protrusions penetrating the ITO and overestimates of outcoupling from surface plasmon modes inherent to our calculational approach. The hexagonal and square buried sub-anode grid devices in Fig. 3.6b give nearly the same enhancements in η_{SA}, with hexagonal grids resulting in slightly higher η_{SA}, as predicted by full wave simulations in Fig. 3.3a. The advantage of the hexagonal sub-anode structure is that the distance that a waveguide mode travels from point of origin to the grid is nearly independent of propagation direction, resulting in an improved scattering efficiency compared to its loss.

The difference between the spectra of the devices in Fig. 3.6c results from weak microcavity effects. Due to the different refractive indices of SiO_2 and TiO_2 in the buried grid, broadening is observed in buried grid devices. In contrast, the lack of a shift and broadening in the air grid device results from air-filled void and the ~30 nm thick overlayer on top of the grid.

The variation in outcoupling efficiency is less than 10% across the visible spectrum (Fig.3.6c inset) and the Lambertian angular profile from the buried hexagonal grid in Fig. 3.6d,

that makes the sub-anode grid solution distinct from that of optical gratings. The lack of pronounced directional and wavelength effects indicates its compatibility with broad spectrally rich white light emission.

3.6 Summary

We demonstrated a method for extracting the waveguided light from the active regions of OLEDs using a non-diffractive, dielectric grid layer placed between the transparent conducting anode and the substrate. Full wave simulations result in optimized grid designs that maximize outcoupling in PHOLEDs. Buried dielectric and air sub-anode grids were fabricated by a combination of photolithography and wafer bonding prior to the deposition of the PHOLEDs. The sub-anode grid is shown to efficiently scatter nearly all waveguide mode power without introducing significant changes on the PHOLED emission wavelength and viewing angle. Importantly, since the grid lies below the anode, its design and fabrication is completely independent of the PHOLED structure and performance. This characteristic of the sub-anode grid allows complete freedom in materials and device structure needed to achieve a fully optimized emitting device. Hence, the grid provides a general and potentially very low cost solution to increased optical outcoupling, particularly when it is combined with simple means for extracting glass modes such as microlens arrays.

3.7 Reference

[1] J. Frischeisen, D. Yokoyama, C. Adachi, and W. Brütting, Appl. Phys. Lett. **96**, 073302 (2010).

[2] Computer program COMSOL Multiphysics (COMSOL AB, Stockholm, Sweden, 2013)

[3] M. Slootsky and S. R. Forrest, Appl. Phys. Lett. **94**, 163302 (2009).

[4] S. Möller and S. R. Forrest, J. Appl. Phys. **91**, (2002).

[5] K. Celebi, T. Heidel, and M. Baldo, Opt. Express **15**, 327 (2007).

[6] R. R. Chance, A. Prock, and R. Silbey, in *Adv. Chem. Phys.* (John Wiley & Sons, Inc., 2007).

[7] R. R. Chance, A. Prock, and R. Silbey, J. Chem. Phys. **60**, (1974).

[8] H. Y. Wang, R. S. Foote, S. C. Jacobson, J. H. Schneibel, and J. M. Ramsey, Sensors Actuators B Chem. **45**, 199 (1997).

[9] S. R. Forrest, D. D. C. Bradley, and M. E. Thompson, Adv. Mater. **15**, 1043 (2003).

[10] S. Mladenovski, K. Neyts, D. Pavicic, A. Werner, and C. Rothe, Opt. Express **17**, 7562 (2009).

[11] B. W. D'Andrade and S. R. Forrest, Adv. Mater. **16**, 1585 (2004).

[12] Y. Sun, N. C. Giebink, H. Kanno, B. Ma, M. E. Thompson, and S. R. Forrest, Nature **440**, 908 (2006).

[13] W. Brütting, J. Frischeisen, T. D. Schmidt, B. J. Scholz, and C. Mayr, Phys. Status Solidi **210**, 44 (2013).

[14] P. A. Hobson, J. A. E. Wasey, I. Sage, and W. L. Barnes, Sel. Top. Quantum Electron. IEEE J. **8**, 378 (2002).

Chapter 4

Elimination of Plasmon Losses and Enhanced Light Extraction of Top-Emitting Organic Light-Emitting Devices Using a Reflective Sub-Electrode Grid

4.1 Introduction

In the last chapter, we demonstrate sub-anode grids effectively extracting waveguide modes. Waveguide modes propagate tens of microns and can be efficiently scattered out of the device with appropriate outcoupling structures. In contrast, SSP modes are excited primarily in the metal cathode, and only propagate a few microns and dissipate before scattering [1]. Thus, suppressing SSPs while extracting waveguided power is a necessary strategy for achieving OLED external quantum efficiencies, $\eta_{EQE} > 70\%$. Unlike bottom-emitting OLEDs, top-emitting devices emit through a semi-transparent electrode into air and do not suffer from optical power trapping within the substrate. However, the higher reflectivity of the semi-transparent top electrode creates a strong optical cavity that introduces additional lossy waveguide modes along with undesirable angle and wavelength dependences of the emission spectrum [2]. Furthermore, since both electrodes in top-emitting devices are often comprised of metal, it is not possible to entirely suppress SPP modes using thick organic layers without also lowering efficiency [3]. In this chapter, we demonstrate an outcoupling scheme for top-emitting diodes by replacing both anode and cathode with indium zinc oxide (IZO)/MoO_3 transparent contacts, and placing a

reflective and scattering corrugated metal-coated dielectric mirror beneath the electrically active organic region. This is combined with a low refractive index anti-reflection (AR) layer to reduce microcavity effects.

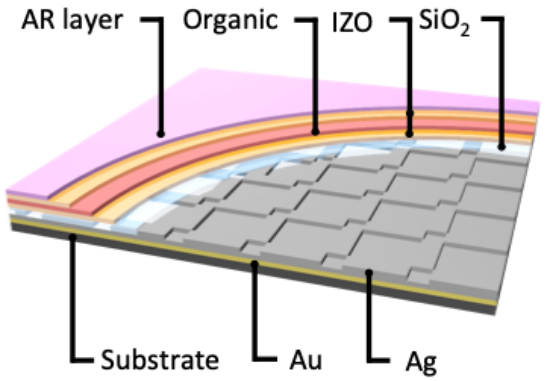

Figure 4.1 Schematic cut away view of top-emitting organic light emitting devices (TEOLEDs) with indium zinc oxide (IZO)/MoO_3 electrodes and a metal coated sub-anode grid.

4.2 Optical analysis

A schematic diagram of the device is shown in Fig. 4.1. The design spaces the active region away from the metal reflector to minimize coupling to SPP modes while scattering out the waveguided optical power without disturbing the planarity of the device itself. Employing a scattering structure within the substrate while retaining a planar substrate surface allows complete freedom for optimizing the scattering layer dimensions without affecting the electrical properties of the OLED. The Ag reflector is a patterned grid of raised rectangles whose periodicity is on the order of several wavelengths to avoid angle and wavelength dependent effects. A dielectric spacer fills in the depressions and extends above the rectangular grid, providing a planar surface for the subsequent deposition of the electrodes and organic layers. The thick and thin spacer regions couple differently to the microcavity modes by locally creating both a thick and thin cavity regions beneath the electrode.

We investigate SPP coupling in the thick and thin cavities by calculating the local electric field of the plasmon mode at the EML, $\boldsymbol{E}(z)$. The emission rate into the SPP mode is found using Fermi's Golden rule:

$$\Gamma(\omega) = \frac{2\pi}{\hbar} |\langle i|\boldsymbol{d} \cdot \boldsymbol{E}(z)|f\rangle|^2 \rho(\omega) \tag{4.1}$$

where $\boldsymbol{d}$ denotes the exciton dipole moment, i and f the initial and final exciton state wavefunctions, and $\rho(\hbar\omega)$ the plasmonic mode density. The distance of the exciton from the metal interface is z, and $\boldsymbol{E}(z)$ is the electrical field of the SPP mode normalized to a half quantum for zero-point fluctuations [11].

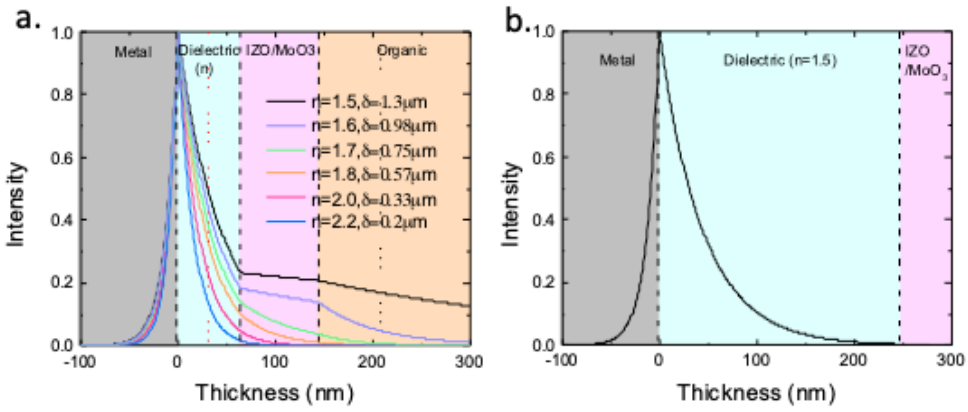

Figure 4.2 (a) Surface plasmon mode magnetic field intensity across the control device structure with different refractive indexes, *n*. Also shown is the surface plasmon polariton (SPP) mode propagation length, δ. The structure is Ag/65nm dielectric with variable *n*/60nm IZO and MoO_3/organic layers (gridline area of the metal coated grid). Emission layer position is denoted by the red dotted line. (b) Field intensity over deeper grid region, with dielectric layer thickness of 245 nm and *n*=1.5 (depression area of the metal coated grid)

The magnetic field intensity profiles of SPP modes in the OLED cavities are shown in Fig. 4.2a and b, found using the dispersion relation:

$$k_{spp}^2 = \frac{\varepsilon_m \varepsilon_d}{\varepsilon_m + \varepsilon_d} \left(\frac{2\pi}{\lambda}\right)^2 \tag{4.2}$$

where wavelength λ = 510 nm. For this calculation, we assume a semi-infinite metal layer having a dielectric constant ε_m [12] in contact with a semi-infinite dielectric layer with dielectric constant, ε_d.

Figure 4.2a shows the calculated mode profiles in the regions where the cavity is thin (corresponding to the areas where the grid lines are raised) for different values of the index of refraction of the spacer layer, *n*. The active region used in simulating this structure is 130 nm-thick organic layers (n_{org} = 1.8) sandwiched between 80 nm-thick transparent electrodes (50 nm IZO and 30 nm MoO_3, $n_{IZO} = n_{MoO3}$ = 2), with the emission layer (EML) placed at 60 nm above the bottom electrode. Since the grid spacing is too large to act as an optical grating, the spacer thicknesses are chosen to match the two cavity resonances to the desired emission wavelength. The cavity resonant wavelength, λ_r, normal to the substrate scales approximately linearly with spacer thickness. Thus, the chosen thicknesses of the SiO_2 spacer layer are 65 nm for the thin cavity regions, and 245 nm for the thick cavity in regions between the grid rectangles, resulting in a grid depth of 180 nm. Both thicknesses give $\lambda_r \approx$ 540 nm, which is optimal for a green emission spectrum.

The calculated propagation lengths of SPP modes ($\delta_{SPP} = 1/[2\mathrm{Im}(k_{SPP})]$) are also shown in Fig. 4.2a. Both the field intensity in the EML whose position is denoted by the black dotted line, and the propagation length decrease as the refractive index of the spacer layer increases. For comparison, the red dotted line indicates the distance from the EML to the metal in a conventional top-emitting OLED (TEOLED). In that case, local field of the SPP mode in the EML is larger than in our design (black dotted line), leading to faster exciton coupling rate to SPPs. In Fig. 4.2b, we observe that the SPP decays before reaching the organic layers in a thick cavity with *n* = 1.5. The coupling to SPP modes decays exponentially as the distance increases

between the EML and metal surface. Thus, SPP coupling can be avoided with nonmetallic electrodes and the appropriate choice of spacer material and thickness.

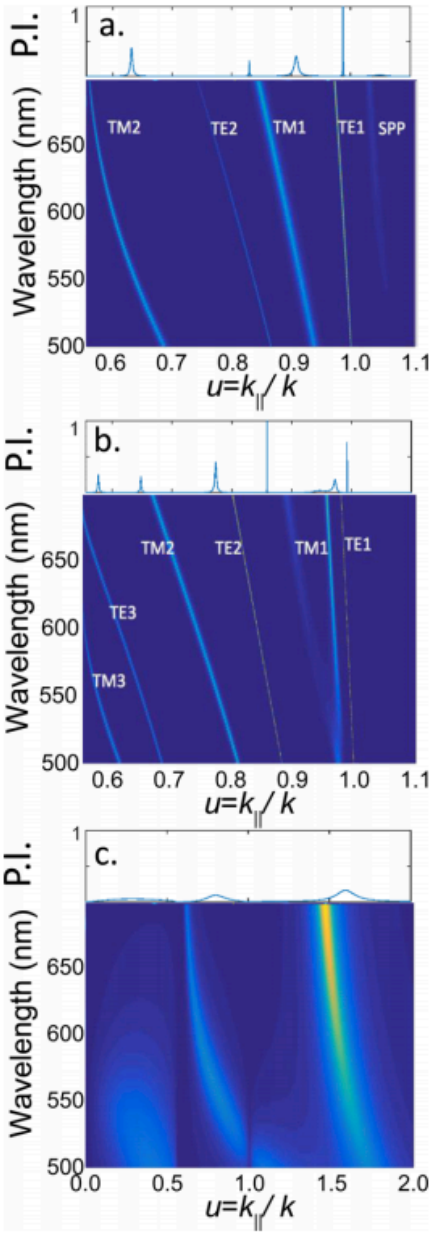

Figure 4.3 The modal power distributions within the cavities. The waveguide modes, and SPP modes at $u > n_{air} / n_{org}$, of the cavities over the (a) gridlines and (b) depression. (c) The power distribution of a conventional TEOLED optimized over the same spectral range, with the structure Ag/90 nm organic layers/20 nm-thick top Ag layer, with a 20 nm EML centered in the organic active region. The plots above each color map are the power distributions at a wavelength of λ = 540nm.

The simulated modal power distributions of the cavities using Green's function analysis [13,14] are shown in Fig. 4.3 a and b. We define u as the ratio of the in-plane

component of wavevector, $k_{||}$, for light propagating in the organic layers with refractive index of n_{org}, to the total wavevector k, *i.e.* $u = k_{||} / k$. Thus, the region $u > 1$ corresponds to evanescent waves in the near field. Usually, modes with $u < n_{air} / n_{org}$ are radiative, $n_{air} / n_{org} < u < 1$ are waveguided, and modes in the region $u > 1$ are SPPs. For the thin cavity, there are four waveguide modes in the emission spectrum, and a weak SPP mode. The thick cavity adds three more waveguide modes but has no SPP modes. Figure 4.3c shows the power distribution of a conventional TEOLED optimized over the same spectral range, with the structure Ag/90 nm organic layers/20 nm-thick top Ag layer, with a 20 nm-thick EML centered in the organic active region. This structure does not support waveguide modes, but has two SPP modes. The first SPP mode at $u \approx 0.6$ and $\lambda \approx 540$ nm is supported by the top thin Ag film. According to Eq. 4.2 and given $n_{air} < n_{org}$, this SPP mode lies in the region of $u < 1$ rather than $u > 1$ for organic/metal SSPs. The second SPP mode supported by Ag/organic interface lies at $u > 1.5$. Figures 4.3 shows that, compared to conventional devices, both the control and metal coated grid devices successfully suppress SPP modes while coupling more power into the waveguide modes.

The scattering by the grid is a consequence of the mismatch between the waveguide modes supported by the two cavities above the grid lines and depressions, which can be estimated by the overlap of the wavevectors of these modes. The third and forth modes in the thin SiO_2 cavity (Fig. 4.3a) have some overlap with the fifth and seventh modes in the thick cavity (Fig. 4.3b), and thus these modes are inefficiently scattered. The modes that are not aligned between cavities are scattered by the grid. The spacer thicknesses determine the mismatch of the modes, but freedom to optimize the spacer thickness is limited when matching the cavity resonance to the OLED emission spectrum.

The simulated output of a dipole in the thin SiO_2 cavity regions using Green's function analysis [13,14], shown in Fig. 4.4a, is strongly angle dependent. The spectral peak wavelength ranges from $\lambda = 545$ nm normal to the plane (0^o), to $\lambda = 460$ nm at 90°. A 70 nm thick low refractive AR layer between air and the top IZO electrode reduces the cavity effects, as is apparent by the spread in wavelength emission and reduced blue shift with angle in Fig. 4.4b. An example AR coating material is MgF_2 whose refractive index is $n_{MgF2} = 1.38$ in the range of the emission spectrum, close to the optimized value of $n = 1.4$ for IZO/air interfaces.

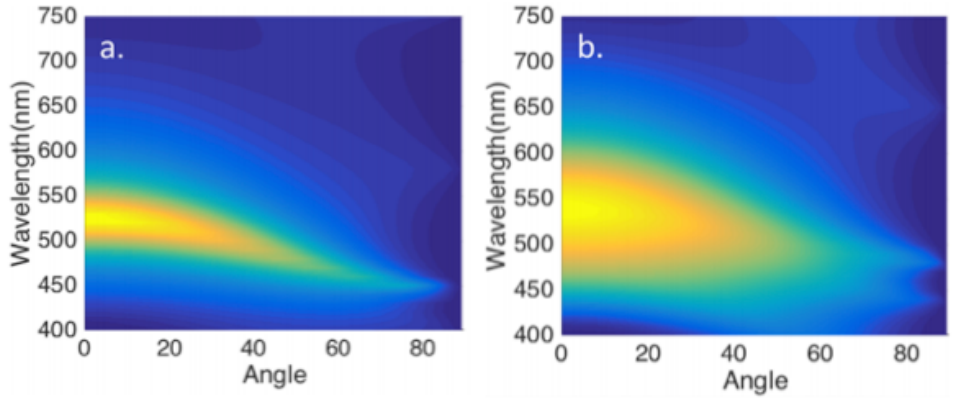

Figure 4.4 Simulated angle and wavelength dependence of the control device (a) without and (b) with a 70 nm thick low refractive ($n = 1.37$) anti-reflection (AR) coating. The device with the AR coating shows a broader spectrum and smaller blue shift at larger angles.

4.3 Sub-electrode metal grid fabrication

The fabrication sequence for the metallic scattering layer is shown in Fig. 4.5. A 245 nm SiO_2 film was deposited by electron-beam evaporation on a glass substrate pre-coated with sacrificial lift-off resist (MicroChem LOR 10B) (4000 r.p.m., 180°C). Photoresist (Microposit S1813) was subsequently coated at 4000 r.p.m. and cured at 115°C for 90 s. The pattern was photolithographically defined using an AutoStep exposure system (GCA AS200) with an exposure time of 0.33 s. The 180 nm deep etch of the SiO_2 film was done using a 1:1 CF_4: CHF_3

plasma at 100 W. The photoresist was removed by exposure to oxygen plasma for 3 min at 800 W. Then a 150 nm thick Ag film was deposited by thermal evaporation after a 2 nm thick Ti wetting layer. Next a 5 nm thick Ge wetting layer and a 200nm thick Au film were simultaneously deposited onto the surface of a clean glass substrate and the Ag-coated/SiO_2/glass substrate by electron-beam evaporation at 10 Å/s. The two glass substrates were then sealed together via cold-weld bonding [15] by applying heat (200° C) and pressure (4 MPa) for 5 min under vacuum (10^{-3} Torr) using an EVG 510 wafer bonder. The bonding is sufficiently robust to survive sonication although the Au surface on the grid is irregular due to the SiO_2 trenches, leaving vacancies at the bonding interface. The bonded glass slabs are diced into 1×1 inch squares, which were soaked in Remover PG (MicroChem at 80° C) to dissolve the sacrificial LOR layer to leave the metallic coated grid. After the grid preparation, a 50 nm thick IZO layer was deposited at 60 W in a chamber with an Ar pressure of 2 mTorr at a rate of 0.6 Å/s using a radio-frequency magnetron sputterer.

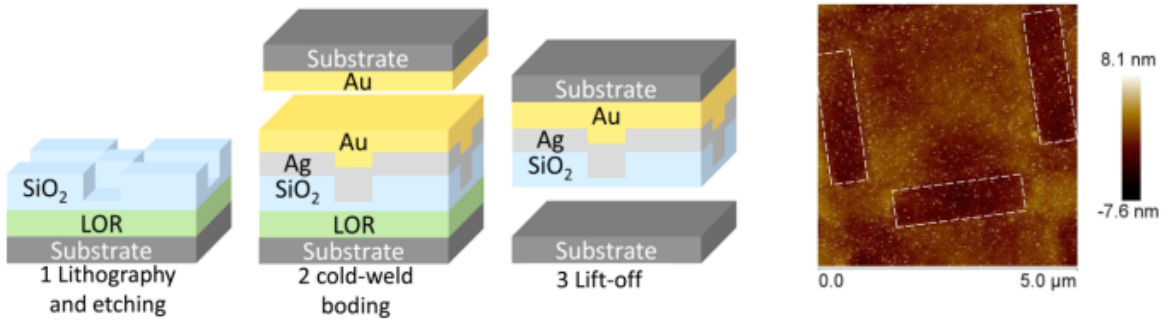

Figure 4.5 Fabrication sequence of the metal coated grid, and atomic force microscope image of the grid surface. There is deformation over the grid line area, and the root mean square surface roughness is 1.2 nm. The height difference due to the deformation is <5 nm.

The control substrate is prepared as follows: A glass substrate was cleaned using sonication in tergitol, de-ionized water, acetone, and isopropanol (IPA). A 2nm thick Ti wetting layer and 150 nm thick Ag layer were sequentially deposited by thermal evaporation, followed

by a 65 nm thick SiO_2 film by electron-beam evaporation, and 50 nm thick IZO by sputtering (23 ohm/sq). The area was defined by a shadow mask without breaking vacuum between depositions.

The IZO-coated substrates were cleaned for 3 min by sonication in IPA and exposed to ultraviolet-ozone before PHOLED layer deposition by vacuum thermal evaporation in a system with a base pressure of 10^{-7} torr. The first MoO_3 layer was deposited at 0.5 Å/s, and the top MoO_3 layer at 0.05 Å/s for the first 5 nm and at 0.2 Å/s for the remaining thickness in the same chamber as the organic layers. The top IZO electrode was sputter-deposited in a chamber with an Ar pressure of 5 mTorr at 0.05 Å/s for the first 10nm, and 2 mTorr at 0.2 Å/s for the remaining thickness. Finally, the MgF_2 capping layer was thermally deposited.

The refractive indices and thicknesses of materials were measured using a variable-angle spectroscopic ellipsometer (J. A. Woollam WVASE32). Current-voltage-luminance characteristics were collected using a semiconductor parameter analyzer (HP-4156A) and a calibrated Si photodiode. The electroluminescence spectra were measured using an Ocean Optics miniature spectrometer. The η_{EQE} was calculated using standard methods [16].

4.4 Experimental results

We fabricated an OLED using IZO/MoO_3 electrodes (control) and a device with a metal coated grid having the same active layer, as follows, starting from the substrate: 50 nm IZO/30 nm MoO_3/30nm 4,7-diphenyl-1,10-phenanthroline (BPhen): Li (molar 1:1)/30 nm BPhen/30 nm $Ir(ppy)_3$ doped at 8 vol% in 4,4′-bis(carbazol-9-yl)biphenyl (CBP)/40 nm 4,4′-cyclohexylidenebis[N, N-bis(4-methylphenyl)benzenamine] (TAPC)/30 nm MoO_3/50 nm IZO. The bottom MoO_3 layer planarizes protrusions left from the grid lithographic process that emerge through the spacer layer. The top MoO_3 layer prevents damage to the organic active

region during the IZO sputtering process. The control device has a 150 nm thick, planar Ag layer covered with 65 nm SiO_2 spacer layer beneath the active region. The grid reflector is an array of 1×3 μm raised rectangles surrounding 3×3 μm and 1×1 μm square depressions, with the spacer thicknesses given above. Both devices are capped with a 70 nm thick MgF_2 AR coating. The current density-voltage curves of both devices are identical above turn on (~3V) as shown in Fig. 4.6a. Furthermore, η_{EQE} is increased from 20±1% to 30±2% using the metallic scattering grid, as shown in Fig. 4.6b. The angular intensity profiles of the devices with the AR layer are broadened from a simple Lambertian emission profile. The peak intensity of the control device is normal to the surface, whereas the grid OLED intensity is at a maximum at 20° from normal. The spectra of the control (Fig. 4.6c) and the metal coated grid (Fig. 4.6d) OLEDs are shown at 0°, 30° and 60°. Both devices have spectral peaks at $\lambda \approx 550$ nm. Compared with the control, the grid device shows a slightly increased blue shift at large angles.

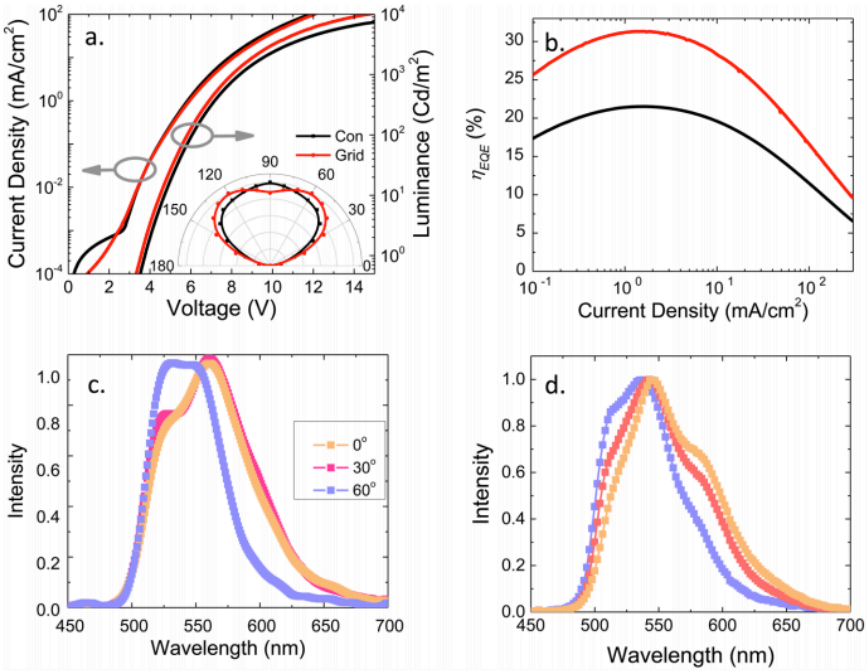

Figure 4.6 (a) Current density-voltage characteristics and (inset) the angular intensity profiles of the control (black) and metal coated grid (red) devices. (b) External quantum efficiencies of the control and metal coated grid devices. The emission spectra of the (c) control and (d) grid device with a MgF_2 AR coating at 0°, 30°, 60° with 2° error.

4.5 Discussion

The emission intensity is a function of the overlap between the cavity resonance and the emission spectrum. The microcavity resonance peak (at $\lambda \approx 540$ nm, see Fig. 4.6) is redshifted from the emission spectral peak ($\lambda \approx 510$ nm). Thus, the blue shift with angle results in broader than the Lambertian angular intensity profiles for the control and grid devices shown in Fig. 4.5a, inset. The broadening of the grid OLED spectrum is more severe because the capping layer thickness, which reduces the cavity quality, was optimized for the thin cavity region of the grid devices, which is the same as the spacer layer thickness used in the control device.

Although a significant enhancement in efficiency is obtained using the reflecting grid, 60% of the optical power is still lost in the device. In addition to the limited grid scattering

efficiency due to the spacer thickness used, the scattered light incurs losses at each reflection from the metal surface. A diffuser film or MLA comprised of high refractive index materials added to the top surface of the control devices should also generate higher efficiencies by reducing the cavity quality factor. The weaker cavity produced by these strategies is also beneficial for outcoupling white light. Using the fact that a MLA foil extracts more than half of optical power going into the foil, the Green's function analysis shows MLA on the device emitting surface could further improve the efficiency by 30% at least.

4.6 Summary

A top-emitting device with IZO/MoO_3 electrodes has achieved η_{EQE} = 20±1%, with almost no excitation of SPP modes. The efficiency is increased to 30±2% by using a metal coated scattering grid layer beneath the anode without impacting the OLED electrical characteristics. The efficiency can be further improved using MLA or diffuser on the device emitting surface. The grid scatters the waveguided power and reduces plasmonic losses. The metallic scattering grid is fabricated within the substrate, and hence is totally separate from the organic active layers, allowing for considerable freedom in both the OLED and grid optical designs. Note that if the insulating spacer layer is replaced with a low resistance transparent metal oxide, it can be used as a conductive layer used for addressing OLED pixels in an active matrix display. This is just one of several possibilities allowed by this sub-electrode light scattering approach.

4.7 Reference

[1] H.-W. Chang, J. Lee, S. Hofmann, Y. Hyun Kim, L. Müller-Meskamp, B. Lüssem, C.-C. Wu, K. Leo, and M. C. Gather, J. Appl. Phys. **113**, (2013).

[2] M. C. Gather and S. Reineke, J. Photonics Energy **5**, 57607 (2015).

[3] S. Hofmann, M. Thomschke, P. Freitag, M. Furno, B. Lüssem, and K. Leo, Appl. Phys. Lett. **97**, (2010).

[4] T. Schwab, S. Schubert, S. Hofmann, M. Fröbel, C. Fuchs, M. Thomschke, L. Müller-Meskamp, K. Leo, and M. C. Gather, Adv. Opt. Mater. **1**, 707 (2013).

[5] C. Fuchs, P.-A. Will, M. Wieczorek, M. C. Gather, S. Hofmann, S. Reineke, K. Leo, and R. Scholz, Phys. Rev. B **92**, 245306 (2015).

[6] T. Schwab, S. Schubert, L. Müller-Meskamp, K. Leo, and M. C. Gather, Adv. Opt. Mater. **1**, 921 (2013).

[7] T. Schwab, C. Fuchs, R. Scholz, X. Li, F. Xie, W. Choy, K. Leo, and M. C. Gather, Proc. SPIE **8829**, 88291I (2013).

[8] W.-Y. Park, Y. Kwon, C. Lee, and K.-W. Whang, Opt. Express **22**, A1687 (2014).

[9] C.-J. Yang, S.-H. Liu, H.-H. Hsieh, C.-C. Liu, T.-Y. Cho, and C.-C. Wu, Appl. Phys. Lett. **91**, (2007).

[10] M. Thomschke, S. Reineke, B. Lüssem, and K. Leo, Nano Lett. **12**, 424 (2012).

[11] I. Gontijo, M. Boroditsky, E. Yablonovitch, S. Keller, U. K. Mishra, and S. P. DenBaars, Phys. Rev. B **60**, 11564 (1999).

[12] A. D. Rakić, A. B. Djurišić, J. M. Elazar, and M. L. Majewski, Appl. Opt. **37**, 5271 (1998).

[13] K. Celebi, T. Heidel, and M. Baldo, Opt. Express **15**, 327 (2007).

[14] R. R. Chance, A. Prock, and R. Silbey, J. Chem. Phys. **60**, (1974).

[15] K. Lee, K.-T. Shiu, J. D. Zimmerman, C. K. Renshaw, and S. R. Forrest, Appl. Phys. Lett. **97**, (2010).

[16] S. R. Forrest, D. D. C. Bradley, and M. E. Thompson, Adv. Mater. **15**, 1043 (2003).

Chapter 5

Efficient, Non-Intrusive Outcoupling in Organic Light Emitting Devices Using Embedded Microlens Arrays

In the last two chapters, we demonstrated light extraction structures for both top and bottom emitting OLEDs. However, both structures need minor modification for different emission wavelengths to achieve optimal performance. Here we demonstrate a simple, efficient and wavelength-independent method for extracting trapped light from the active region into the air and substrate modes by embedding a microlens array between the transparent electrode and the glass substrate.

5.1 Introduction

The sub-electrode microlens array (SEMLA) shown in Fig. 5.1a consists of a flat spacer layer on top of a hexagonal closed-packed array of 10 μm diameter hemispherical lenses with refractive index $n_{SEMLA} = 1.8$. The microlens trenches in the glass substrates, in Fig. 5.1b, show the shape of the SEMLA. The lenses are closely packed leaving no flat plateau area in between. The SEMLA surface is smooth, meaning no optical scattering resulting from the structure. The dimensions are based on previous studies [1] with no further optimization shown in this report. The structure does not intrude into the device active region, and hence places no constraints on the design of the OLED itself. The lens array is fabricated using conventional photolithography

while being much smaller than a display pixel size (typically > 30 μm). Figure 5.1b shows a glass substrate containing the SEMLA structure (highlighted by dashed lines) on a printed background, with no apparent impact on the image sharpness. Figure 5.1(b), inset, shows a microscopic image of a section of a glass substrate covered by the SEMLA structure. The substrate is patterned with a square grid with 100 μm period and 20 μm wide metal gridlines, which is comparable to a mobile phone display pixel size. The SEMLA has negligible impact on image resolution when magnified at this level.

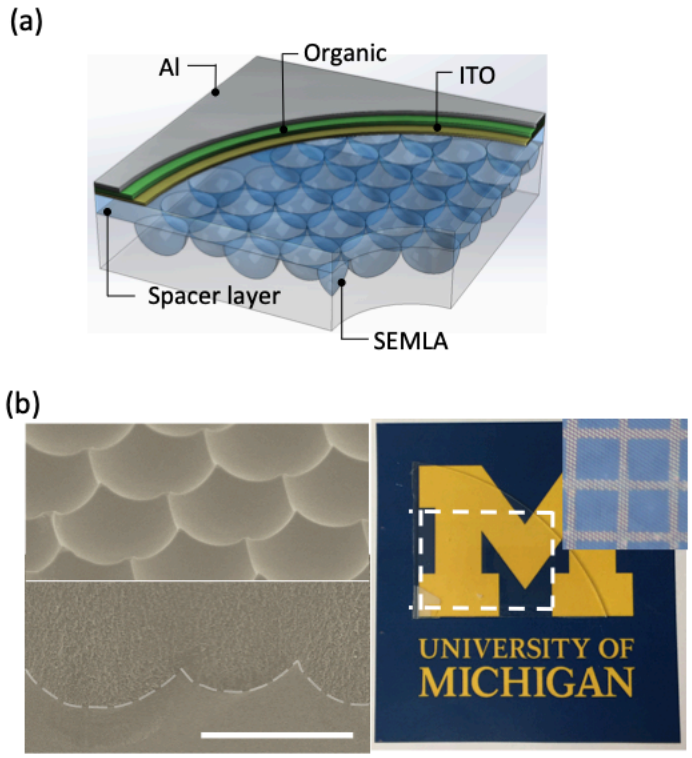

Figure 5.1 (a) Schematic illustration of devices on a sub-electrode microlens array (SEMLA) substrate. (b) Left: A scattering electron microscope image of the microlens-shape trenches in glass substrates (upper) and an image of cross section of a SEMLA substrate with a dashed line highlighting the interface of the SEMLA (bottom). Right: Image of a SEMLA substrate on a printed image, with the microlens side facing the image. The white dashed lines enclose the SEMLA structure area. *Inset*: A microscopic image of a SEMLA on top of a substrate patterned with a square grid with 100 μm pitch and 20 μm wide gridlines.

5.2 Optical analysis

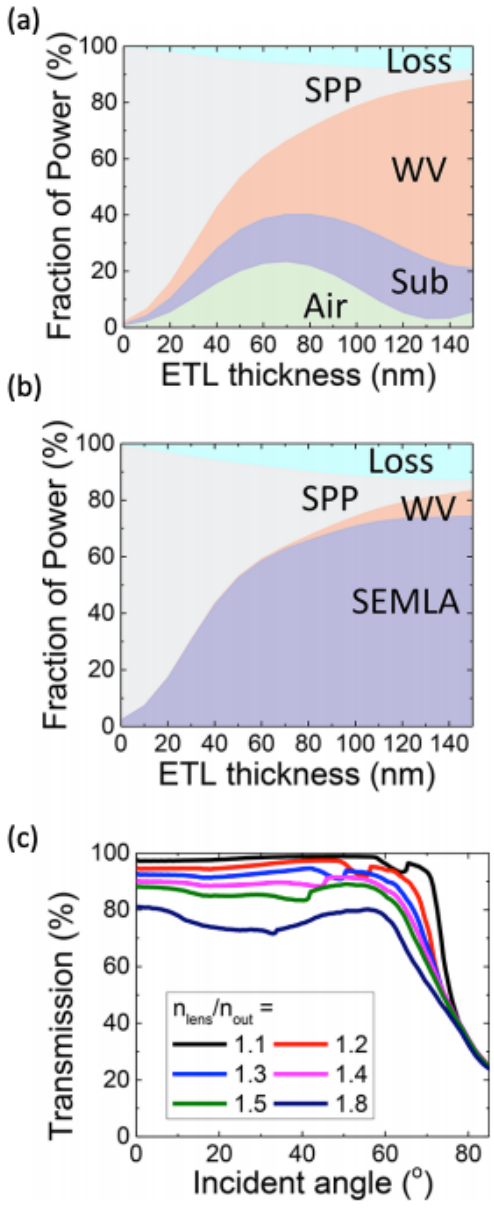

Figure 5.2 Optical power modal analysis *vs.* electron transport layer (ETL) thickness on (a) a conventional glass substrate and (b) a SEMLA substrate. (c) Ray tracing simulation results for the transmission through microlens (n_{lens}) to the medium in which it is embedded (n_{out}) increases *vs*. incident angle to substrate normal.

Optical modal analysis assumes that an emitting dipole (wavelength of 540 nm) is located in the center of the emissive layer with a thickness of 20 nm and refractive index of 1.83. The emitting dipole has 77% horizontal and 23% vertical component emission due to dipole

alignment of the green dopant material bis[2-(2-pyridinyl-N)phenyl-C](2,4-pentanedionato-O2,O4)iridium(III) ($Ir(ppy)_2acac$). The thicknesses and refractive indexes of each layer are: 40 nm thick ITO with $n = 2.1$, 40 nm thick hole transport layer with $n = 1.70$, emissive and electron transport layers with $n = 1.78$, and Al with a complex index of $n = 0.6+2.8i$. The SEMLA and polymer planarization layers (both made of NOA 170, Norland Products Inc.) have $n = 1.8$. All indices of refraction above were measured with ellipsometry. The glass refractive index is $n = 1.45$.

For the ray tracing simulations, the geometry in the simulation was a hexagonal array of close-packed hemispherical microlenses with an ITO, an organic layer and a reflective metal surface on its planar surface. The refractive index of the ITO and organic materials are identical to that of the microlenses, so no wave calculation or refraction was considered between the microlens-substrate interface and the metal surface. A 3% loss per pass through the ITO and 8% loss per reflection at the metal surface were assumed. The light was assumed to be unpolarized. At each incidence angle, the transmission was calculated for >1000 rays evenly distributed over a unit cell, and originating from within the organic layer. The azimuthal dependence was averaged to provide the transmission as a function of polar angle. To improve the computation speed, rays with a remaining relative intensity of < 0.5% were eliminated.

The high refractive index of the SEMLA extracts waveguide modes from organic and ITO anode layers. Figures 5.2 a and b show the calculated optical power distribution in the devices with and without the SEMLA based on Green's function analysis, assuming that the spacer layer is semi-infinite. The device structure used in the calculation is the following: 40 nm ITO anode/40 nm hole transport layer/20 nm emission layer/electron transport layer/Al cathode. For the SEMLA refractive index of $n_{SEMLA} = 1.8$, the waveguide modes are reduced to almost

zero for an electron transport layer thickness < 70 nm, with the SEMLA structure extracting all radiated optical power except for the surface plasmon modes. The optical power exits into the glass substrate from the high index hemispherical microlens array. The light extraction from the SEMLA into glass (n_{glass} = 1.45) is more efficient than from an external MLA (n_{MLA}= 1.4 -1.5) into air (n_{air} = 1) due to reduced reflection at the lens/glass interface with its larger critical angle. This behavior has been verified by a ray tracing simulation, with results in Fig. 5.2c. The discontinuities in the transmission spectra result from total internal reflection at the flats between the lenses. As the ratio of refractive indices of the microlens (n_{lens}) to the medium in which it is embedded (n_{out}) increases, the transmission at all incident angles decreases. Thus, n_{SEMLA} is chosen to be high enough to suppress waveguide modes in the organic and ITO layers, but not so high that the array itself becomes waveguiding. Air gaps between the substrate and the MLA as demonstrated previously, [2] increase reflections, and hence should be avoided. Since the total transmission through microlens array also depends on the angular profile of the emission source, the light extraction efficiency into the substrate may vary for different organic cavities.

5.3 SEMLA fabrication

A photoresist (PR) layer spun onto a solvent-cleaned soda lime glass (UniversityWafer #3004169267) substrate was patterned with an AutoStep exposure system (GCA AS200) into a hexagonal array of 0.8-μm-diameter circular openings with a 10-μm pitch. After a 10 min hard bake, the glass with patterned PR was immersed for 6.5 min in buffered HF Improved (Transene) diluted 6:1 with a surfactant. The PR was then removed by sonication in acetone and 2-proponal, and a 20-min RCA cleaning step. The NOA-170 was spin-coated onto the etched glass substrate and cured under ultraviolet illumination. NOA-170 filled the etched microlens-shape trenches

and formed a ~20 μm thick flat layer above microlens. After the sub-electrode MLA preparation, a 40 nm thick ITO layer was deposited by radio-frequency magnetron sputtering. The glass and sapphire substrates were cleaned by sonication in tergitol, de-ionized water, acetone, and 2-propanol, and coated with ITO along with SEMLA substrates. Organic layers and top electrodes were deposited by vacuum thermal evaporation in a system with a base pressure of 10^{-7} torr. The green PHOLED consists of a 2 nm thick MoO_3, 40 nm thick 4,4′-cyclohexylidenebis[N, N-bis(4-methylphenyl)benzenamine] (TAPC), 25 nm thick, 8 vol% $Ir(ppy)_2acac$ doped in 4,4′-bis(carbazol-9-yl)biphenyl (CBP) and 65 nm B3PYMPM. The white PHOLED structure consists of a 2 nm thick MoO_3, 50 nm thick TAPC, 15 nm thick 4 vol% $Ir(ppy)_2acac$, 4 vol% bis(2-methyldibenzo[f,h]quinoxaline)(acetylacetonate)iridium(III) ($Ir(MDQ)_2acac$) co-doped in CBP, 10 nm thick bis[2-(4,6-difluorophenyl)pyridinato-C2,N](picolinato)iridium(III) (FIrpic) 10 vol% doped with CBP and 55 nm thick 3,3',5,5'-tetra[(M-pyridyl)-phen-3-yl]biphenyl (BP4MPy). Finally, the cathode consisting of 1.5 nm thick LiQ and 100 nm thick Al was deposited through an array of 1 mm diameter openings in a shadow mask. The refractive indices and thicknesses of materials were measured using a variable-angle spectroscopic ellipsometer (J. A. Woollam, WVASE32). Current-voltage-luminance characteristics were collected using a semiconductor parameter analyzer (HP-4156A) and a calibrated Si photodiode. The electroluminescence spectra were measured using an Ocean Optics miniature spectrometer. The η_{EQE} was calculated using standard methods [9]. The systematic error in the measurement setup is 6%. The external microlens array (Lumlight, MA1303001) was applied at the glass substrate before measurements. To measure the total light intensity in both the air and substrates modes, index-matching fluid was applied between the substrates and the photodiode.

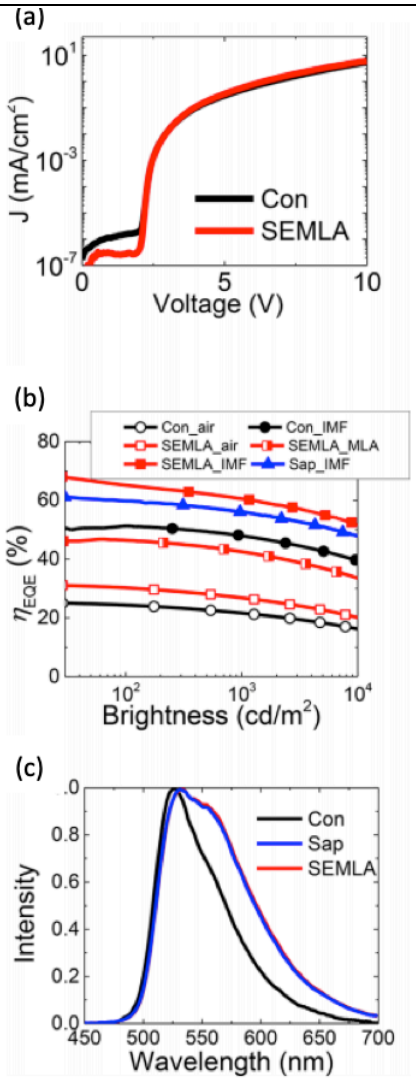

Figure 5.3 Measured characteristics of green phosphorescent organic devices (PHOLEDs) on conventional flat glass (Con), SEMLA and sapphire (Sap) substrates. Measurements with no additional outcoupling at the substrate and air interface (air), with an external microlens array (MLA), and with index matching fluid (IMF) are indicated. (a) Current density (J)-voltage characteristics of the SEMLA and conventional devices showing no significant differences. (b) External quantum efficiencies (η_{EQE}) of PHOLEDs on different substrates. (c) Spectra of green PHOLEDs on different substrates with no additional outcoupling at the substrate/air interface.

5.4 Experimental results

To demonstrate the enhancement in light extraction, green and white PHOLEDs (WOLEDs) were fabricated on conventional glass, sapphire ($n_{sapphire}$= 1.77) and SEMLA

substrates. An external MLA was also attached to SEMLA substrates to further enhance outcoupling. The total quantum efficiency of both air and substrate modes was measured using commercial index matching fluid (IMF) to measure the extraction efficiency of trapped light from the ITO and organic layers. The IMF indices were $n_{IMF,\ low}$= 1.51 for the SEMLA and conventional glass substrates, and $n_{IMF,\ high}$ = 1.70 for sapphire, which enable to outcouple all substrate modes.

The performance characteristics of the green PHOLEDs with different substrates are shown in Fig. 5.3. All devices have identical electrical characteristics since the SEMLA does not intrude into the device active region. The green emitting device comparisons are obtained at a luminance of 100 cd/m^2. The SEMLA alone enhances η_{EQE} from 25±3 % for a PHOLED on a flat glass substrate, to 30±3 %, representing an improvement by an outcoupling enhancement factor of *EF* = 1.2. The outcoupling is further enhanced by *EF* = 1.9 to η_{EQE} = 47±4% using an external MLA to improve substrate outcoupling. Using IMF at the glass-air interface in conjunction with the SEMLA extracts 65±5% (an *EF* = 2.6) of the total generated photons, compared with 51±4 % for conventional glass and 60±4% for sapphire substrates. The most efficient device using the SEMLA reaches η_{EQE} = 70±4%. The spectra of PHOLEDs employing the SEMLA along with sapphire substrates are identical. It is slightly broader than that from conventional glass substrates due to weaker cavity effects in the SEMLA since $n_{SEMLA} \approx n_{sapphire} \approx n_{org}$.

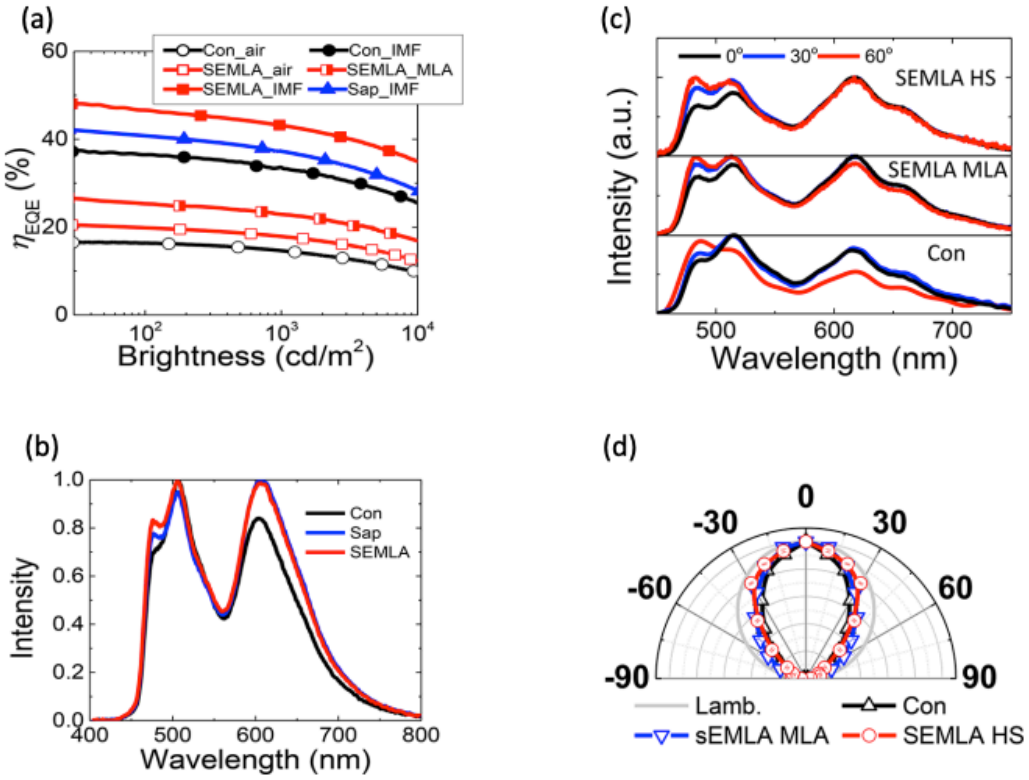

Figure 5.4 Measured characteristics of WOLEDs on conventional glass (Con), SEMLA and sapphire (Sap) substrates. Measurements with no additional outcoupling at the substrate/air interface (air), with an external microlens array (MLA) and with index matching fluid (IMF) are indicated. (a) External quantum efficiency (η_{EQE}) of WOLEDs on different substrates. (b) WOLED spectra on different substrates. The spectra are collected at the same current density (J), at which the luminance of the control L_{Con} = 10,000 cd/m^2. (c) The spectra of devices on a conventional glass substrate (con), a SEMLA substrate with an external MLA (SEMLA MLA) and a SEMLA substrate with a large hemispherical outcoupling lens with IMF (SEMLA HS) at 0°, 30° and 60° to the substrate normal. The spectra were collected at the same J, at which L_{Con} = 5,000 cd/m^2. (d) The angular luminosity distribution of WOLEDs on different substrates. Lamb. Indicates an ideal Lambertian emission pattern.

The optical output characteristics of white PHOLEDs (WOLEDs) are shown in Fig. 5.4. The SEMLA enhances η_{EQE} from 16±2 % for conventional glass substrates to 20±2 % by EF = 1.3. It can be further enhanced to 27±3% using an external MLA with EF = 1.7. Using an IMF, the SEMLA extracts 45±4% (EF = 2.8) of the total generated photons into the glass substrate, compared with 37±3% for conventional glass, and 41±3% for sapphire substrates. The most efficient WOLED using the SEMLA reaches η_{EQE} = 50±3% by EF = 3.1. This is one of the most efficient WOLEDs reported [2–4], limited primarily by the efficiency of the device [5] rather

than the outcoupling scheme. The spectra from the three different substrates without an external MLA are shown in Fig. 5.4b. Both sapphire and SEMLA substrates have high intensities in red and blue spectral regime comparing with the conventional glass, showing boarder spectra resulting from weaker cavity effects.

The WOLED spectra at different viewing angles on a glass, a SEMLA substrate with an external MLA (SEMLA MLA) and a SEMLA substrate with a large hemispherical outcoupling lens (SEMLA HS) are shown in Fig. 5.4c. The spectral blue shift at large angles is only observed for the control device. The SEMLA eliminates this common spectral shift at large angles, making it more suitable for display and white light illumination applications. The angular intensity profile of the conventional device is much narrower than a Lambertian source. In contrast, the SEMLA-modified substrates show higher intensities at large viewing angles, bringing them closer to a Lambertian source.

5.5 Discussion

The simulated light extraction efficiency into the SEMLA (60% in Fig. 5.2b) is lower than measurements (65±5% in Fig. 5.3b), even when assuming 100% transmission (Fig. 5.2c) from the SEMLA into the glass substrate. The mismatch partially results from birefringence [6] (with ordinary and extraordinary indicies of refraction of n_o = 1.8 and n_e = 1.6, respectively) of the electron transporting layer comprising 4,6-bis(3,5-di-3-pyridylphenyl)-2-methylpyrimidine;4,6-bis(3,5-di(pyridin-3-yl)phenyl)-2-methylpyrimidine (B3PYMPM), that is not considered in the simulation. The 10 to 30 μm thickness of the flat spacer layer is comparable with the coherence length of OLEDs [7], but it is nevertheless treated in the simulation as a semi-infinite plane, which may be another source of the differences with measurement.

The SEMLA extracts more light than direct fabrication of the WOLEDs on high index sapphire substrates (Fig. 5.3b and Fig. 5.4a), despite the fact that $n_{sapphire} \approx n_{SEMLA}$ and there is less than 100% transmission from the SEMLA into glass. The lower efficiency of the sapphire substrate results from two sources. First, there is a minor refractive index mismatch between sapphire and the IMF ($n_{sapphire}$= 1.77, $n_{IMF,\ high}$ = 1.70) that reduce the outcoupling of light trapped in the substrate. Second, since the SEMLA thickness is comparable to the WOLED coherence length, the optical power distribution in the SEMLA may be subject to destructive interference. The mismatch between measurement and simulation, and between the devices on sapphire and SEMLA substrates, shows that the SEMLA has reached the theoretical limit for light extraction. This indicates that the SEMLA extracts all emitted optical power with the exception of residual surface plasmon modes. The surface plasmon modes can be further enhanced using a thick ETL, as shown in Fig. 5.2b. Other SPP reduction strategies, such as corrugated structures and optical gratings, may also be integrated with SEMLA, although it would be potentially increase the fabrication complexity and costs.

The similar enhancement factors of light extraction from both the green and white PHOLEDs in Fig. 5.5 indicates that the SEMLA solution is independent of emission wavelength, as expected. The spectra on the SEMLA and sapphire substrates are almost identical since the structure is non-diffractive. This also provides a guideline for cavity designs of OLEDs on SEMLA substrates. Compared with high refractive index substrates, the glass-air interface of the SEMLA substrate can more readily outcouple substrate modes. When employing external MLAs, the outcoupling into air for n_{lens}/n_{out} = 1.5 is higher than for n_{lens}/n_{out} = 1.8 in Fig. 5.2c. Thus, the SEMLA substrates replace sapphire substrates with higher efficiency and lower costs, at no expense to performance or freedom in device design.

An external MLA can enhance the η_{EQE}, but is not as efficient as the large hemispherical lens or the IMF, as shown in Figs. 5.3b and 5.4a. The MLA only outcouples ~ 70% photons from the substrate and air modes combined. Figures 5.3b and 5.5 show that ~20% photons remain trapped in the substrate using the SEMLA in combination with the MLA. Other technologies for substrate mode extraction [8] appear to exhibit the same bottleneck. Solutions to improve extraction from substrate modes are, therefore, necessary to fully exploit the advantages of efficient waveguide and surface plasmon mode outcoupling structures such as the SEMLA.

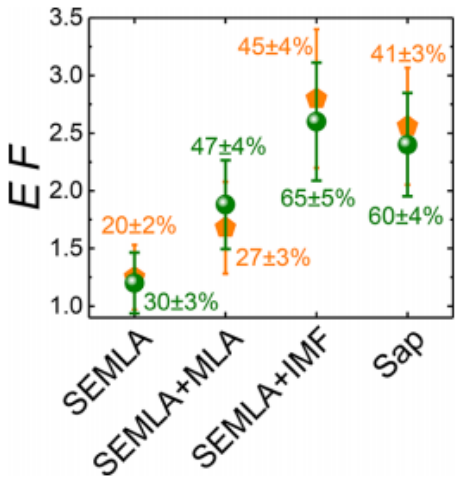

Figure 5.5 The enhancement factor (*EF*) of green and white PHOLEDs on different substrates shown in previous figures, compared with conventional flat substrates with identical OLED device structures. The η_{EQE} are indicated. The green circles and the orange pentagons denote the green and white PHOLEDS, respectively.

5.6 Summary

High refractive index sub-electrode microlens arrays embedded in the glass substrate and beneath the transparent bottom electrode in OLEDs can redirect 100% of the light confined in organic and ITO layers towards the substrate. Its placement below the OLED allows complete freedom in OLED design and fabrication; the non-intrusive flat upper surface of the lens array

provides a surface similar to that of a conventional flat glass or plastic substrate. Both monochromatic and white PHOLEDs fabricated on SEMLA substrates with external outcoupling shows extremely high efficiencies of η_{EQE} = 70±4 % with *EF* = 2.8 for green, and η_{EQE} = 50±3 % with *EF* = 3.1 for the WOLED compared to analogous devices on conventional glass substrates. This is significantly more efficient light extraction than other reports of non-intrusive outcoupling structures. The blue shift eliminated at large angles along with no perceptible impact on image sharpness makes this method ideal for white light illumination and display applications. The spectrum of WOLEDs on SEMLA substrates remains identical with those on sapphire substrates, affording both higher efficiency and lower costs with no expense to performance or freedom in device design.

5.7 Reference

[1] Y. Sun and S. R. Forrest, J. Appl. Phys. **100**, (2006).

[2] T. Komoda, K. Yamae, V. Kittichungchit, H. Tsuji, and N. Ide, SID Symp. Dig. Tech. Pap. **43**, 610 (2012).

[3] Q.-D. Ou, L. Zhou, Y.-Q. Li, S. Shen, J.-D. Chen, C. Li, Q.-K. Wang, S.-T. Lee, and J.-X. Tang, Adv. Funct. Mater. **24**, 7249 (2014).

[4] K. Kato, T. Iwasaki, and T. Tsujimura, J. Photopolym. Sci. Technol. **28**, 335 (2015).

[5] Y.-L. Chang, Y. Song, Z. Wang, M. G. Helander, J. Qiu, L. Chai, Z. Liu, G. D. Scholes, and Z. Lu, Adv. Funct. Mater. **23**, 705 (2013).

[6] M. K. Callens, D. Yokoyama, and K. Neyts, Opt. Express **23**, 21128 (2015).

[7] C.-H. Tsai, K.-C. Tien, M.-C. Chen, K.-M. Chang, M.-S. Lin, H.-C. Cheng, Y.-H. Lin, H.-W. Chang, H.-W. Lin, C.-L. Lin, and C.-C. Wu, Org. Electron. **11**, 439 (2010).

[8] T.-W. Koh, J. A. Spechler, K. M. Lee, C. B. Arnold, and B. P. Rand, ACS Photonics **2**, 1366 (2015).

[9] S. R. Forrest, D. D. C. Bradley, and M. E. Thompson, Adv. Mater. **15**, 1043 (2003).

Chapter 6

Ultrathin, Lightweight and Flexible Organic Light-Emitting Devices with a High Light Outcoupling Efficiency

Flexibility is a key advantage of organic electronics. In particular, flexible light-emitting diodes (OLEDs) are currently employed in mobile devices, with interest now turning to foldable displays [1–7]. Yet only a few reports on flexible OLEDs [3,5,7] address methods of increasing the light extraction efficiency. Most of these outcoupling methods, however, have yet to be adapted for use in flexible OLEDs. In this chapter, we demonstrate ultrathin (10 μm), lightweight (20 g/m^2) and flexible, roughened polychloro-*p*-xylylene (parylene) -based OLEDs with enhanced optical outcoupling.

6.1 Introduction

Parylene forms transparent, conformal, pinhole-free and strain-free sheets with good dielectric and mechanical properties [8] that have recently been utilized as flexible substrates for polymer light-emitting diodes (PLEDs) [9], organic photovoltaics (OPVs) [10,11] and OLEDs [12]. In addition, the parylene has a relatively high refractive index of $n = 1.64$, which is preferred in terms of outcoupling compared to the commonly used flexible polyethylene terephthalate (PET) substrates [3–7] whose refractive index is $n = 1.57$. A visible-wavelength-scale random corrugation imprinted on both surfaces of the parylene sheet, as shown in Fig. 6.1a, scatters light from substrate, waveguide and SPP modes. Corrugated parylene OLEDs increase

the external quantum efficiency at a current density of $J = 0.1$ mA/cm^2 to $\eta_{EQE} = 28 \pm 2\%$, from $\eta_{EQE} = 21 \pm 1\%$ for analogous OLEDs on flat glass substrates, without inducing any changes in electrical characteristics. The thin film OLEDs show a Lambertian intensity profile with identical spectra independent of viewing angle.

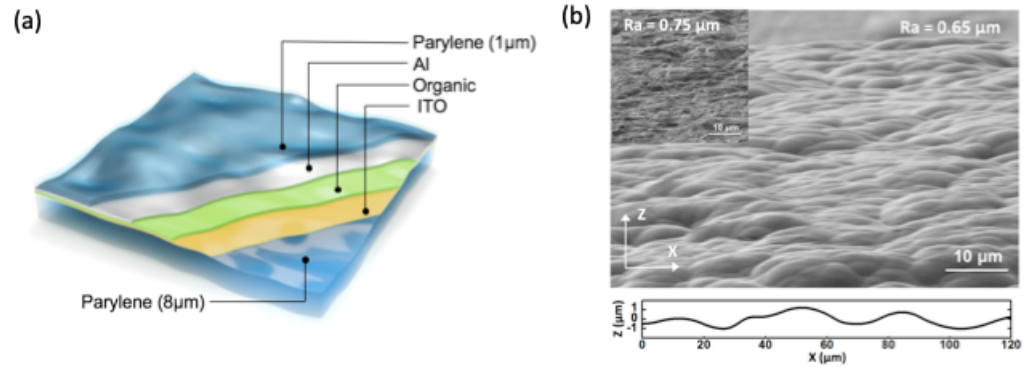

Figure 6.1 (a) Illustration of the corrugated parylene-based OLED (CP-OLED). (b) Scanning electron microscope (SEM) image of the corrugated Al cathode surface of the CP-OLED with an arithmetic mean surface roughness of $R_a = 0.65$ μm. *Inset*, left top: SEM image of the surface of the unpolished sapphire mold with $R_a = 0.75$ μm; bottom: cross-section of the corrugated cathode measured by confocal laser scanning microscopy.

6.2 Device fabrication

The thin film substrate was fabricated by depositing a parylene film on the unpolished side of a sapphire plate. The arithmetic mean roughness of the plate was $R_a = 0.75$ μm, as shown in Fig. 6.1b, inset. A float-zone glass plate was used to produce a flat parylene substrate for comparison. A solution of 2 vol % Micro-90 detergent in deionized water was spin-coated onto the plates at 500 rpm for 30 s to form a release layer. A double-sided adhesive gel film (PF film X4, Gel-Pak) was cut into an open rectangle and placed onto the plate surfaces. This frame is used as a fixture for peeling off and handling the free-standing parylene films. An 8 μm thick parylene film was deposited through physical vapor deposition (PVD) process at a base pressure of 18 mTorr. Parylene-C dimer (dichloro-[2,2]paracyclophane) was sublimed at 180° C and

cleaved in a pyrolysis furnace at 690° C into monomeric form. The monomeric gas was then sent into the deposition chamber where it condenses on the plate surfaces to form a conformal coating at room temperature. A 70 nm thick ITO layer was sputtered onto the parylene surface, followed by thermal evaporation of the organic layers in vacuum at a base pressure of 10^{-7} Torr. The structure of the green bottom-emitting PHOLEDs is: 2 nm MoO_3/40 nm 4,4′-cyclohexylidenebis[N,N-bis(4-methylphenyl)benzenamine] (TAPC)/25 nm bis[2-(2-pyridinyl-N)phenyl-C](acetylacetonato)iridium(III) ($Ir(ppy)_2(acac)$) doped at 8 vol% in 4,4′-bis(carbazol-9-yl)biphenyl (CBP)/65 nm 2,2′,2"-(1,3,5-benzinetriyl)-tris(1-phenyl-1-H-benzimidazole) (TPBi)/1.5 nm 8-quinolinolato lithium (Liq)/100 nm Al. The devices were patterned using a shadow mask comprising an array of 1 mm wide strips, resulting in a crossbar pattern between the bottom ITO and top Al contacts. The devices were encapsulated by depositing a 1 μm thick parylene film over their surfaces. The parylene thickness is calibrated using a profilometer (Dektak XT). The optical constants and thicknesses of other materials were measured using variable-angle spectroscopic ellipsometry. Finally, the flexible OLEDs were peeled off from the plates using the gel frames. Unpeeled samples were also prepared.

The current density-voltage-luminance (*J-V-L*) characteristics of the devices were collected using a semiconductor parameter analyzer (HP-4156A) and a calibrated Si photodiode (Hamamastu, S3584-08). The electroluminescence (EL) spectra were measured using a spectrometer (USB4000, Ocean Optics, Inc). The η_{EQE} was calculated using standard methods [13]. Index-matching fluid (IMF) with an index of refraction of $n_{IMF,high}$ = 1.70 was applied between the sapphire substrate (unpeeled sample) and the Si photodiode to detect all air and substrate modes. An IMF with $n_{IMF,low}$ = 1.51 was used for the device on glass.

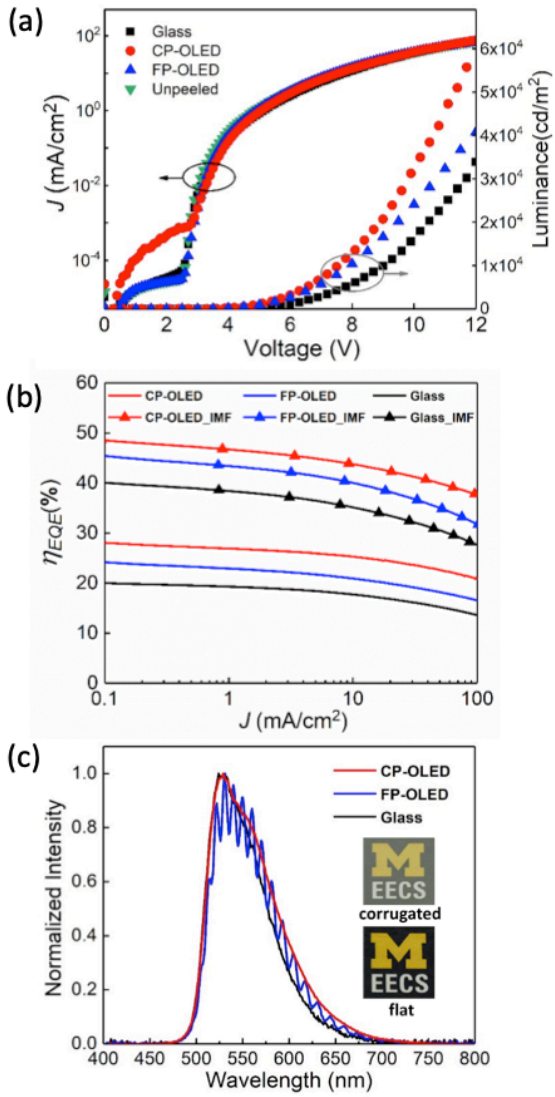

Figure 6.2 Device characteristics. (a) Current density-voltage-luminance (*J-V-L*) characteristics of the CP/FP-OLEDs, unpeeled and glass devices. (b) External quantum efficiencies (η_{EQE}) of the CP-OLED, FP-OLED, glass and unpeeled devices. The η_{EQE} of the unpeeled CP-OLED, FP-OLED and glass device (triangles) are measured using index-matching fluid (IMF) between the substrate (sapphire for unpeeled CP/FP-OLEDs) and the photodiode to outcouple all substrate modes. (c) Electroluminescence spectra of the devices. *Inset*: Photographs comparing the transparency of the corrugated (upper) and flat (lower) parylene substrates on a printed image.

A scanning electron microscope (SEM) image of the Al cathode of the CP-OLED is shown in Fig. 6.1b. The random corrugated pattern originates from the rough surface of the unpolished sapphire substrate that transfers to the conformably deposited parylene film and OLED layers. The transferred corrugation at the CP-OLED cathode has a surface roughness of R_a = 0.65 μm, with peak-to-valley depth of 2 μm. The relatively spiky features on the unpolished

sapphire mold are replaced by a smoothly corrugated profile of the CP-OLED due to the conformal nature of the parylene PVD process.

6.3 Experimental results and discussion

Figure 6.2a shows the *J-V-L* characteristics of the CP/FP (flat parylene)-OLEDs and devices on glass substrates. The CP/FP-OLEDs demonstrate identical *J-V* characteristics compared with both unpeeled and glass substrate devices. The FP-OLED has $\eta_{EQE} = 24 \pm 2\%$ at $J = 0.1$ mA/cm^2, compared to $\eta_{EQE} = 21 \pm 1\%$ for the device on the glass substrate. In the CP-OLED, $\eta_{EQE} = 28 \pm 2\%$ (see Fig. 6.2b). The corrugated features of the device have no impact on the electrical properties of the OLED itself since the micron-scale smoothness of the corrugations do not significantly affect the uniformity of the nanometer-scale thicknesses of the OLED active layers.

To understand the source of improvement of the CP-OLED outcoupling from waveguide and SPP modes, we measure all the optical power in the substrate modes using IMF, with results compared in Fig. 6.2b (triangles). We assume unity transmission at the parylene/sapphire interface. The unpeeled CP-OLED yields $\eta_{EQE} = 49 \pm 3\%$, and the unpeeled FP-OLED yields $\eta_{EQE} = 46 \pm 3$ %. Also, $\eta_{EQE} = 41 \pm 3$ % is obtained for the device on the glass substrate. By subtracting the efficiencies of the glass substrate devices, the enhancement in the extracted waveguide or SPP modes is $\Delta\eta_{CP\text{-}OLED} = 8 \pm 6\%$ for the CP-OLED, and $\Delta\eta_{FP\text{-}OLED} = 5 \pm 6\%$ for the FP-OLED.

The electroluminescence (EL) spectra of the devices are shown in the Fig. 6.2c. All have spectral peaks at $\lambda \approx 530$ nm. The EL spectrum of the FP-OLED shows small oscillations with a period $\Delta\lambda \approx 10$ nm due to interference from the opposite surfaces of the flat, 8 μm thick parylene

substrate. This oscillation does not exist for the CP-OLED due to randomization of the optical field by the corrugations. The spectra of parylene-based devices are slightly broader than that from conventional glass substrates due to weaker cavity effects, since the refractive index difference between parylene and the organic layers is small [15]. Photographs of a corrugated (upper) and a flat (lower) parylene substrate on a printed image are shown in Fig. 6.2c, inset. The flat parylene substrate is transparent while the corrugated one appears hazy due to the random scattering from its roughened surface. Haziness can prevent the CP-OLED from use in displays. The angular emission characteristics for the CP-OLED are shown in Fig. 6.3. Compared to glass-based device, the CP-OLED shows a Lambertian intensity profile. Similarly, the spectral shapes are independent of viewing angle to at least 60^{o} from the substrate normal. To evaluate the flexibility of the CP-OLED, the performance of the devices was tested before and after bending. The diodes become either leaky or resistive after repeated bending, which is possibly due to cracking of the brittle ITO anode [11]. Alternative flexible electrodes are required for flexible devices.

The optical power distributions within the glass and parylene OLEDs were calculated using Green's function analysis assuming that a dipole emitting at a wavelength of 540 nm is located in the center of the 25 nm thick emissive layer with n = 1.83. $Ir(ppy)_2acac$ dipole alignment leads to 77% normal and 23% horizontal component emission (relative to the substrate plane) [14]. The thicknesses and refractive indices of each layer are: ITO, 70 nm thick, n = 2.1, hole transport layer, 40 nm thick, n = 1.70, electron transport layer, 65 nm thick, n =1.78, and Al cathode, $n = 0.6 + 2.8i$. The parylene substrate index is n = 1.64.

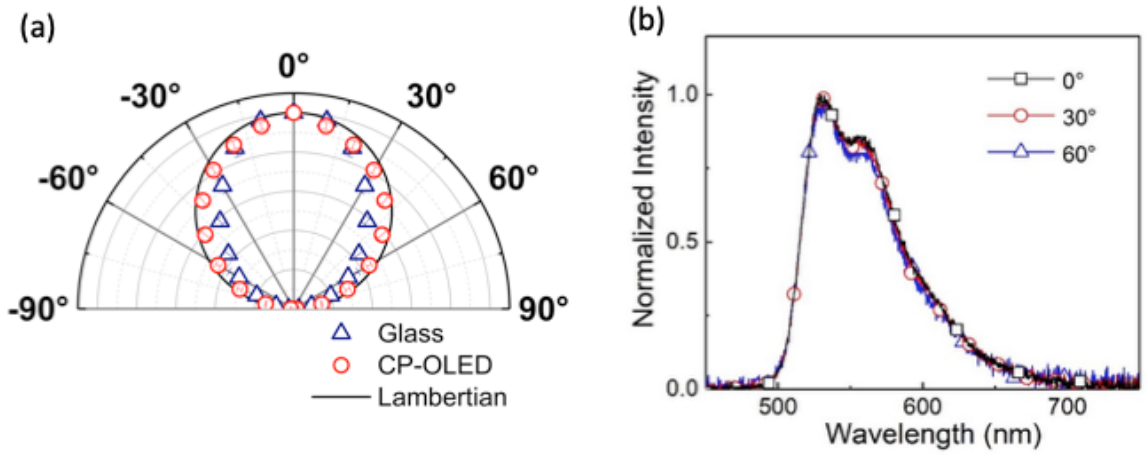

Figure 6.3 Device angular optical characteristics. (a) Angular dependence of light intensity of the CP-OLED and glass-based device. All data are normalized to the intensity in the substrate normal direction. The Lambertian emission pattern is plotted as reference. (b) Electroluminescence spectra of the CP-OLED at viewing-angles of 0°, 30° and 60° to the substrate normal.

The imprinted corrugated pattern of the CP-OLED randomizes the emitted light trajectories, allowing more of the trapped photons to find the escape cone at all interfaces. The result of this randomization is a Lambertian profile and wavelength-independent emission characteristics. In particular, the corrugated pattern with a visible-wavelength-scale surface roughness of R_a = 0.65 μm effectively enhances the outcoupling of photons within the visible spectrum. Correspondingly, as shown in the inset of Fig. 6.1b, the surface profile of the CP-OLED has an approximately 20 μm lateral distance from peak to valley. This structure ensures that the waveguide modes can be effectively scattered out before absorption. This lateral distance also ensure no potential shortening path introduced in the OLED active region, which is the reason for identical electrical characteristic of all devices, as shown in Fig. 6.3. Therefore, this corrugation without sharpness does not intrude inside the active region, but ripples the whole active region along the surface of parylene substrates. The outcoupling efficiencies of CP-OLEDs can be further optimized by using surface molds with optimized roughness, such as

sandblasted glass. Compared to other outcoupling schemes implemented in PET-based flexible OLEDs, such as adopting a high-index electrode [3] or introducing gratings/corrugations using nanoimprint lithography, [5,7] requiring complicated fabrication processes, our method is simpler and has a potentially lower cost.

6.4 Summary

We demonstrated ultrathin, lightweight and flexible parylene substrates as a simple and potentially low-cost platform for high-efficiency flexible OLEDs. Outcoupling enhancement without any electrical characteristic change is achieved by visible-wavelength-scale corrugations imprinted on the ultrathin high-index parylene substrate. Flexible green PHOLEDs fabricated on corrugated parylene substrates with η_{EQE} = 28 ± 2% were demonstrated with a Lambertian intensity profile and wavelength-independent emission characteristics. Since the extreme substrate thinness can make handling difficult, in many applications the flexible parylene-based OLEDs can be laminated onto a variety of curved or flat surfaces whose materials choice is unconstrained by device processing conditions. Alternatively, beyond the obvious applications to foldable displays, the thin substrates may serve in medical applications, wearable electronics, or electronic paper where the extreme flexibility is beneficial. [10] Finally, the devices may be compatible with roll-to-roll manufacturing processes, paving the way for widespread and low-cost use of flexible OLEDs in emerging display and lighting applications.

6.5 Reference

[1] S. R. Forrest, Nature **428**, 911 (2004).

[2] G. Gu, P. E. Burrows, S. Venkatesh, S. R. Forrest, and M. E. Thompson, Opt. Lett. **22**, 172 (1997).

[3] Z. B. Wang, M. G. Helander, J. Qiu, D. P. Puzzo, M. T. Greiner, Z. M. Hudson, S. Wang, Z. W. Liu, and Z. H. Lu, Nat. Photonics **5**, 753 (2011).

[4] T.-H. Han, Y. Lee, M.-R. Choi, S.-H. Woo, S.-H. Bae, B. H. Hong, J.-H. Ahn, and T.-W. Lee, Nat. Photonics **6**, 105 (2012).

[5] L. H. Xu, Q. D. Ou, Y. Q. Li, Y. B. Zhang, X. D. Zhao, H. Y. Xiang, J. De Chen, L. Zhou, S. T. Lee, and J. X. Tang, ACS Nano **10**, 1625 (2016).

[6] L. Zhou, H.-Y. Xiang, S. Shen, Y.-Q. Li, J.-D. Chen, H.-J. Xie, I. A. Goldthorpe, L.-S. Chen, S.-T. Lee, and J.-X. Tang, ACS Nano **8**, 12796 (2014).

[7] R. Wang, L. H. Xu, Y. Q. Li, L. Zhou, C. Li, Q. D. Ou, J. De Chen, S. Shen, and J. X. Tang, Adv. Opt. Mater. **3**, 203 (2015).

[8] M. J. Bak, M. Salcman, and E. M. Schmidt, 121 (1977).

[9] T. Yokota, P. Zalar, M. Kaltenbrunner, H. Jinno, N. Matsuhisa, H. Kitanosako, Y. Tachibana, W. Yukita, M. Koizumi, and T. Someya, 1 (2016).

[10] S. Park, S. W. Heo, W. Lee, D. Inoue, Z. Jiang, K. Yu, H. Jinno, D. Hashizume, M. Sekino, T. Yokota, K. Fukuda, K. Tajima, and T. Someya, Nature **561**, 516 (2018).

[11] J. Jean, A. Wang, and V. Bulović, Org. Electron. Physics, Mater. Appl. **31**, 120 (2016).

[12] J.-H. Lee and A. Kim, Org. Electron. **47**, 147 (2017).

[13] S. R. Forrest, D. D. C. Bradley, and M. E. Thompson, Adv. Mater. **15**, 1043 (2003).

[14] M. J. Jurow, C. Mayr, T. D. Schmidt, T. Lampe, P. I. Djurovich, W. Brutting, and M. E. Thompson, Nat Mater **15**, 85 (2016).

[15] Y. Qu, J. Kim, C. Coburn, and S. R. Forrest, ACS Photonics **5**, 2453 (2018).

Part II Exciton Photon Strong-Coupling

Chapter 7
Exciton-polaritons

In Part I, we focused on emission from excitons in weak optical cavities. The interaction between the excitons and photons is in a perturbative regime and can be predicted using Fermi's golden rule. [1] In this limit of weak coupling, excitons emit photons that propagate away without further interaction with the excitons. The energy transfer is one directional. In this regime, the spontaneous emission rate and the emission power pattern of an exciton can be modified by changing the photonic density of states. In OLEDs, this changes the exciton lifetime and the light-extraction efficiency of devices.

When lifetimes of excitons and photons are both longer than the interaction time, there is a coherent energy exchange between the excitons and photons at a characteristic frequency Ω, called the Rabi frequency. The energies of the new system are no longer same as the energies of uncoupled excitons or photons. We attribute this to strong interaction of excitons and photons. In the regime of strong light-matter interaction, one can no longer treat the excitons and photons separately. We must consider the new modes of the system that are in the form of a mixture of these two particles. This new eigenstate is called exciton-polariton or cavity-polariton. The emergence of this new quasi-particle requires slow damping of both excitons and photons and a large exciton-photon coupling strength, *i.e*. a combination of a confined optical mode and large exciton oscillator strength. Exciton-polaritons have the properties of both photons and excitons.

They usually have a light effective mass due to their cavity photonic components, and strong interaction with matter-like particles inherited from excitons.

7.1 Theory for strong coupling

Exciton-polaritons can be explained and modeled by classical, semi-classical and fully quantum mechanical pictures [2]. These three conceptual frameworks are discussed and compared in depth by Torma and Barnes [3] using the case of coupling between emitters and surface plasmon polaritons. Here, we use the classical model and the quantum picture to review the basic concepts of exciton-polaritons.

7.1.1 Coupled oscillator model

An intuitive and widely applied model to understand the eigen-energies of this system is to treat excitons and photons as coupled harmonic oscillators, which is called the coupled oscillator model. In this model, the coupled-system Hamiltonian can be expressed as

$$\begin{pmatrix} E_{ph} & V \\ V & E_{ex} \end{pmatrix} \begin{pmatrix} \alpha \\ \beta \end{pmatrix} = E \begin{pmatrix} E_{ph} & V \\ V & E_{ex} \end{pmatrix} \tag{7.1}$$

where α and β are the Hopfield coefficients representing the composition of the eigenstate in terms of photons and excitons, V is the interaction coefficient, E_{ph} and E_{ex} are the energies of uncoupled photons and excitons that can be expressed as functions of angle. In organic semiconductors, the exciton energy is approximately dispersionless.

7.1.2 Classical model

An optical wave travelling in a material whose macroscopic electric susceptibility can be expressed using the Lorentz oscillator model:

$$\chi(\omega) = \frac{Ne^2}{m} \frac{1}{\omega_{ex}^2 - \omega^2 - i\gamma\omega} \tag{7.2}$$

where χ is the susceptibility, N the density of dipoles with charge e and mass m. ω_{ex} is the resonant frequency of the harmonic oscillator and γ is the macroscopic damping. The permittivity ε is related to the susceptibility through:

$$\varepsilon(\omega) = \varepsilon_b(\omega) + \chi(\omega) \tag{7.3}$$

where ε_b is the background dielectric constant that accounts for all non-resonant transitions. An electromagnetic wave travels through this material with the dispersion:

$$k^2 = \frac{\omega^2}{c^2}\,\varepsilon(\omega). \tag{7.4}$$

The dispersion of light differs according to the optical structure. The dispersion of the uncoupled optical wave can be expressed as

$$k^2 = \frac{{\omega_{ph}}^2}{c^2}\,\varepsilon_b. \tag{7.5}$$

Near the resonance of the excitons ($\omega_{ex} \approx \omega$), we arrive at a quadratic expression:

$$(\omega - \omega_{ph})(\omega - \omega_{ex} + \frac{i\gamma}{2}) = \frac{Ne^2}{2\varepsilon_b m} \equiv V^2. \tag{7.6}$$

We then arrive at the eigen-energies of the system:

$$\omega_{\pm} = \frac{\omega_{ph} + \omega_{ex}}{2} \pm \frac{1}{2}\sqrt{4V^2 + (\omega_{ph} - \omega_{ex})^2}\,. \tag{7.7}$$

Here we neglect the damping of photons and excitons. We can define detuning as the energy difference between excitons and photons, $\Delta = \hbar(\omega_{ph}\text{-}\omega_{ex})$. When $\omega_{ph} = \omega_{ex}$, the energy difference between the two modes is the Rabi splitting energy, given by

$$\hbar\Omega = \hbar\sqrt{4V^2 - (\gamma_{ex} - \gamma_{ph})^2} \tag{7.8}$$

and Ω is Rabi frequency. γ denotes damping.

In the classical picture, the Rabi splitting is proportional to the numbers of coupled dipoles, and does not depending on the optical field intensity. This classical picture can predict the dispersion relations of the quantum quasi-particles. Therefore, the transfer matrix method is widely applied to design polariton microcavities.

7.1.3 Quantum picture

In the full quantum picture, we consider a single quantum emitter interacting with the field. Haug and Koch [4] showed the exciton-polariton Hamiltonian can be expressed as :

$$H = H_{ex} + H_p + H_{int} = E_{ex}\hat{a}^+\hat{a}^- + E_{ph}\hat{b}^+\hat{b}^- - ig(\hat{a}^+ + \hat{a}^-)\left(\hat{b}^+ + \hat{b}^-\right) \quad (7.9)$$

where the E_{ex} and E_{ph} are the energies of uncoupled excitons and photons. $\hat{a}^+, \hat{a}^-, \hat{b}^+, \hat{b}^-$ are the creation and annihilation operators for excitons and photons, respectively. The excitons-photon coupling constant is g. We can simplify the interaction Hamiltonian as Eq. 7.9 using rotating wave approximation, in which we neglect the term containing the frequency of ($\omega_{ex} + \omega_{ph}$), a much higher frequency than other frequencies characterizing the dynamics. However, this approximation may fail if the Rabi splitting is too large, and comparable with the frequency of ($\omega_{ex} + \omega_{ph}$). We call it ultra-strong coupling regime if the coupling strength reaches this level, which is the main topic in Chapter 9.

$$H_{int} = -ig(\hat{a}^+\hat{b}^- + \hat{a}^-\hat{b}^+). \quad (7.10)$$

The eigen-energies of the new system then becomes:

$$E_{\pm} = \frac{1}{2}(E_{ex} + E_{ph}) \pm \frac{1}{2}\sqrt{\Delta^2 + 4g} \quad (7.11)$$

where Δ has the same definition as the classical model. The quantum picture Eq. 7.11 gives the same eigen-energies of the new system as the classical picture Eq. 7.16. The two energy levels

are called lower and upper polariton branches. Figure 7.1 shows a characteristic anticrossing of the two polariton branches split from the uncoupled excitons and photons.

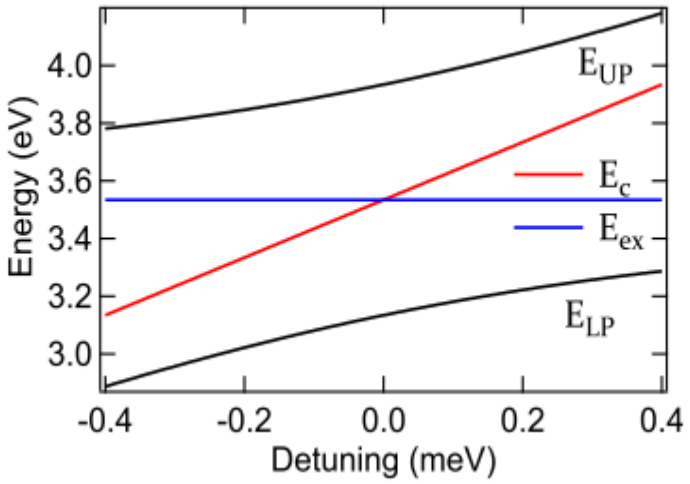

Figure 7.1 The calculated anticrossing of the lower and upper polariton energy levels while tuning the photon and excitons energies.

The uncoupled excitons and photon operators can be diagonalized with the Hopfield transformation by introducing the polariton creation and annihilation operator $\hat{p}^{\pm}$:

$$\hat{p}^{\pm} = \alpha\hat{b}^{\pm} \mp \beta\hat{a}^{\pm} \tag{7.12}$$

where α and β are the Hopfield coefficients, as in Eq. 1.10. Then, the Hamiltonian becomes:

$$H = E_p\hat{p}^{+}\hat{p}^{-}. \tag{7.13}$$

In this quantum picture, the mixed excitonic and photonic nature of polaritons is highlighted. Equation 7.13 shows the polariton is the exchange of excitation between an exciton with an empty cavity and a ground state exciton with the cavity populated with a photon. This energy exchange occurs at the Rabi frequency. The periodic absorption and emission continues until the excitation escapes from the cavity or is dissipated into heat. This picture also shows the polariton can be more exciton-like or photon-like according to the Hopfield coefficients.

7.2 Exciton-polaritons in a cavity

In the previous section, we reviewed the general theory for exciton-polaritons without specific dispersions of excitons and photons. In this thesis, we are only dealing with Frenkel excitons in amorphous organic films, which are nearly dispersionless. The photon dispersion depends on the optical structure. Here, we apply two types of photonic modes both supported by a distributed Bragg reflector (DBR). For polariton lasing, we use a planar cavity with two DBRs. For polariton transport, we use a Bloch surface waves supported at the DBR-air interface. In this section, we review basic properties of photons and resulting polaritons in a planar cavity with DBRs.

7.2.1 Planar cavity photons

A planar microcavity consists of two mirrors separated by a distance L_c. The mirrors can either be metallic films or DBRs. The optical power penetrates less into the metal mirrors compared with the DBR, resulting in stronger exciton-photon interactions. However, due to the high absorption of metals, DBR is usually chosen for polariton lasers. A DBR compresses stacks of alternating low- and high-index layers with an optical length equal to a quarter of the target wavelength. The high reflectivity of DBRs results from constructive interference from reflections at each interface. Therefore, more pairs of alternative layers and higher index contrast between low- and high-index layers lead to higher reflectivity. This reflectivity covers a broad range of wavelengths centered at the target wavelength, which is referred to as the stopband, as shown in Fig. 7.2. The bandwidth depends on the index contrast of the layers. The reflectivity can be expressed as:

$$R = 1 - \frac{4n_{ext}}{n_{in}}\left(\frac{n_l}{n_h}\right)^{2N} \tag{7.12}$$

where n_{in} and n_{ext} are the indices of the incident and exit materials, respectively, n_l and n_h are the indices of low- and high-index layers in the DBR, and N is the stack numbers of the DBR.

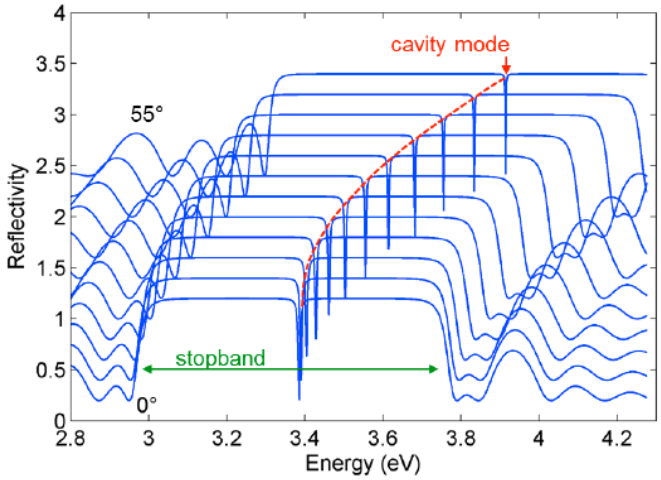

Figure 7.2 The calculated TE reflectivity of a cavity consisting of two DBRs for different incident angles. The DBRs consist of 8.5 pairs of SiO_2 and SiN_x sandwiching a 230 nm SiO_2 layer.

Since the optical field penetrates into the DBR, the equivalent cavity length L_{eff} is larger than L_c. Therefore, we use $L_{DBR} = L_{eff} - L_c$ to denote the penetration depth of the optical field into the mirror, which depends on both the wavelength and polarization. For wavelengths near the center of the stopband, the angle-dependent reflectivity can be expressed as: [5]

$$r_{DBR}(\omega) = \sqrt{R}\, exp\, [\frac{in_c}{c}(\omega - \omega_0)]L_{DBR}cos\theta_c \tag{7.13}$$

where ω_0 is the stop band center frequency, θ_c is the incidence angle in the material between the two mirrors with an index of n_c.

In a planar cavity, the resonance occurs when there is constructive interference after the an optical wave traveling one round trip. In a cavity with two ideal mirrors, the resonance is directly related to the optical distance between the mirrors:

$$\omega'_{ph} = m\pi c\, / L_c n_c cos\theta\, , \tag{7.14}$$

where *m* is an integer. In a cavity with two DBR mirrors, due to the penetration into the DBR the resonant frequency can be expressed as:

$$\omega_{ph}(\theta) = \frac{L_c \omega'_{ph}(\theta) + L_{DBR}\omega_0(\theta)}{L_c + L_{DBR}} \tag{7.15}$$

$$E_{ph}(k) = \frac{\hbar c}{n_C} k = \frac{\hbar c}{n_C} \sqrt{k_\parallel{}^2 + k_\perp{}^2} = \frac{\hbar c}{n_C} \left[\left(\frac{\pi}{L_{eff}}\right)^2 + k_\parallel{}^2\right]^{\frac{1}{2}} \tag{7.16}$$

where $k_\parallel$ and $k_\perp$ are the horizontal and vertical components of the wavevector. Since $k_\parallel$ can also be expressed as

$$k_\parallel = k sin(\theta) = \frac{E_{ph}(k)}{\hbar c} sin(\theta). \tag{7.17}$$

Eq. 7.16 can be rewritten as: [6]

$$E_{ph}(\theta) = E_{ph}(\theta = 0)\left(1 - \frac{sin^2(\theta)}{n_{eff}^2}\right)^{-\frac{1}{2}} \tag{7.18}$$

where n_{eff} is the effective refractive index that accounts for the optical penetration into the mirrors and different dielectric constants of layers across the cavity. This equation can map a dispersion of the cavity photons, which can be measured using angle-resolved reflectivity, as calculated in Fig. 7.2 and schematically presented in Fig. 7.3.

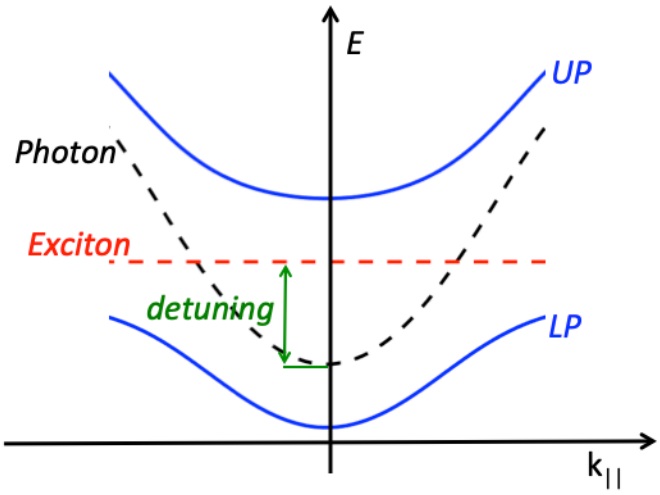

Figure 7.3 Dispersion relations of upper and lower branches of polaritons (UP and LP), and uncoupled excitons and photons in a planar cavity with DBRs. At substrate normal direction, the energy difference between excitons and photons is referred to detuning.

7.2.2 Exciton-polaritons in the planar cavity

Figure 7.3 shows dispersion relations of the uncoupled excitons and photons, and the upper and lower branches of polaritons, which are referred to as UP and LP, respectively. At the substrate normal direction, the energy difference between the uncoupled excitons and photons is called detuning in a cavity polaritonic system. When the exciton and photon energies are the same, the energy difference between LP and UP is called the Rabi splitting energy.

The polariton dispersions can be measured using angle-resolved reflectivity of the cavity. In organic semiconductors, the absorption instead of emission energy determines the exciton energy. Due to the large Stokes shift of organic materials, UP is not emitting in most cases and hence angle-resolve photoluminescence can only measure the dispersion of the LP. During photoluminescence measurements, the cavity is usually optically pumped. If the incident pumping light is chosen to coincide with a point on the polaritons dispersion curve, the polaritons are directly excited. This pumping method is called resonant pumping. Otherwise, the

uncoupled excitons are generated first, referred to as the exciton reservoir; or polaritons are generated with phonon emission. This pumping method is called non-resonant pumping.

7.3 Previous work on organic exciton-polaritons

7.3.1 Organic polariton lasers

Polaritons can interact with solid-state particles due to their excitonic nature. As the pumping power increases, the polariton density goes up to a point that polariton-polariton and polariton-exciton collisions become significant. These elastic interactions can lead to nonlinear behaviors. When the cavity is under non-resonant pumping, the exciton reservoir relaxes into large-wavevector polariton states through phonon scattering. If the subsequent relaxation paths are fast, as pumping power increases, the population build-up at the bottom of the LP curve leads to coherent lasing-like emission. This phenomenon is called polariton lasing and was first observed in a GaAs-based cavity by Deng *et al*. [7,8] The coherence of the polariton laser results from the spontaneous emission from a macroscopic coherent state. Therefore, the polariton lasing does not require population inversion as in conventional lasers. Deng *et al*. observed that two thresholds co-exist in the same polariton device: the conventional lasing threshold produced from an inverted electron-hole population is one order of magnitude higher than the polariton lasing. Since then, varieties of active materials have been used to achieve polariton lasing. Most inorganic microcavities require cryogenic temperatures to observe cavity-polaritons due to the small binding energy of Wannier-Mott excitons. Recently, microcavities with large-bandgap inorganic semiconductors, such as ZnO [9,10] and GaN [11,12], have been observed to support room-temperature polariton lasing. On the other hand, Frenkel excitons in organic

semiconductors possess binding energies of 0.1-1 eV, leading to cavity-polaritons that are highly stable at room temperature.

Since the first demonstration of an organic polariton laser using single crystal anthracene [13] around a decade ago, many organic materials with different morphologies exhibited the same phenomenon. [14–18] The materials and lasing thresholds at room temperature of these works are listed in Fig. 7.4 and Table. 7.1. The lasing threshold depends on many factors other than active organic materials, such as detuning, cavity quality, pumping energy and pumping angle. [19] Therefore, the polariton lasing thresholds listed above cannot show the whole picture of the optical properties of these materials.

Efficient relaxation of cavity-polaritons into the bottom of the lower branch of the polariton dispersion relationship is crucial to reduce the polariton lasing threshold. For inorganic semiconductors, relaxation relies on exciton-polariton and polariton-polariton interactions, which are much weaker for Frenkel excitons in organic semiconductors. The radiative pumping directly from the exciton reservoir and phonon emission play more important roles in organic microcavities.

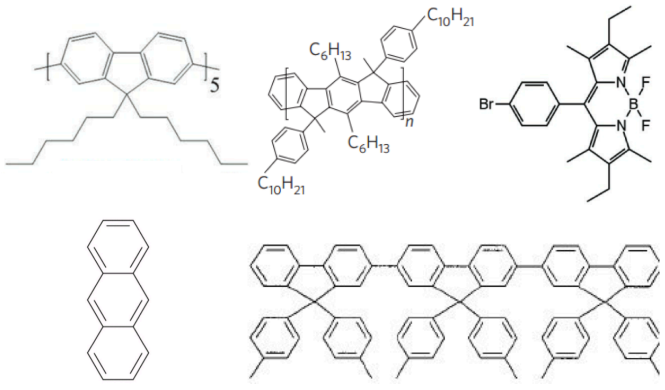

Figure 7.4 The active organic materials in organic polariton lasers. From top left, they are pantaflourene, MeLPPP, BODIFPY-Br, anthracene and TDAF.

Table 7.1 The active organic materials and their polariton lasing thresholds

Materials	Polariton lasing threshold
Anthracene	2×10^6 kW/cm^2
TDAF	1×10^5 kW/cm^2
MeLPPP	6×10^4 kW/cm^2
eGFP	3×10^3 kW/cm^2
BODIPY-Br	2×10^5 kW/cm^2
Pantaflourene	5×10^4 kW/cm^2

The first demonstration of organic polariton lasing used single crystal anthracene. Different from other systems, it does not demonstrate characteristic pumping power dependent blueshifts that results from bi-excitonic interactions. The relaxation mechanism possibly follows the same pathway as stimulated emission in bare anthracene films. [20] The lack of bi-excitonic interaction may be one of the reasons leading to the highest polariton lasing thresholds listed in Table 7.1. Slootsky *et al*. [21] demonstrated the polariton lasing threshold in the same system can be one order of magnitude lower at cryogenic temperatures.

In 2014, polariton lasing with nonlinear interactions were demonstrated [16,18] in two different organic systems: one using an amorphous vacuum thermal deposited neat TDAF film and one using a spin-coated MeLPPP polymer layer. Both showed a characteristics power-dependent blueshift that results form polariton-polariton or exciton-polariton interactions. Later, TDAF also demonstrated room temperature superfluidity under resonant pumping. [22] Since then a series of phenomena have been studied using this organic material, such as OLEDs in the

ultrastrong coupling regime, and dynamical instability in non-equilibrium polariton condensation. [22–27]

Dietrich *et al*. [14] used biologically produced enhanced green fluorescent protein (eGFP) realizing both polaritonic and photonic lasing. Similar to inorganic polariton cavities, it shows the co-existence of polariton and photonic lasing in the same cavity, with a polariton lasing threshold one order of magnitude lower than photonic lasing. This is the only organic system showing the transition from polariton lasing to photonic lasing. Since the fluorophore in eGFP is surrounded by a biologically produced structure called a 11-β sheet, excitons on the active molecules are prevented from concentration quenching, which significantly reduces exciton-exciton annihilation and lowers the threshold. It is the only demonstration of polariton lasing under nanosecond pumping pulses, while other organic systems require picosecond or sub-picosecond pumping pulses.

The first non-blue polariton lasing was demonstrated by Cookson *et al*. [17] using a yellow dye, bromine-substituted boron-dipyrromethene (BODIPY-Br), diluted in a polystyrene matrix as the active material. In 2019, another BODIPY derivative showed polariton lasing in a broad detuning range, as shown in Fig. 7.5. Using the same active material with different photon energies, the polariton lasing can be realized at emission wavelengths from 540 nm to 570 nm. Since the polariton lasing threshold dependence on detuning is not yet clear, it provides a good organic material to study related topics.

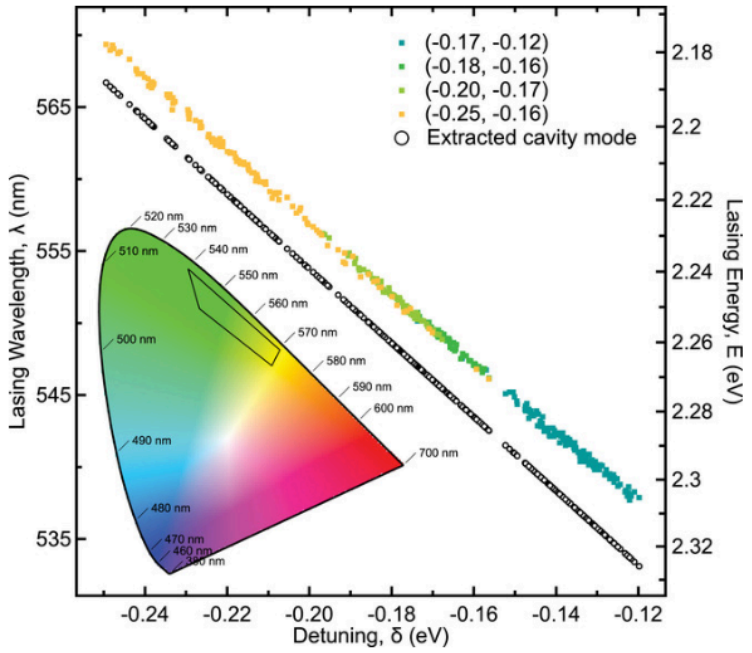

Figure 7.5 Cookson et al demonstrated polariton lasing using a microcavity containing BODIPY-G1. This system can undergo lasing in a broad wavelength range from 540 nm to 570 nm.

7.3.2 Exciton-polariton long-range transport in organic systems

In a molecular system, the excitation energy is localized by Frenkel excitons, and their transport is dominated by near-field Förster or Dexter intermolecular hopping. However, intrinsic static and dynamic disorder typically lead to exciton diffusion lengths less than 10 nm and a diffusion constant of only ~10^{-3} cm^2/s. Precise tailoring of molecular structure and ordered assemblies favorable to exciton transport has been proven to be difficult; only a few successes have been achieved to demonstrate exciton transport over only a few microns. [28–30]

Polaritons partially inherit their light effective mass and delocalization properties due to their photonic component, and thus are potentially immune from interactions with local defects and disorder common to molecular solids, even at room temperature. [31–33] It has been proposed that exciton conductance is significantly enhanced via strong coupling with a photon. [34–38] Moreover, coherent coupling with an extended and propagating photon mode

can lead to rapid and long-range transport that differs from the slow and short-range diffusion of more massive excitons. [39–41]

Lerario *et al*. demonstrated an interactive polariton fluid by coupling Bloch surface waves at the DBR surface with excitons in a parylene derivative, Lumogen Red F305 vacuum deposited film. The coupling strength between Bloch surface waves and excitons is well studied, [42–44] and this surface polariton transport has been demonstrated in several material systems. [35,45] The Bloch surface wave is an ideal type of photon to study polariton transport for the following reasons. First of all, the Bloch surface wave is tightly confined at the DBR-air interface, resulting in a small mode volume which results in large coupling strength between excitons and photons. Secondly, the optical structure consists only of dielectric materials with very low or even negligible absorption, leaving the polariton lifetime limited only to scattering by defects or the intrinsic decay rate of polaritons. Lastly, Bloch surface waves have a high group velocity, making the polariton group velocity on the same order of magnitude of the speed of light and hence a long propagation length is expected. One defect is due to optical index changes to which polaritons are highly sensitive. The sharpness of the polaritonic mode spectrum in the work of Lerario *et al*. implies high local homogeneity of their organic film. Due to the low loss of the all-dielectric system and high uniformity of the film, the polariton propagation is as long as 300 μm. They also demonstrated the propagation length dependence on photonic fraction of polaritons, as shown in Fig. 7.6. More photonic fraction reads to longer the polariton propagation. They also found the nonlinear interaction within the polaritons fluid. As the pumping power increases, a blueshift of polaritons appears.

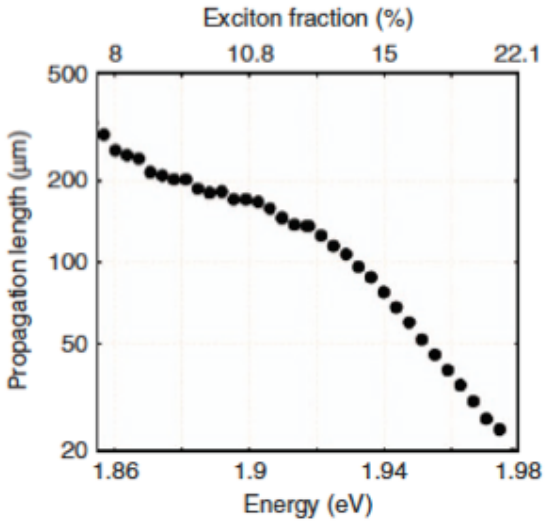

Figure 7.6 Lerario *et al*. demonstrated the relation between propagation length vs. the excitonic fraction of Bloch surface wave polaritons and their energies. The excitonic fraction and the energy of polaritons are determined by detunings.

7.4 Reference

[1] V. Bulovic, V. B. Khalfin, G. Gu, P. E. Burrows, D. Z. Garbuzov, and S. Forrest, Phys. Rev. B. Condens. Matter **58**, 3730 (1998).

[2] V. M. Agranovich, *Excitations in Organic Solids* (2009).

[3] P. Törmä and W. L. Barnes, Reports Prog. Phys. **78**, 13901 (2014).

[4] H. Haug and S. W. Koch, *Quantum Theory of the Optical and Electronic Properties of Semiconductors: Fivth Edition* (World Scientific Publishing Company, 2009).

[5] G. Panzarini, L. C. Andreani, A. Armitage, D. Baxter, M. S. Skolnick, V. N. Astratov, J. S. Roberts, A. V Kavokin, M. R. Vladimirova, and M. A. Kaliteevski, Phys. Solid State **41**, 1223 (1999).

[6] M. S. Skolnick, T. A. Fisher, and D. M. Whittaker, Semicond. Sci. Technol. **13**, 645 (1998).

[7] H. Deng, G. Weihs, C. Santori, J. Bloch, and Y. Yamamoto, Science (80-.). **298**, 199 (2002).

[8] H. Deng, H. Haug, and Y. Yamamoto, Rev. Mod. Phys. **82**, 1489 (2010).

[9] F. Li, L. Orosz, O. Kamoun, S. Bouchoule, C. Brimont, P. Disseix, T. Guillet, X. Lafosse, M. Leroux, J. Leymarie, M. Mexis, M. Mihailovic, G. Patriarche, F. Réveret, D. Solnyshkov, J. Zuniga-Perez, and G. Malpuech, Phys. Rev. Lett. **110**, 196406 (2013).

[10] T.-C. Lu, Y.-Y. Lai, Y.-P. Lan, S.-W. Huang, J.-R. Chen, Y.-C. Wu, W.-F. Hsieh, and H. Deng, Opt. Express **20**, 5530 (2012).

[11] S. Christopoulos, G. B. H. von Högersthal, A. J. D. Grundy, P. G. Lagoudakis, A. V Kavokin, J. J. Baumberg, G. Christmann, R. Butté, E. Feltin, J.-F. Carlin, and N. Grandjean, Phys. Rev. Lett. **98**, 126405 (2007).

[12] P. Bhattacharya, T. Frost, S. Deshpande, M. Z. Baten, A. Hazari, and A. Das, Phys. Rev. Lett. **112**, 236802 (2014).

[13] S. Kéna-Cohen and S. R. Forrest, Nat. Photonics **4**, 371 (2010).

[14] C. P. Dietrich, A. Steude, L. Tropf, M. Schubert, N. M. Kronenberg, K. Ostermann, S.

Höfling, and M. C. Gather, Sci. Adv. **2**, e1600666 (2016).

[15] S. K. Rajendran, M. Wei, H. Ohadi, A. Ruseckas, G. A. Turnbull, and I. D. W. Samuel, Adv. Opt. Mater. **7**, 1801791 (2019).

[16] K. S. Daskalakis, S. A. Maier, R. Murray, and S. Kéna-Cohen, Nat. Mater. **13**, 271 (2014).

[17] T. Cookson, K. Georgiou, A. Zasedatelev, R. T. Grant, T. Virgili, M. Cavazzini, F. Galeotti, C. Clark, N. G. Berloff, D. G. Lidzey, and P. G. Lagoudakis, Adv. Opt. Mater. **5**, 1700203 (2017).

[18] J. D. Plumhof, T. Stöferle, L. Mai, U. Scherf, and R. F. Mahrt, Nat. Mater. **13**, 247 (2013).

[19] H. Yanagi, F. Sasaki, and K. Yamashita, Adv. Opt. Mater. **7**, 1970066 (2019).

[20] L. Mazza, S. Kéna-Cohen, P. Michetti, and G. C. La Rocca, Phys. Rev. B **88**, 75321 (2013).

[21] M. Slootsky, Y. Zhang, and S. R. Forrest, Phys. Rev. B **86**, 45312 (2012).

[22] G. Lerario, A. Fieramosca, F. Barachati, D. Ballarini, K. S. Daskalakis, L. Dominici, M. De Giorgi, S. A. Maier, G. Gigli, S. Kéna-Cohen, and D. Sanvitto, Nat. Phys. **13**, 837 (2017).

[23] S. Kéna-Cohen, S. A. Maier, and D. D. C. Bradley, Adv. Opt. Mater. **1**, 827 (2013).

[24] C. R. Gubbin, S. A. Maier, and S. Kéna-Cohen, Appl. Phys. Lett. **104**, 233302 (2014).

[25] N. Bobrovska, M. Matuszewski, K. S. Daskalakis, S. A. Maier, and S. Kéna-Cohen, ACS Photonics **5**, 111 (2018).

[26] K. S. Daskalakis, S. A. Maier, and S. Kéna-Cohen, Phys. Rev. Lett. **115**, 1 (2015).

[27] H. Mizuno, H. Akagi, M. Tsubouchi, R. Itakura, H. Katsuki, and H. Yanagi, Jpn. J. Appl. Phys. **58**, 52003 (2019).

[28] X. H. Jin, M. B. Price, J. R. Finnegan, C. E. Boott, J. M. Richter, A. Rao, S. Matthew Menke, R. H. Friend, G. R. Whittell, and I. Manners, Science (80-.). **360**, 897 (2018).

[29] A. T. Haedler, K. Kreger, A. Issac, B. Wittmann, M. Kivala, N. Hammer, J. Köhler, H. W. Schmidt, and R. Hildner, Nature **523**, 196 (2015).

[30] H. Najafov, B. Lee, Q. Zhou, L. C. Feldman, and V. Podzorov, Nat. Mater. **9**, 938 (2010).

[31] V. M. Agranovich, M. Litinskaia, and D. G. Lidzey, Phys. Rev. B - Condens. Matter Mater. Phys. (2003).

[32] P. Michetti and G. C. La Rocca, Phys. Rev. B - Condens. Matter Mater. Phys. **71**, 115320 (2005).

[33] M. Litinskaya, Phys. Lett. Sect. A Gen. At. Solid State Phys. (2008).

[34] J. Schachenmayer, C. Genes, E. Tignone, and G. Pupillo, Phys. Rev. Lett. **114**, 196403 (2015).

[35] D. M. Myers, S. Mukherjee, J. Beaumariage, D. W. Snoke, M. Steger, L. N. Pfeiffer, and K. West, Phys. Rev. B **98**, 235302 (2018).

[36] S. K. Saikin, M. A. Shakirov, C. Kreisbeck, U. Peskin, Y. N. Proshin, and A. Aspuru-Guzik, J. Phys. Chem. C **121**, 24994 (2017).

[37] S. K. Saikin, A. Eisfeld, S. Valleau, and A. Aspuru-Guzik, Nanophotonics **2**, 21 (2013).

[38] J. Feist and F. J. Garcia-Vidal, Phys. Rev. Lett. **114**, 196402 (2015).

[39] G. Lerario, D. Ballarini, A. Fieramosca, A. Cannavale, A. Genco, F. Mangione, S. Gambino, L. Dominici, M. De Giorgi, G. Gigli, and D. Sanvitto, Light Sci. Appl. **6**, e16212 (2017).

[40] R. Pandya, R. Chen, Q. Gu, J. Sung, C. Schnedermann, O. S. Ojambati, R. Chikkaraddy, J. Gorman, G. Jacucci, O. D. Onelli, and others, ArXiv Prepr. ArXiv1909.03220 (2019).

[41] D. M. Coles, P. Michetti, C. Clark, W. C. Tsoi, A. M. Adawi, J.-S. Kim, and D. G. Lidzey, Adv. Funct. Mater. **21**, 3691 (2011).

[42] S. Pirotta, M. Patrini, M. Liscidini, M. Galli, G. Dacarro, G. Canazza, G. Guizzetti, D. Comoretto, and D. Bajoni, Appl. Phys. Lett. **104**, 51111 (2014).

[43] M. Liscidini, D. Gerace, D. Sanvitto, and D. Bajoni, Appl. Phys. Lett. **98**, 121118 (2011).

[44] R. Wang, H. Xia, D. Zhang, J. Chen, L. Zhu, Y. Wang, E. Yang, T. Zang, X. Wen, G. Zou, P. Wang, H. Ming, R. Badugu, and J. R. Lakowicz, Nat. Commun. (2017).

[45] F. Barachati, A. Fieramosca, S. Hafezian, J. Gu, B. Chakraborty, D. Ballarini, L. Martinu,

V. Menon, D. Sanvitto, and S. Kéna-Cohen, Nat. Nanotechnol. **13**, 906 (2018).

Chapter 8

Temperature Dependence of an Amorphous Organic Thin Film Polariton Laser

In Chapter 7, we reviewed previous works on organic polariton lasers. Over the years, the lasing threshold has been reduced. However, due to weak Coulomb interactions between tightly bound Frenkel excitons, the polariton lasing threshold remains comparable to conventional lasers. Improved insights and more detailed measurements [1] of temperature-dependent polariton interactions and relaxation from the exciton reservoir, which may be moderated by the non-radiative decay of excitons and polaritons, are needed to understand this apparently anomalous behavior. Previous works show a laser threshold dependence on temperature. [2,3] Thus, a systematic study on threshold and the polariton population distribution *vs.* temperature is needed.

8.1 Introduction

In this chapter, we investigate polariton density and lasing threshold in the temperature range from 16 K to room temperature (RT), and their relation to the photoluminescence (PL) of TDAF. An increase of laser threshold is observed at temperatures $T < 45$ K, that is accompanied by the bottleneck in the lower polariton branch (LPB) below lasing threshold. As the pumping fluence increases at low temperature, amplified spontaneous emission (ASE) is observed prior to lasing, whereas at RT, ASE is always coincident with lasing. In contrast to the changes within

the microcavity, bare TDAF films show a temperature-independent PL over the entire temperature range of $T < 115$ K.

8.2 Microcavity fabrication

The microcavity consists of a distributed Bragg reflector (DBR) comprising 8 pairs of 45 nm SiN_x/70 nm SiO_2 deposited by plasma-enhanced chemical vapor deposition on a sapphire substrate chosen for its high thermal conductivity. This is followed by a 115 nm thick TDAF film deposited using vacuum thermal evaporation (VTE) at a rate of 1 Å/s and a base pressure of ~10^{-7} torr. The second DBR, comprising 5 pairs of 40 nm ZnS/78 nm MgF_2, was deposited by VTE onto the organic film surface without exposure to air. A bare TDAF film was also deposited onto a sapphire substrate for temperature dependent PL measurements. All thicknesses and refractive indices were measured using variable angle spectroscopic ellipsometry.

The microcavity sample was non-resonantly pumped at a wavelength of $\lambda = 370$ nm from an optical parametric amplifier (TOPAS-C) pumped by a Clark-MXR CPA-series Ti: sapphire amplifier producing ~150 fs pulses at a repetition rate of 1000 Hz. The laser beam was focused to a ~150 μm diameter spot incident through the substrate at ~7^o from normal incidence. The pump power was controlled by a neutral density filter wheel and monitored using a calibrated Si detector (Coherent J-10Si-LE). Angle-resolved PL was collected from the film surface side with an angular resolution and step size of 2.5^o using a fiber bundle located on a rotating rail of a goniometer and connected to a spectrometer (Acton SP-2300i), with a 400 nm long-pass filter to eliminate stray pump light. A polarizer was placed in front of signal collection fiber bundle to distinguish between transverse electric (TE) and magnetic (TM) emission. The bare TDAF film was excited using illumination from a $\lambda = 340$ nm laser. All measurements were performed with the samples mounted inside a closed-cycle, temperature-controlled He cryostat.

8.3 Experimental results

The primary absorption peak of TDAF at 3.5 eV strongly couples with cavity photons, producing two polariton branches. Only the LPB emits light under pumping. Figures 8.1a and b show the PL intensity and full width at half maximum (FWHM) at the substrate normal (in-plane wavevector $k = 0$), respectively, at RT, 45 K and 16 K. All three data sets in Fig. 8.1a share the same three stages. Below threshold, the intensity sublinearly increases with the pumping fluence due to bi-exciton quenching. The threshold $P_{th} = 38 \pm 5$ μJ/cm^2 at $T > 45$ K, and increases to 51 ± 5 μJ/cm^2, and 67 ± 7 μJ/cm^2 at $T = 45$ K and 16 K, respectively, as shown in Fig. 8.1a inset. Above threshold, a superlinear increase in intensity is accompanied by spectral narrowing, followed by a saturation of intensity at a pump fluence of $P \sim 200$ μJ/cm^2. Immediately below and above threshold, the PL intensity (I) dependence on absorbed pump fluence follows the power law: $I = I_0 P^a$, with $a = 0.545 \pm 0.01$, 0.71 ± 0.3 and 0.52 ± 0.01 below threshold, and 2.47 ± 0.44, 2.26 ± 0.30 and 2.29 ± 0.15 above threshold at RT, 45 K and 16 K, respectively.

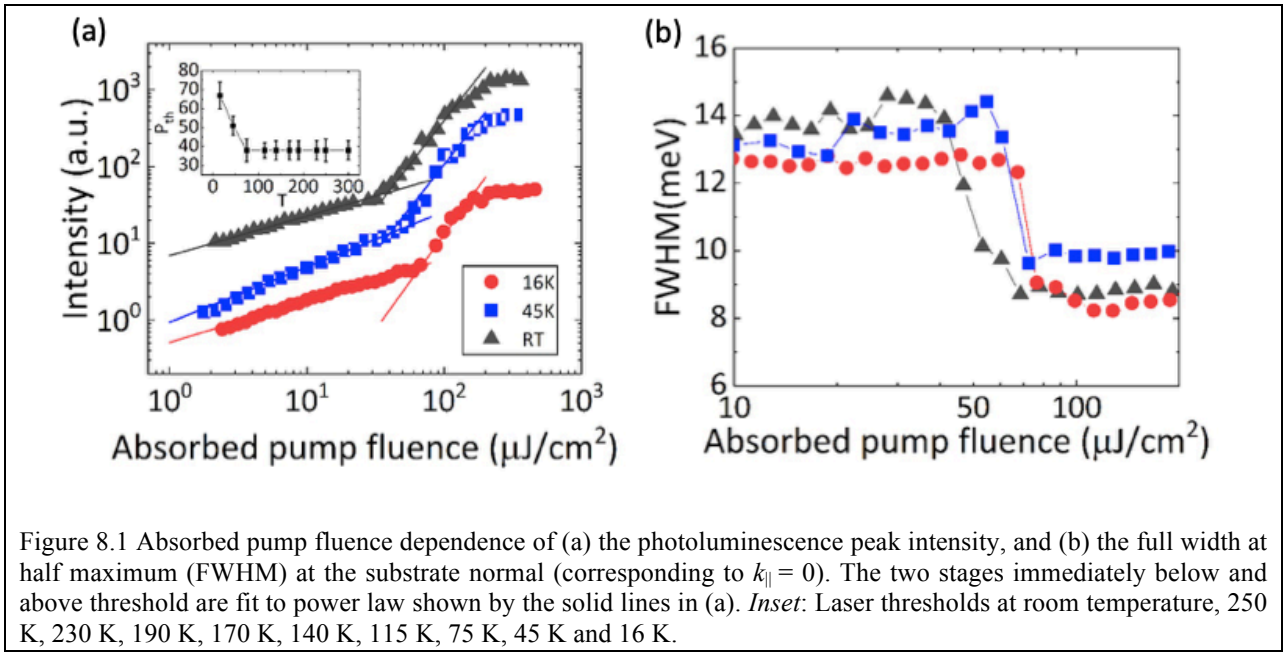

Figure 8.1 Absorbed pump fluence dependence of (a) the photoluminescence peak intensity, and (b) the full width at half maximum (FWHM) at the substrate normal (corresponding to $k_{||} = 0$). The two stages immediately below and above threshold are fit to power law shown by the solid lines in (a). *Inset*: Laser thresholds at room temperature, 250 K, 230 K, 190 K, 170 K, 140 K, 115 K, 75 K, 45 K and 16 K.

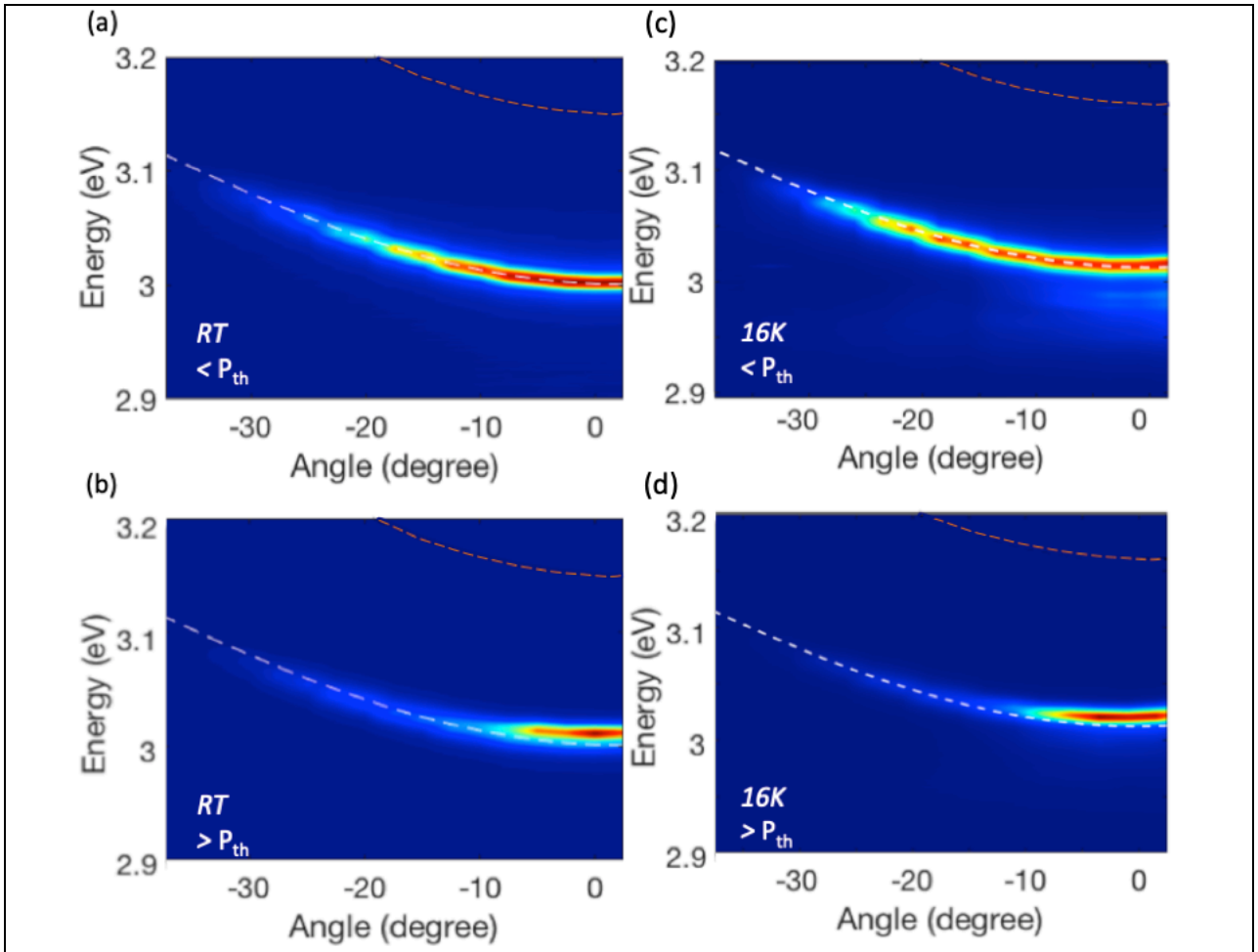

Figure 8.2 Angle-resolved photoluminescence spectra at pumping fluences of (a) $P \sim 0.9P_{th}$ and (b) $P \sim 3P_{th}$ at room temperature and (c) $P \sim 0.9P_{th}$ and (d) $P \sim 3P_{th}$ at 16K. The white and black lines are the dispersions of the lower polariton branch and cavity photons, respectively, using the coupled-oscillator model with fitting parameters in Table. 8.1.

The PL dispersion relations of TM polaritons below, $P \sim 0.9P_{th}$, and above, $P \sim 3P_{th}$, the lasing threshold, are shown in Figs. 8.2, at RT and 16 K. The dispersion is fit using coupled-oscillator model, [4] with fit parameters listed in Table 8.1. The energies at the bottom of the LPB are weakly temperature dependent, as shown in Figs. 8.2a and c, with the PL peak at $k = 0$ shifting from 3.001 eV at room temperature to 3.010 eV at 16 K. This blue shift results from the dependence of photon energy on thermal contraction of the cavity. As a result, the detuning, Δ, ranges from 340 meV to 355 meV between temperatures from 16 K and RT. This shift is small

compared to the half width of the TDAF PL spectrum and its polariton emission, allowing us to investigate reservoir dynamics in a straightforward manner. Below threshold, at both temperatures, the polariton populations decrease monotonically with increasing angle, as shown in Fig. 8.2a and c. The polaritons spread into higher energies at 16 K compared to RT. At 16 K, ASE leaks out of the reflector at $E \sim 2.96$ eV [1,4] near the substrate normal direction. The TE polarized PL intensity is similar as for the TM mode below threshold, and is one order of magnitude lower above threshold. At both temperatures, the PL emission spectrum collapses to the bottom of the LPB, which is a signature of reaching the lasing threshold. There is also a pronounced blueshift compared to below threshold, as observed in Fig. 8.2b and d.

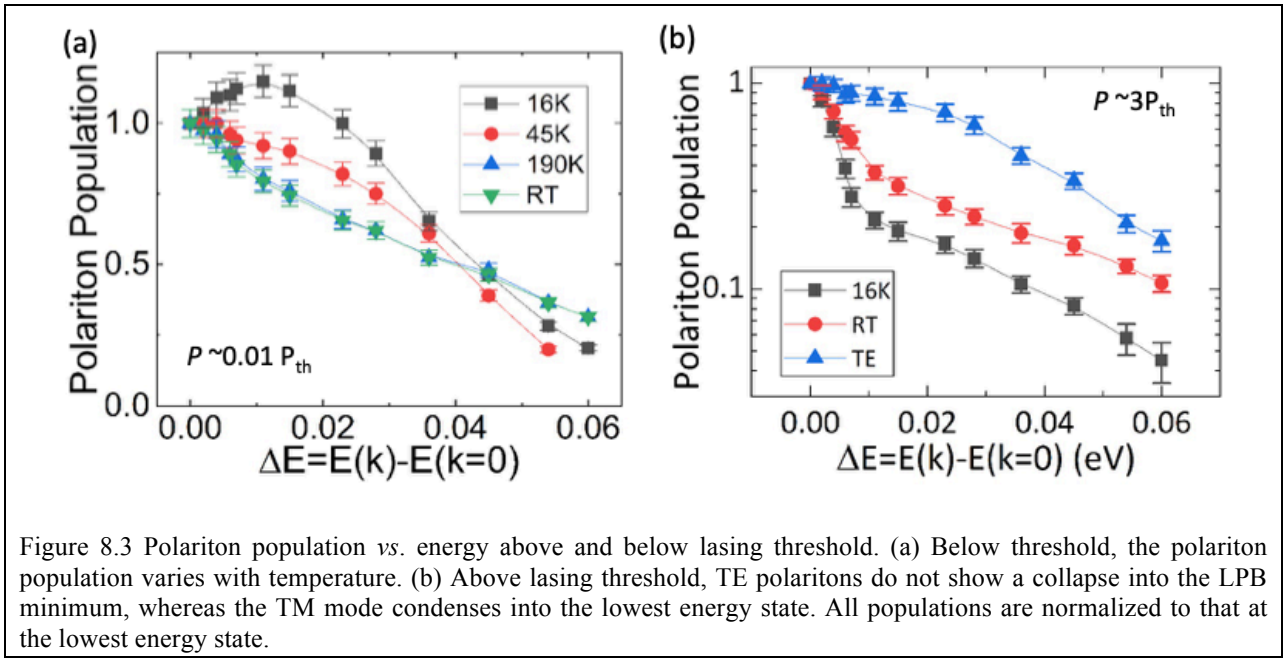

Figure 8.3 Polariton population *vs*. energy above and below lasing threshold. (a) Below threshold, the polariton population varies with temperature. (b) Above lasing threshold, TE polaritons do not show a collapse into the LPB minimum, whereas the TM mode condenses into the lowest energy state. All populations are normalized to that at the lowest energy state.

Table 8.1 Parameters fitting the polariton dispersion curves at RT and 16 K

Temperature	$E_{ph}(k=0)$ (eV)	n_{eff}	V (meV)
RT	3.145	2.11±0.02	536±4
16 K	3.160	2.11±0.03	536±5

The polariton population distributions within LPB at several temperatures are shown in Fig. 8.3. The polariton population, N, at different energies ($\Delta E = E(k) - E(k=0)$) is calculated using the PL intensity, I, and the photonic fraction $|\alpha|^2$ using the coupled-oscillator model, as $N(E) \propto I(E)/|\alpha(\mathrm{E})|^2$, and normalized to the energy at the bottom of the LPB. The PL intensities are measured at $P \sim 0.01P_{th}$ below threshold (Fig. 8.3a), and $3P_{th}$ above threshold (Fig. 8.3b). Below threshold, the distributions are identical at both RT and 190 K. At $T < 190$ K, the polariton population at $\Delta E \sim 15$ meV increases, with a sharper population decrease at higher energies. At 16 K, the bottleneck appears with a polariton distribution peak at $\Delta E \sim 10$ meV above the bottom of the LPB, at 3.02 eV. Above threshold, the TM polaritons collapse at all temperatures into the lowest energy state, while the TE polaritons do not, as shown in Fig. 8.3b.

The PL spectra from a TDAF film with no microcavity *vs*. temperature are shown in Fig. 8.4. At RT, the emission is broad and lacks structure. At $T < 115$ K, the emission exhibits clear vibronic peaks. Furthermore at $T < 115$ K the quantum yield increases by 40% relative to its value at RT, with a 75% increase in the 0-0 vibronic peak at 3.02 eV. The polariton population at 3.02 eV gradually increases with decreasing temperature, while the bare TDAF film shows no obvious spectral changes at $T < 115$ K. Although the TDAF film shows vibronic features, a monotonic decrease in the polariton population remains along the LPB to higher energy at $T > 45$ K. The TDAF 0-0 vibronic peak at 3.02 eV does not show up in the polariton microcavity until it

is cooled down to T = 16 K. The polariton emission energy, therefore, is more sensitive to temperature than that of the bare TDAF film.

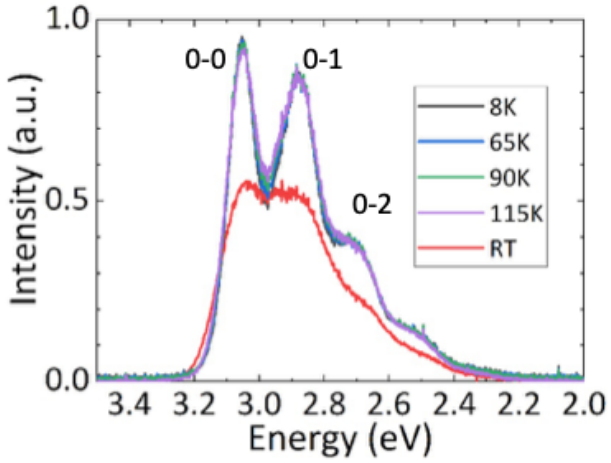

Figure 8.4 Photoluminescence spectra of a bare TDAF film at different temperatures. The spectral identification of each peak is shown. At T < 115 K, the PL spectra are temperature independent.

8.4 Discussion

As shown in Fig. 8.2c, the bottleneck at 3.02 eV disappears at $P \sim 0.9P_{th}$ compared to the population distribution at $P \sim 0.01P_{th}$ in Fig. 8.3a, even though stimulated scattering relaxation directly from the exciton reservoir does not guarantee polariton condensation at 16 K. This transition from bottleneck-limited relaxation to polariton lasing only occurs when the pumping fluence approaches the threshold $P \sim 0.9P_{th}$. However, whether this bottleneck disappearance results from the ASE or from exciton-polariton interactions remains unclear. Indeed, the lasing threshold depends sensitively on the degree of detuning. For example, a detuning that aligns the bottom of LPB with a vibronic or ASE peak of the active material may result in more efficient polariton relaxation into the lowest energy state, considering higher quantum yield and narrower vibronic emission at low temperatures. [3]

Despite the differences between polariton populations, polariton lasing is realized from T = 16 K to RT at a detuning $\Delta \approx 350$ meV. An increase in threshold occurs at low temperature as shown in Fig. 8.1, although the quantum yield of TDAF increases with decreasing temperature. TDAF polariton lasing is the result of a combination of relaxation from the exciton reservoir and along LPB into the energy minimum. [5] As temperature decreases, radiative pumping directly from excitons increases while relaxation along LPB decreases. These two mechanisms compete to maintain a temperature-independent laser threshold until phonon-polariton interactions become inefficient at $T < 45$ K. This inefficiency at low temperature can only be compensated by more exciton-polariton or polariton-polariton interactions, resulting in the high polariton laser thresholds.

8.5 Summary

In conclusion, we investigated the polariton population and lasing threshold in the temperature range of 16 K to RT in the archetype organic material, TDAF, and observe the lasing threshold remains unchanged at $P_{th} = 38 \pm 5$ μJ/cm^2 at temperatures $T > 45$ K, increasing to $P_{th} = 51 \pm 5$ μJ/cm^2 and 67 ± 7 μJ/cm^2 at $T = 45$ K and 16 K. The increased laser threshold is accompanied by a bottleneck in LPB below threshold. This dependence results from inefficient relaxation long LPB due to the lack of phonon scattering at low temperature. The unchanged laser thresholds at $T > 45$ K result from the competition between an increase in radiative pumping directly from the exciton reservoir, accompanied by a decrease in phonon-induced relaxation along LPB as temperature decreases.

8.6 Reference

[1] H. Mizuno, H. Akagi, M. Tsubouchi, R. Itakura, H. Katsuki, and H. Yanagi, Jpn. J. Appl. Phys. **58**, 52003 (2019).

[2] J. D. Plumhof, T. Stöferle, L. Mai, U. Scherf, and R. F. Mahrt, Nat. Mater. **13**, 247 (2013).

[3] M. Slootsky, Y. Zhang, and S. R. Forrest, Phys. Rev. B **86**, 45312 (2012).

[4] K. S. Daskalakis, S. A. Maier, R. Murray, and S. Kéna-Cohen, Nat. Mater. **13**, 271 (2014).

[5] H. Yanagi, F. Sasaki, and K. Yamashita, Adv. Opt. Mater. **7**, 1970066 (2019).

Chapter 9

Ultrastrong Coupling of Vibrationally Dressed Organic Frenkel Excitons with Bloch Surface Waves in an All-Dielectric Structure

When the Rabi splitting energy is nominally ≥10% of the uncoupled Frenkel exciton energy ($\hbar g \geq 0.1\hbar\omega_{ex}$), the ultrastrong coupling regime is reached. Exploration of this regime offers opportunities to investigate interesting quantum electrodynamics and nonlinear optical properties of organic materials.[2,3] Low-Q metallic cavities or surface plasmonic modes are commonly used to confine the optical field to induce ultrastrong coupling with a maximum coupling ratio of $g/\omega_{ex} = 0.31$. [4–10] However, metal cavities suffer from significant optical losses, thereby defeating many of the inherent advantages, such as long-range transport and optical nonlinearities found in this regime. All-dielectric structures with reduced loss are therefore desirable, but to our knowledge have yet to be realized.

9.1 Introduction

In this work, we show ultrastrong exciton-photon coupling in a one-sided structure comprising a distributed Bragg reflector (DBR) supporting a low-loss Bloch surface wave (BSW) [11–15] coated with a tetraphenyldibenzoperiflanthene (DBP) thin film (Fig. 9.1a inset). Multiple exciton-polariton branches with vibronic features are observed in both the strong and ultrastrong coupling regimes, and the separation between dominant absorptive polariton branches

increases with coupling strength. The measurements are interpreted using transfer matrix simulations and a coupled-oscillator model without rotating wave approximation. We analyze the coupling strengths and quantify their dependence on the number of absorbers and the electric field strength. This low-loss polaritonic structure enables long range exciton-polariton transport and high efficiency energy transfer in an ultrastrong coupling regime at room temperature.

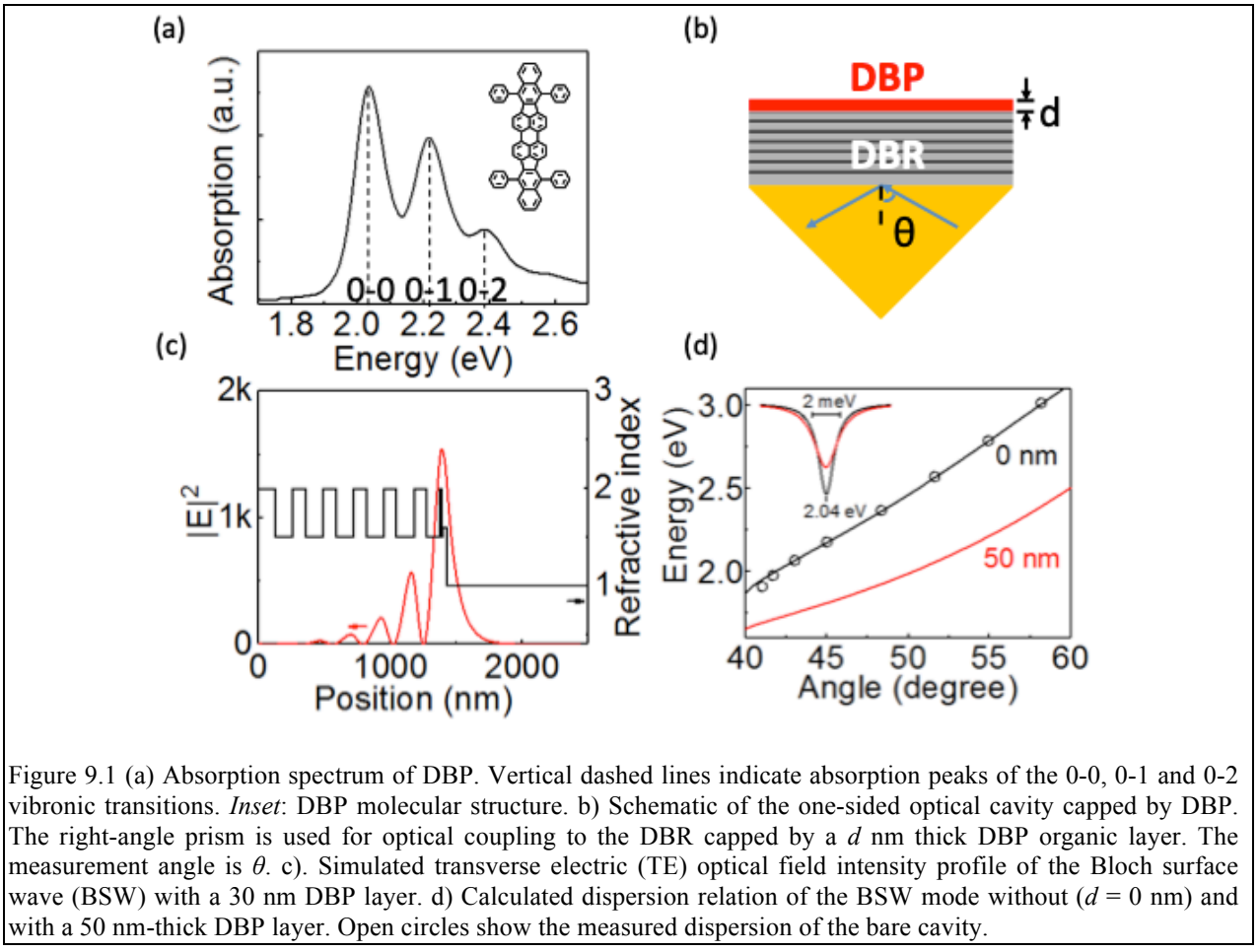

Figure 9.1 (a) Absorption spectrum of DBP. Vertical dashed lines indicate absorption peaks of the 0-0, 0-1 and 0-2 vibronic transitions. *Inset*: DBP molecular structure. b) Schematic of the one-sided optical cavity capped by DBP. The right-angle prism is used for optical coupling to the DBR capped by a d nm thick DBP organic layer. The measurement angle is θ. c). Simulated transverse electric (TE) optical field intensity profile of the Bloch surface wave (BSW) with a 30 nm DBP layer. d) Calculated dispersion relation of the BSW mode without (d = 0 nm) and with a 50 nm-thick DBP layer. Open circles show the measured dispersion of the bare cavity.

9.2 Theory

The rotating-wave approximation commonly used to describe strong coupling is not applicable in the ultrastrong regime. A full Hamiltonian containing both diamagnetic and anti-resonant terms is thus employed: [10]

$$H = \hbar \sum_q \sum_n \omega_{cav,q}\left(a_q^\dagger a_q + \frac{1}{2}\right) + \omega_{ex,n}\left(b_{q,n}^\dagger b_{q,n} + \frac{1}{2}\right)$$
$$+ \hbar \sum_q \sum_n D_q\left(a_q^\dagger a_q + a_q a_q^\dagger\right) + i g_q\left(a_q^\dagger b_{q,n} + b_q^\dagger a_{q,n}\right)$$
$$+ \hbar \sum_q \sum_n D_q\left(a_q a_{-q} + a_q^\dagger a_{-q}^\dagger\right) + i g_q\left(a_q b_{-q,n} + a_q^\dagger b_{-q,n}^\dagger\right) \qquad (9.1)$$

where q is the in-plane wavevector, $a^\dagger(a)$ and $b^\dagger(b)$ are creation (annihilation) operators for photons at energy $\hbar\omega_{cav}$ and a number n of excitons at energy $\hbar\omega_{ex,n}$, and D_q is the diamagnetic coupling constant. For one photon and three exciton oscillators (corresponding to the 0-0, 0-1 and 0-2 vibronic states of DBP), the 8 × 8 Hamiltonian matrix M is:

$$\begin{bmatrix}
\omega_{ph} + \frac{2D}{\hbar} & -ig_1 & -ig_2 & -ig_3 & -\frac{2D}{\hbar} & -ig_1 & -ig_2 & -ig_3 \\
ig_1 & \omega_{ex1} & 0 & 0 & -ig_1 & 0 & 0 & 0 \\
ig_2 & 0 & \omega_{ex2} & 0 & -ig_2 & 0 & 0 & 0 \\
ig_3 & 0 & 0 & \omega_{ex3} & -ig_3 & 0 & 0 & 0 \\
\frac{2D}{\hbar} & -ig_1 & -ig_2 & -ig_3 & -\omega_{cav} - \frac{2D}{\hbar} & -ig_1 & -ig_2 & -ig_3 \\
-ig_1 & 0 & 0 & 0 & ig_1 & -\omega_{ex1} & 0 & 0 \\
-ig_2 & 0 & 0 & 0 & ig_2 & 0 & -\omega_{ex2} & 0 \\
-ig_3 & 0 & 0 & 0 & ig_3 & 0 & 0 & -\omega_{ex3}
\end{bmatrix} \qquad (9.2)$$

where g_1, g_2, g_3 are the coupling strengths between the photon and three excitons, and

$$D \approx \sum_{i=1,2,3} \frac{{g_i}^2}{\omega_{ex,i}} \qquad (9.3)$$

Its eigenvector $(\alpha, \beta_1, \beta_1, \beta_1, x, y_1, y_2, y_3)^T$ contains Hopfield coefficients of the photon, three excitons and their virtual contributions.

9.3 Experimental results

A DBR consisting of 6 pairs of 100 nm thick SiN_x and 135 nm thick SiO_2 capped by 10 nm thick SiN_x and 15 nm thick SiO_2 layers were deposited by plasma enhanced chemical vapor deposition on a fused silica substrate. This was followed by depositing DBP films with different thicknesses (d = 2 nm to 50 nm), by vacuum thermal evaporation. Three well-resolved absorption peaks of DBP are shown in Fig. 9.1a. Optical constants of DBP were measured by spectroscopic ellipsometry and fitted with a Gaussian oscillator model yielding three exciton resonance energies of $\hbar\omega_{ex,i}$ = 2.04 eV, 2.22 eV and 2.38 eV (i =1, 2, 3) corresponding to the vibronic progression 0-0, 0-1 and 0-2, respectively. The full width at half maxima (FWHM) were $\Gamma_{1\text{-}3}$ = 133 meV, 141 meV and 147 meV, the relative oscillator strengths were $f_1 : f_2 : f_3$ = 1:0.82:0.39, and the background dielectric constant [16] was ε_∞ = 3.0. The Kretschmann configuration was used in the angle-resolved reflectivity measurements to observe the polaritons with the DBP layer capping the DBR. A glass prism was attached to the substrate using index-matching fluid (refractive index n = 1.5), as shown in Fig. 9.1b.

To extract the coupling-strengths between excitons and photons, BSW dispersion relations with different DBP layer thicknesses (d) are calculated using transfer matrix simulations. The calculation uses an equivalent organic layer on top of the DBR with the background dielectric constant of DBP, which accounts for all other resonant frequencies. A transverse electric (TE) polarized BSW mode is supported by the DBR and confined to a small volume (~λ/4, λ being the resonant wavelength), with the field intensity peak just beneath the

organic layer (Fig. 9.1c). Figure 9.1d shows the simulated BSW dispersion relation of the DBR capped with a DBP layer with d = 50 nm. For comparison, the dispersion relation of the DBR with a free top surface (black line: simulation, open circles: measurement) is also shown. Compared with the free surface DBR (d = 0 nm), the BSW on the DBR capped with DBP (red line) exhibits a red-shifted energy cutoff, and the dispersion relation is perturbed by partial hybridization with the guided modes, consistent with previous reports. [17] Both open cavities showed narrow resonance dips centered at 2.04 eV (Fig. 9.1d, inset), and a calculated $Q \sim 10^3$.

The TE reflectivity spectra of a 30 nm (left) and 50 nm (right) thick DBP-loaded DBR above the total internal reflection angle are simulated, as shown in Figs. 9.2a and b. Four branches (guided by red dashed lines) between 1.6 eV and 2.5 eV are separated from three uncoupled vibronic states 0-0, 0-1, 0-2 (indicated by vertical dashed lines from left to right). All of the predicted features are readily distinguished in the prism-coupled measurements in Fig. 9.2c and d. The low reflectivity below 1.6 eV or above 2.5 eV is due to the DBR stop band and absorption of SiN_x and the broadening is primarily due to the angular spread of the prism coupled beam as well as the limited angular resolution of our setup. At all angles, the lowest-energy reflectivity dip is relatively strong and narrow, and it shifts to higher energy with increasing angle. Other dips are relatively weak and broad. The energy of the dip between the 0-0 and 0-1 vibronic is independent of angle, while that of the dip between 0-1 and 0-2 increases slightly with angle. The highest-energy dip (above the 0-2 transition) emerges above 46^o and blue shifts with increasing angle. For all simulations, the contrast in reflectivity is small, especially at high angles.

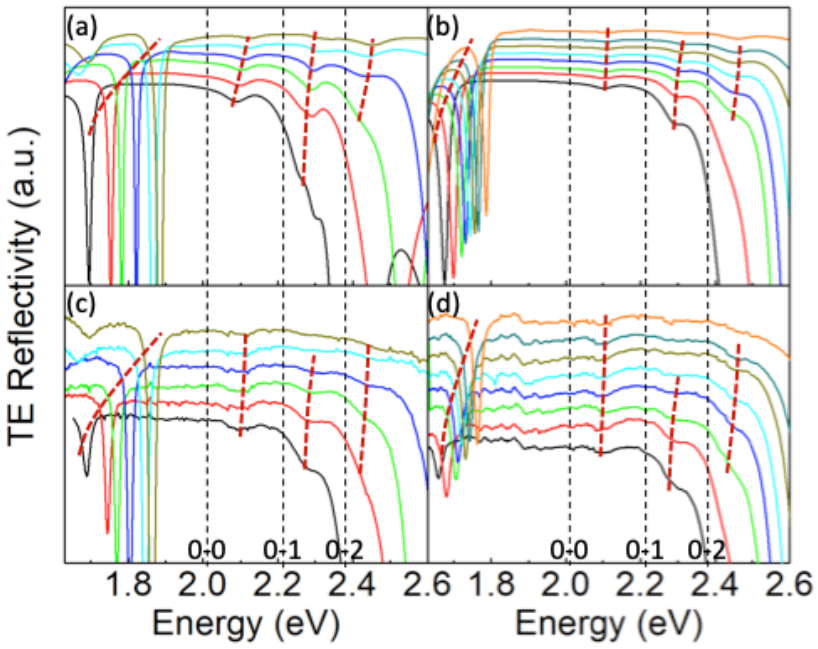

Figure 9.2 Simulated TE-polarized reflectivity spectra of a (a) d = 30 nm thick DBP layer on a DBR at incidence angles of 41.7°, 44.3°, 45.7°, 47.7°, 50.3°, 51.6° and (b) d = 50 nm thick DBP layer on a DBR at incidence angles of 44.3°, 45.7°, 47°, 47.6°, 48.3°, 49°, 49.6°, 50.9° (curves from bottom to top). Measurements corresponding to (a) and (b) are shown in (c) and (d), respectively. Red dashed lines provide guides for the polariton branches; vertical black dashed lines indicate the uncoupled exciton energies. Four polariton branches are observed from low to high energy: the lower (LP), first middle (MP1), second middle (MP2), and upper polariton branch (UP).

The reflectivity minima of the measured spectra of the 50 nm-thick sample are extracted assuming a Gaussian lineshape and are plotted in Fig. 9.3a. The lower (LP), first middle (MP1), second middle (MP2) and upper (UP) branches are observed with anti-crossing features near three uncoupled exciton resonant energies (three horizontal dashed lines), a signature of exciton-photon coupling. Large splitting observed between LP and MP1 indicates a large coupling strength and thus g/ω_{ex} ratio, probably leading to an invalidation of rotating-wave approximation.

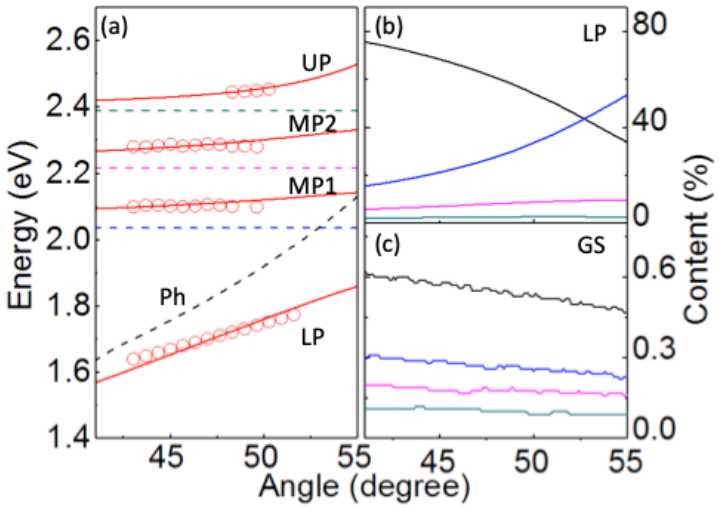

Figure 9.3 Dispersion relations of BSW-exciton polaritons in the ultrastrong-coupling regime (d = 50 nm). (a) Least-squares fit (solid lines) to data (circles) of the angle-dependent reflectivity minima. The fits assume three coupled oscillators with coupling strengths of g_1 = 205 meV, g_2 = 177 meV, and g_3 = 136 meV. Colored horizontal dashed lines are guides for the uncoupled 0-0, 0-1, 0-2 exciton energies; black dashed line: calculated dispersion of the BSW photon (Ph). (b) Hopfield coefficients of LP: photon (black line) and three excitons (colored lines). (c) Virtual photon (black) and exciton (colored) content of the polariton ground state (GS).

9.4 Discussion

To estimate coupling strengths and vacuum Rabi splitting energies, we fit the measured data with the 8 × 8 Hamiltonian matrix, where the uncoupled photon energy ($\hbar\omega_{ph}$) is calculated using the transfer matrix method, and the several vibronic transitions are treated as individual exciton states. [18] The least-squares fit yields coupling strengths of $\hbar g_1$ = 205 meV, $\hbar g_2$ = 177 meV, and $\hbar g_3$ = 136 meV. Using a photon linewidth of Γ_{cav} = 5 meV, and an exciton width Γ_{ex} = 133 meV, the vacuum Rabi splitting energy is:

$$\hbar\Omega_i = \sqrt{4\hbar g_i^2 - \left(\Gamma_{ex} - \Gamma_{ph}\right)^2} \qquad (i = 1, 2, 3) \tag{9.4}$$

The extracted Rabi splitting energies $\hbar\Omega_1$ = 389 meV, $\hbar\Omega_2$ = 329 meV, $\hbar\Omega_3$ = 238 meV are larger than spectral widths of uncoupled photon and exciton states. Thus, $g_1/\omega_{ex,1} \approx 0.1$ confirms

ultrastrong coupling regime has been reached. The Hopfield coefficients of LP are shown in Figure 9.3b. Similar fitting for samples with thicknesses of 3 - 40 nm (not shown here) indicate that they do not reach the ultrastrong coupling regime.

In the ultrastrong regime, the virtual contributions to the polariton ground state cannot be ignored. The virtual photon content ($|x_{LP}|^2+|x_{MP1}|^2+|x_{MP2}|^2+|x_{UP}|^2$) and virtual exciton contributions ($|y_{i,LP}|^2+|y_{i,MP1}|^2+|y_{i,MP2}|^2+|y_{i,UP}|^2$) are calculated and shown in Fig. 9.3c. The virtual photon content is approximately 0.55% per state, and the contents of virtual excitons 0-0, 0-1 and 0-2 are 0.2%, 0.15%, and 0.1% to the ground state, respectively.

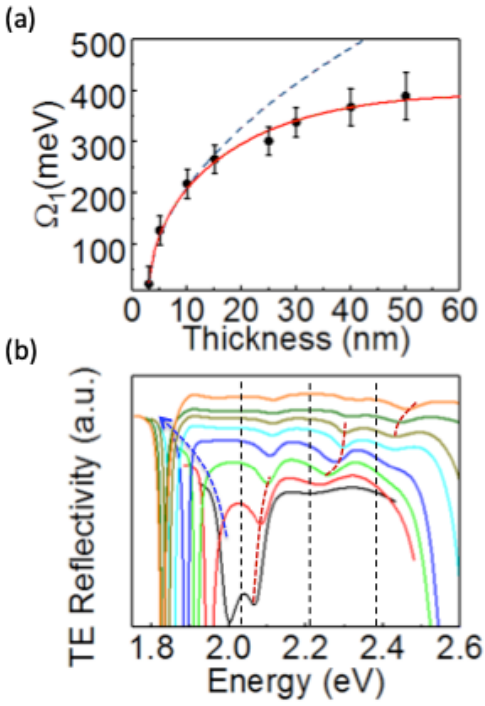

Figure 9.4 (a) Vacuum Rabi splitting energy vs. DBP thickness. Dots are the extracted vacuum Rabi splitting energies ($\hbar\Omega_1$). The dashed line is a fit to the constant field approximation. The solid line accounts for field attenuation, with fitting parameters A' = 4.45±0.50 eV, l = 53 ± 8 nm, and d_0 = 2.9 ± 0.8 nm. (b) Simulated reflectivity of samples with d = 2, 5, 10, 15, 25, 30, 40, and 50 nm (curves from bottom to top) at angles corresponding to ω_{cav}-ω_{ex1} = 0. Blue dashed line is a guide for the evolution of low-energy absorption peak, and red dashed lines guide for the high-energy absorption peak as coupling strength increases.

The Rabi splitting energy ($\hbar\Omega_1$) monotonically increases with DBP layer thickness as shown in Fig. 9.4a. The coupling strength is increased with $\sqrt{N}$, where N is the number of molecules, which is proportional to organic layer thickness, d. Thus, the Rabi splitting energy is fit using $\hbar\Omega(d) = A\sqrt{d - d_0}$, shown as the dashed line, where A is a constant, and d_0 is the critical DBP thickness demarking the transition from weak to strong coupling. Although thin DBP samples with d < 15 nm can be fit by this expression, a slower increase in $\hbar\Omega(d)$ is observed at greater thickness. This deviation results from the exponential attenuation in electric field with distance from the DBR surface, as shown in Fig. 9.1c. To account for the reduction in field intensity with distance, we integrate over the film thickness *viz.*:

$$\hbar\Omega(d) \propto 2\mu\sqrt{N}\bar{E} = 2\mu\sqrt{N}\int_0^d \frac{e^{-x/l}}{d}dx = A'\frac{1 - e^{-\frac{d-d_0}{l}}}{\sqrt{d - d_0}} \tag{9.5}$$

where the characteristic field decay length is l, μ is molecular transition dipole moment, and A', d_0 and l are fitting parameters. A fit to this expression is indicated by the solid line in Fig. 9.4a.

It is interesting to study the energy shift of the polariton branches and their absorption as the coupling strength becomes comparable with the vibrational frequency ($g \sim \omega_v$). [19,20] Figure 9.4b shows the simulated reflectivity of samples with different organic layer thicknesses, namely with different coupling strengths between 0-0 excitons and BSW photons. The angle for each thickness is chosen such that the BSW photon is resonant with the 0-0 exciton-photon. With larger coupling strengths, all polariton branches detune from the exciton energies except for MP1, that remains constant when g_1 is comparable with the phonon energy. As the coupling strength increases, the most intense polariton absorption remains located at the lowest branch, while the dominant polariton absorption at the higher energy side shifts from MP1 to MP2 and UP. This trend can also be found in the experimental reflectivity spectrum.

9.5 Summary

Ultrastrong coupling of Frenkel excitons and BSW photons is demonstrated in an all-dielectric, one-sided photonic structure. It is striking that in this ultrastrong regime, we still observe reflectivity from the middle vibronic polariton branches. Using a coupled-oscillator model, coupling strengths as large as 205 meV ($\hbar\Omega_1$ = 389 meV) are extracted, corresponding to $g/\omega_{ex} \approx 0.1$. We analyze the thickness dependence of the reflectivity spectra and find that the coupling strength is tuned by balancing the layer thickness with the electric field amplitude at the surface of the DBR. The evolution of vibronic polariton branches shows that the dominant polariton branches diverge with increasing coupling strength. The all-dielectric structure extends the application space available to investigate polariton physics, such as ultralong-range polariton propagation, energy transfer and nonlinear optical effects in the ultrastrong regime.

9.6 Reference

[1] D. Lidzey, D. Bradley, M. Skolnick, T. Virgili, S. Walker, and D. Whittaker, Nature **395**, 53 (1998).

[2] P. Forn-Díaz, L. Lamata, E. Rico, J. Kono, and E. Solano, ArXiv Prepr. ArXiv1804.09275 (2018).

[3] A. F. Kockum, A. Miranowicz, S. De Liberato, S. Savasta, and F. Nori, Nat. Rev. Phys. **1**, (2018).

[4] T. Schwartz and T. W. Ebbesen, Phys. Rev. Lett. **106**, 196405 (2011).

[5] S. Balci, Opt. Lett. **38**, 4498 (2013).

[6] S. Kéna-Cohen, S. A. Maier, and D. D. C. Bradley, Adv. Opt. Mater. **1**, 827 (2013).

[7] F. Barachati, J. Simon, Y. A. Getmanenko, S. Barlow, S. R. Marder, and S. Kéna-Cohen, ACS Photonics **5**, 119 (2018).

[8] A. Cacciola, O. Di Stefano, R. Stassi, R. Saija, and S. Savasta, ACS Nano **8**, 11483 (2014).

[9] M. Held, A. Graf, Y. Zakharko, P. Chao, L. Tropf, M. C. Gather, and J. Zaumseil, Adv. Opt. Mater. **6**, 1700962 (2018).

[10] F. Le Roux and D. D. C. Bradley, Phys. Rev. B **98**, 1 (2018).

[11] M. Liscidini, D. Gerace, D. Sanvitto, and D. Bajoni, Appl. Phys. Lett. **98**, 121118 (2011).

[12] S. Pirotta, M. Patrini, M. Liscidini, M. Galli, G. Dacarro, G. Canazza, G. Guizzetti, D. Comoretto, and D. Bajoni, Appl. Phys. Lett. **104**, 51111 (2014).

[13] F. Barachati, A. Fieramosca, S. Hafezian, J. Gu, B. Chakraborty, D. Ballarini, L. Martinu, V. Menon, D. Sanvitto, and S. Kéna-Cohen, Nat. Nanotechnol. **13**, 906 (2018).

[14] S. Pirotta, M. Patrini, M. Liscidini, M. Galli, G. Dacarro, G. Guizzetti, D. Comoretto, and D. Bajoni, Opt. Lett. **39**, 2068 (2014).

[15] G. Lerario, D. Ballarini, A. Fieramosca, A. Cannavale, A. Genco, F. Mangione, S. Gambino, L. Dominici, M. De Giorgi, G. Gigli, and D. Sanvitto, Light Sci. Appl. **6**, e16212 (2017).

[16] V. M. Agranovich, *Excitations in Organic Solids* (OUP Oxford, 2009).

[17] R. Wang, H. Xia, D. Zhang, J. Chen, L. Zhu, Y. Wang, E. Yang, T. Zang, X. Wen, G. Zou, P. Wang, H. Ming, R. Badugu, and J. R. Lakowicz, Nat. Commun. **8**, (2017).

[18] R. J. Holmes and S. R. Forrest, Phys. Rev. Lett. **93**, 1 (2004).

[19] F. Herrera and F. C. Spano, Phys. Rev. Lett. **118**, 1 (2017).

[20] M. A. Zeb, P. G. Kirton, and J. Keeling, ACS Photonics **5**, 249 (2018).

Chapter 10

Ultralong-Range Energy Transport in Disordered Organic Semiconductors at Room Temperature via Coherent Exciton-Polariton Propagation

In the last chapter, we studied the coupling strength between Bloch surface photons and excitons. Angular reflectivity measurements show two anti-crossing polariton branches with a giant vacuum Rabi splitting energy of 480 meV due to ultrastrong coupling between 0-0 vibronic of molecular excitons and Bloch surface modes. In this chapter, we use the same system to investigate polariton propagation. Measurements by selective photoluminescence imaging in both real and Fourier spaces indicate long-range polariton transport of up to 80 μm and a halo-like intensity pattern due to polariton self-interference.

10.1 Methods

10.1.1 Device fabrication

The DBR was fabricated by sequentially depositing 4 pairs of ZnS (90 nm) and MgF_2 (148 nm) on a 180 micrometer-thick fused silica substrate via thermal evaporation in a vacuum chamber with a base pressure of 10^{-7} torr. Then a 20 nm-thick DBP layer was deposited on top of the DBR by vacuum thermal evaporation, followed by encapsulation using a thin fused silica lid sealed in an ultrapure N_2 environment to the substrate peripherally sealed using ultraviolet cured epoxy with an approximately 1 mm gap between lid and substrate.

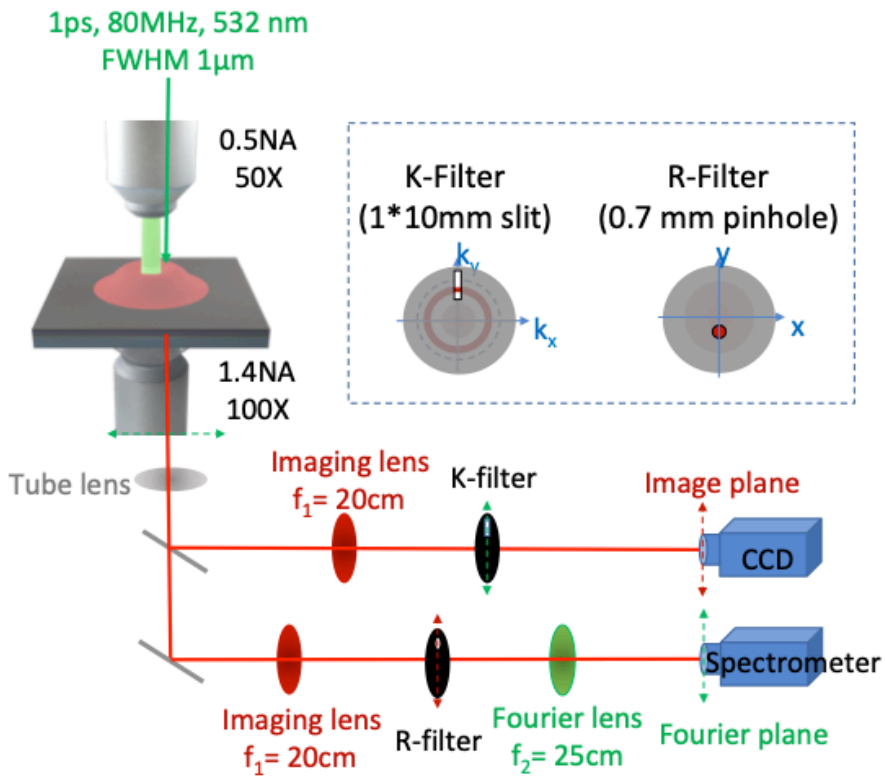

Figure 10.1 Optical measurement setup for k-space and real space.

10.1.2 Optical measurements

The angular reflectivity was measured using a k-space microscope comprising an inverted microscope (Olympus), a white tungsten halogen white lamp source, and a spectrometer (Acton SpectraPro SP-2500) with a 1024 x 1024 CCD camera (PIX 1024B, Princeton Instruments). The measurement was conducted in a reflection geometry with a 1.40 NA, 100X oil-immersed objective. The k-space image was reconstructed at the entrance of the spectrometer using an achromatic lens (Thorlabs), and the reflected light is filtered by a linear TE polarizer. The angular photoluminescence spectra were also collected with a similar microscope setup, using TM-polarized λ = 532 nm ultrafast pulsed laser source (pulse width of 1 ps, repetition time of 80 MHz, power of 1 µW; Toptica Fibre-Pro) and a λ = 600 nm long pass filter (Thorlabs) in the light collection path. The photoluminescence images were collected by the k-space

microscope in a transmission geometry using the set-up in Fig. 10.1. A 1 μm diameter TE-polarized pulsed Gaussian laser beam was focused on the surface of the DBP layer with a 0.5NA, 50X objective. Emission was collected as above. In the collection channel for k-space-filtered real space imaging, a 5 cm diameter achromatic lens was used to reconstruct the real-space image at the entrance of a CCD camera. A 1 mm x 10 mm slit was placed in the reconstructed k-plane after the lens and moved by a micromanipulator to admit only light with the desired k. The position of slit was confirmed by a flip lens. For wavelength-resolved propagation measurements, the CCD camera was replaced with a spectrometer. The position of the slit filter has a significant effect on the propagation pattern, and the edge of the slit may diffract the detecting light, resulting in an additional shift of the propagation pattern as well as the generation of optical fringes. To avoid edge diffraction, the slit edge was placed slightly below the air cone where there was only negligible exciton emission. In the collection channel for real-space-filtered k-space photoluminescence imaging, the real-space image was reconstructed by a 5 cm diameter achromatic lens. A 500 μm pinhole was used to select a particular area, and its position in this real-space image plane was confirmed by a flip lens. The filtered light passed through another 5 cm diameter achromatic lens and projected onto the spectrometer at the k-plane.

10.2 Experimental results

The DBR supports a single transverse-electric (TE) Bloch surface wave (BSW) above the total internal reflection (TIR) angle (θ_{TIR} = 42^{o}) at the glass-air interface. The DBP film is amorphous and has three clearly distinguishable vibronic peaks (0-0, 0-1, 0-2) of its lowest spin-singlet exciton, corresponding to the three absorption peaks (560 nm, 580 nm and 610 nm) and Stokes-shifted emission peaks (610 nm, 670 nm and 720 nm) in Fig. 10.2a. The simulated TE angular reflectivity spectrum of the structure using transfer matrix formalism is shown in Fig.

10.2a. In the spectrum, two photonic modes can be distinguished: one comprises weakly-coupled parabolic modes at the upper edge of the DBR upper stop band (USB) spanning both below and above the TIR angle, and the other due to the anti-crossing modes (upper polariton branch: UP, lower polariton branch: LP) existing at $\theta > \theta_{TIR}$. All TE modes are directly visualized by the white-light angular reflectivity measurement shown in Fig. 10.2a. Specifically, the reflectivity dip of the LP is sharp and faint, indicating the high-quality factor of the coupled BSW. The dip in UP broadens near the 0-2 transition, and narrows when approaching higher in-plane momentum, $n_0 \sin\theta$, that is at higher angle. (Here, n_0 is the glass index of refraction.) These two polariton branches provide clear evidence of strong coupling between photons and excitons, which is absent in previous reports of polariton propagation.

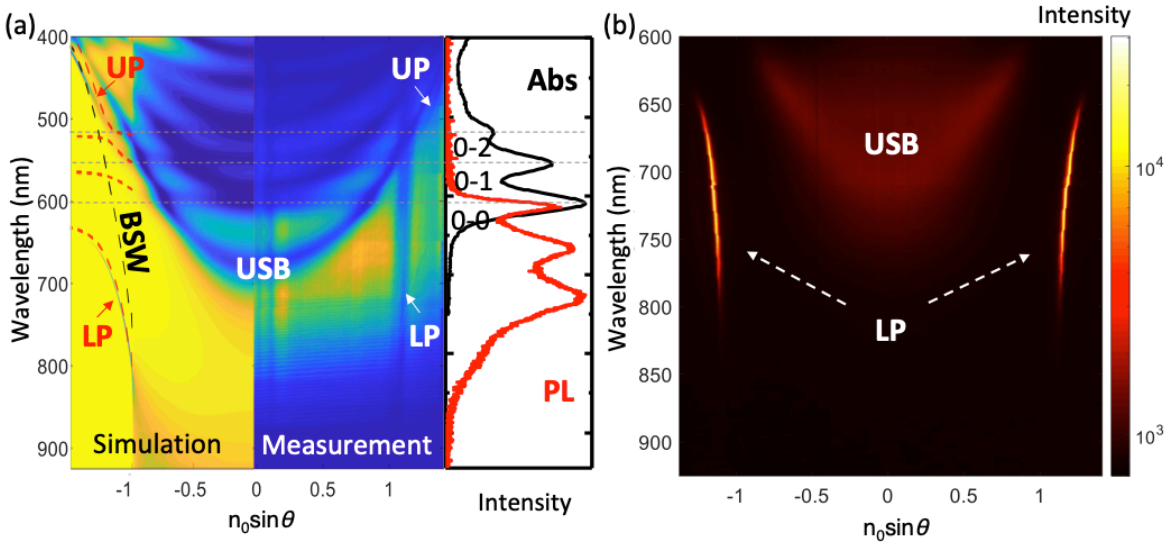

Figure 10.2 Ultrastrong coupling between DBP and Bloch surface waves (BSW). (a) Simulated (left) and measured (middle) transverse electric (TE) angular reflectivity spectra of ultrastrong coupled vibronic excitons of DBP (horizontal gray dashed-lines) and the BSW (red dashed-line). Red dashed lines show four fit polariton branches (UP: upper polariton branch, LP: lower polariton branch) using the coupled-oscillator model. Absorption and photoluminescence spectra (right) of uncoupled DBP shows the vibronic progressions; (b) Measured TE angular photoluminescence spectra of the ultrastrong coupled sample.

We measured the TE angular photoluminescence emission spectrum of an encapsulated sample using a *k*-space microscope. As shown in Fig. 10.2b, there is significant leakage of exciton emission from the USB at $\theta < \theta_{TIR}$ due to the limited spectral range of the DBR stop band. At angles greater than TIR, only the lowest polariton branch LP is observed, and the maximum intensity is close to the emission peak of the 0-2 vibronic (Fig. 10.2a), indicating phonon-assisted polariton relaxation. [1]

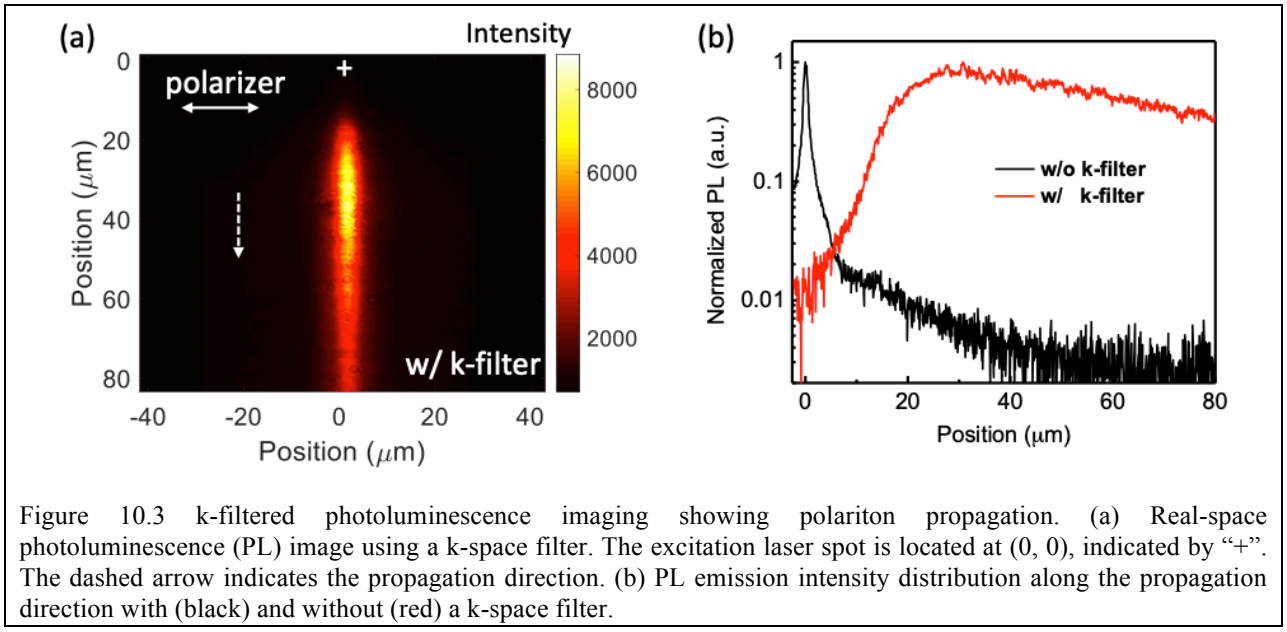

Figure 10.3 k-filtered photoluminescence imaging showing polariton propagation. (a) Real-space photoluminescence (PL) image using a k-space filter. The excitation laser spot is located at (0, 0), indicated by "+". The dashed arrow indicates the propagation direction. (b) PL emission intensity distribution along the propagation direction with (black) and without (red) a k-space filter.

To track the polariton propagation, we image the spatial distribution of photoluminescence non-resonantly exciting the sample at normal incidence using the similar setup, where the spectrometer is replaced with a CCD camera. The photoluminescence image is now dominated by an intense and bright emission at the excitation spot due to the Gaussian spatial profile of the 1 μm diameter laser beam. Outside of this bright spot, relatively weaker emission radially spreads beyond the field of view. To rule out the exciton emission leakage from the USB, we place a slit in the reconstructed in-plane momentum *k*-space behind the imaging collection lens, and select only the high-*k* polariton emission at $\theta > \theta_{TIR}$, as shown in

Fig. 10.3a. The polariton emission propagates in the direction selected by the slit. Surprisingly, the polariton emission intensity is weak near the excitation spot, has a peak at a distance of approximately 20 μm, and then decays exponentially along the propagating path beyond the field of view that extends to 80 μm (Fig. 10.3b). For comparison, the emission profile taken in the absence of a *k*-space filter is also shown, where a long and weak emission tail overlap the narrow and intense peak at the pumping position.

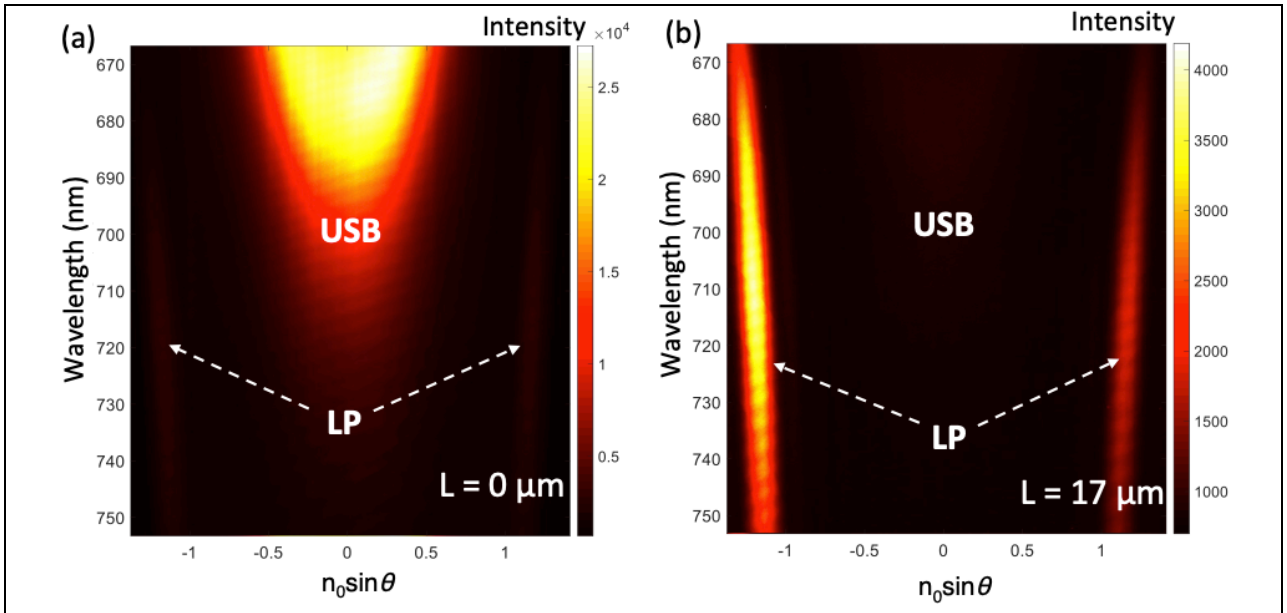

Figure 10.4 Selected-area angular PL spectra showing the origin of the emission. (a) k-space filtered PL dispersion of selected area at the position (a) L = 0 μm and (b) L = 17 μm from the laser excitation spot.

We further select a portion of area at the intermediate image plane with a pinhole filter to probe the spectral dispersion as a function of position. When the pinhole coincides with the excitation spot corresponding to observation distance L = 0, a similar angular photoluminescence spectrum is obtained (Fig. 10.4a), although the primary emission is from excitons in the USB rather than from LP. As the pinhole is moved away from the excitation spot (increasing L) along the propagation direction, the weight of the polariton emission from LP increases, consistent with the propagation pattern observed in Fig. 10.3. At L = 17 μm and beyond, the emission is

dominated by the forward-propagating LP branch with a positive in-plane momentum (see Fig. 10.4b), while the backward-propagating LP with a negative in-plane momentum emission is also observed at high pumping power.

Table10.1 Parameters of the interference model used to fit the propagation profiles in Fig. 10.2c.

Wavelength (nm)	670	690	710	730	750
μ (μm^{-1})	0.014	0.032	0.045	0.059	0.073
α (μm^{-1})	0.039	0.016	0.013	0.01	0.009

10.3 Theory

Angular reflectivity of the sample was simulated using the transfer matrix method using the measured refractive indexes of ZnS (n=2.3) and MgF_2 (n=1.4). The uncoupled Bloch surface mode was calculated using the background refractive index of 1.75 for DBP.

The polariton propagation pattern is due to self-interference of modes as illustrated in Fig. 10.5b. Consider two plane wave components emitted from a DBP exciton whose transition dipole moment is oriented parallel to the substrate plane. The propagation proceeds at angle, θ (path 1), and $-\theta$ (path 2). When (π - θ) is larger than the critical angle between DBP and air (θ_c), path 2 experiences TIR at the top DBP surface, resulting in a phase difference between paths 1 and 2. The phase difference φ is given by:

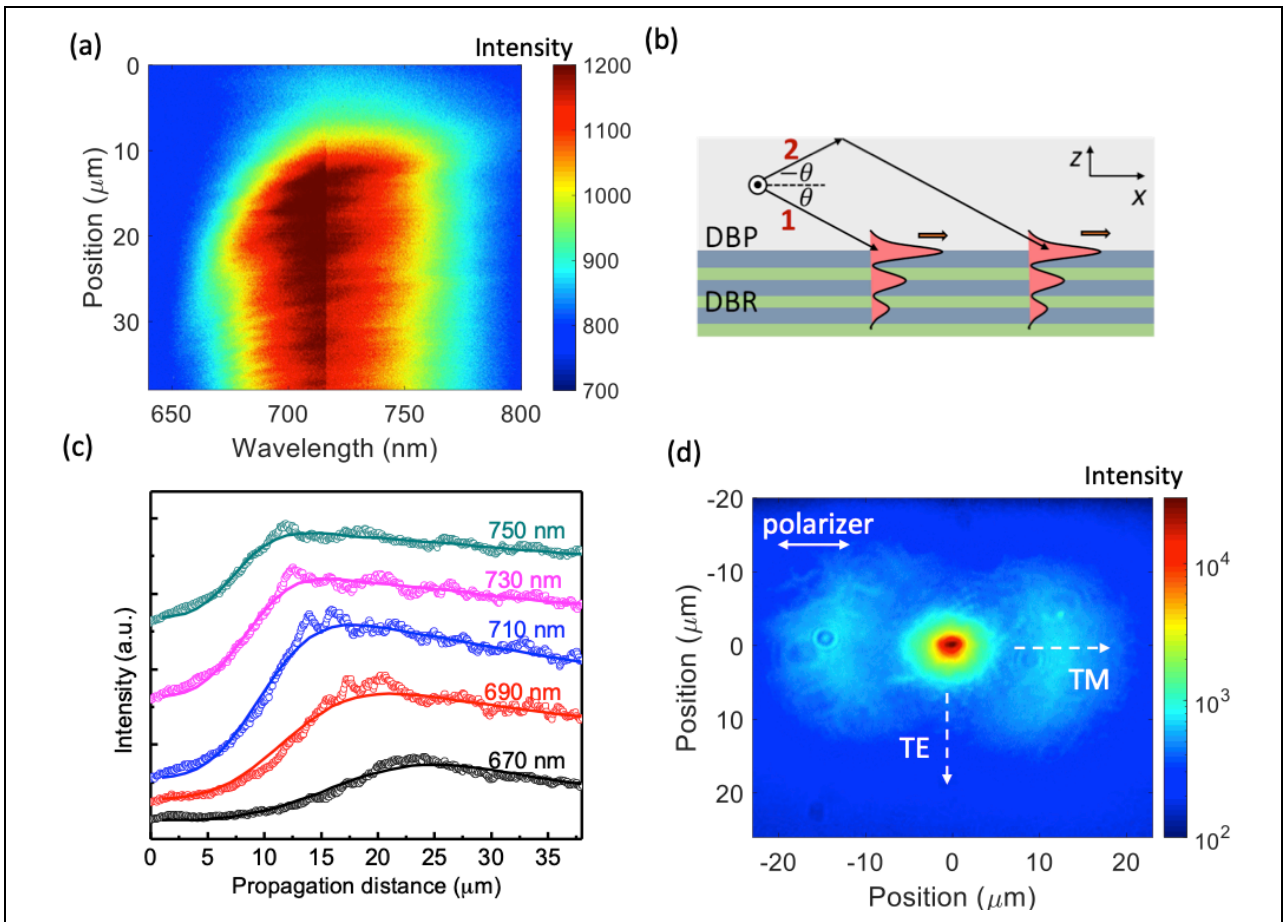

Figure 10.5 Polariton propagation experiment and model. (a) Energy-resolved propagation image. (b) The scheme shows the polariton self-interference model used to fit the propagation profiles in (a). (c) Five propagation profiles at wavelengths of 670, 690, 710, 730 and 750 nm. The calculated distributions (solid lines) fit to the measurement (dashed lines) are shown. (d) PL image showing polariton propagation in the absence of a k-space filter. Emission from the TE and TM modes is separated using a linear polarizer. The horizontal dashed-line indicates propagation of TM guided modes, while the vertical dashed-line indicates propagation direction of TE polaritons. The excitation laser beam was focused at position (0, 0), showing an intense peak from leakage of exciton emission.

$$\varphi = arctan\left(\frac{\sqrt{cos^2\theta - \left(\frac{n_{air}}{n_{DBP}}\right)^2}}{sin\theta}\right) + \frac{4\pi z n_{DBP}}{\lambda cos\theta} \qquad (10.1)$$

where n_{air} and n_{DBP} are the refractive indexes of air and DBP respectively, λ is the wavelength of the exciton radiation, z is the distance of the exciton to the DBP top surface. The first term is the phase delay due to TIR, whereas the second term is the phase delay due to the extra length of path 2.

The Fourier transform of the electric field $E(\vec{r})$ radiated by the DBP exciton is:

$$E(r) = \int E(k)e^{-ikr}d\vec{k} = \int_{-\frac{\pi}{2}+\theta_c}^{\frac{\pi}{2}-\theta_c} E(\theta)\, e^{-ik(cos(\theta)x+sin(\theta)z)}d\theta$$

$$= \int_{0}^{\frac{\pi}{2}-\theta_c} (E(\theta)\, e^{-i(k_x\cdot x+k_z\cdot z)} + E(-\theta)e^{-i(k_x\cdot x-k_z\cdot z)})d\theta, \qquad (10.2)$$

where $\vec{r}$ is the position vector within the DBP film, x is in-plane component of $\vec{r}$, k_x and k_z are the in-plane and out-of-plane components of the wavevector $\vec{k}$, respectively, and $E(\theta)$ and $E(-\theta)$ are electric field of plane waves along path 1 and path 2, respectively.

Following reflection, path 2 has the identical wavevector as path 1, thus the same coupling efficiencies to the polariton mode. Consequently, the amplitudes of the two plane waves are also the same, *viz*. $E(\theta) = E(-\theta)$. The two plane waves each excite a polariton component with the electric field, $E_{LP}(x)$, that is calculated by summing the polariton mode excited by all plane wave components in Eq. 10.2:

$$E_{LP}(x) = \int_{0}^{\frac{\pi}{2}-\theta_c} (E_{LP}(\theta)\, e^{-ik_{x1}\cdot x} + E_{LP}(\theta)e^{-i(k_{x2}\cdot x+\varphi)})d\theta \qquad (10.3)$$

where $E_{LP}(\theta)$ is the electric field amplitudes of polariton modes excited by plane wave, $E(\theta)$, and k_{x1} and k_{x2} are in-plane wavevector components of the polariton excited via path 1 and path 2, respectively.

We assume that $k_{x1,0} = k_{x2,0} = k_{x,0}$ at the excitation spot at $x = 0$. After propagation by a distance x, k_{x1} and k_{x2} scatter into Gaussian distributions $k_{x,0}\pm\mu x$, where μ is the broadening

factor. Polariton mode excited from the same exciton after these two paths will interfere with each other. Thus, the total intensity of polariton emission is given by:

$$I_{LP}(x) = \int_0^d \left(\int_0^{\frac{\pi}{2}-\theta_c} E_{LP}(\theta) e^{-ik_{x1}\cdot x} (1 + e^{-i\Delta k_x \cdot x}\, e^{-i\varphi}) d\theta \right)^2 e^{-\alpha x} dz, \qquad (10.4)$$

where $\Delta k_x = k_{x2} - k_{x1}$, α is the attenuation due to leakage and absorption during propagation, z is the distance from the DBP free surface, and d is the film thickness.

The polariton propagation pattern for a given wavelength is calculated by choosing the polariton components for k_x in the integral of Eq. 10.4. The fitting parameters μ and α used in the fit experimental data in Fig. 10.5c are listed in Table 10.1.

10.4 Discussion

After excitation, photogenerated hot excitons rapidly relax to the exciton reservoir where they subsequently radiatively decay via weakly-coupled localized modes, such as leakage from the USB. At the same time, excitons in the reservoirs populate the LP polariton states via a phonon-assisted recombination and/or radiative pumping. [1] As polaritons have large group velocities, they rapidly propagate in-plane, away from the pumping region. Thus, the lifetime and group velocity in the LP branch determine the spatial extent of the quasiparticle distribution.

To calculate the polariton lifetime, we first fit the dispersion relation in Fig. 10.2a with a coupled-oscillator model outside of the rotating-wave approximation [2] for three DBP vibronic peaks and one BSW photonic oscillator. Figure 10.2a shows the four calculated branches (red dashed lines), where the UP and LP dispersions match the measured data, although absorption from the middle polariton (MP) branches is too weak to be observed. [2] The fitting yields a vacuum Rabi-splitting energy of 480 ± 50 meV for the 0-0 exciton and Bloch surface wave, which is > 20% of the uncoupled 0-0 exciton energy. [3] This ultrastrong-coupled system shows

a high excitonic fraction from 20% to 60% in the LP branch. Considering the lifetimes and fractions of the uncoupled DBP singlet exciton and BSW photon, the calculated polariton lifetime is 500 fs for photonic-like LP and 7 ps for exciton-like LP quasiparticles. We also obtained a group velocity in the LP branch of $3\text{-}5\times10^6$ m/s directly from the measured dispersion relation in Fig. 10.2a.

To understand the polariton propagation pattern, we obtained the wavelength-resolved polariton emission profiles shown in Fig. 10.5a using a k-space filter. For each wavelength, the signal shows a similar halo-like pattern with the polariton emission maximum located tens of micrometers away from the excitation point, followed by decreasing intensity with distance. The size of the hole increases with the wavelength (λ), with an approximate radius of 20 μm at $\lambda =$ 670 nm and 10 μm at $\lambda =$ 750 nm. We attribute the polariton propagation pattern to self-interference between two light paths illustrated in Fig. 10.5b. The polariton mode is either directly excited by the radiation field of an exciton (path 1), or after experiencing TIR (path 2) from the DBP film surface. The phase difference between the two paths results in destructive interference at the pumping site. As the polariton mode propagates beyond the coherence length approximately corresponding to the radius of the halo, the emission intensity rapidly increases to a maximum, followed by an exponential decay due to scattering and non-negligible material absorption.

We calculate the polariton propagation pattern by tracing the pair of plane wave components with the same in-plane momentum. In Fig. 10.5c, we find that the calculation (solid lines) quantitatively fits the halo-like profile observed in wavelength-resolved propagation measurement (data points). The size of the halo is determined by the coherence length of polariton propagation, which is limited by various possible de-coherence mechanisms such as

scattering from grain boundaries, surface roughness, interaction among polaritons and phonons. [4–6] The hole diameter decreases with increasing wavelength as the polariton mode approaches to the air cone at θ_{TIR}. Although relatively intense back scattering was detected as the polariton mode propagates, as shown in Fig. 10.4b, the polariton intensity pattern suggests that the modal coherence length can be as large as 20 μm.

Note that by using the polariton lifetime and group velocity, an effective propagation distance up to 30 μm is obtained based on ballistic transport, [4] which is close to the emission peak position in Fig. 10.3. However, to reconstruct the halo-like propagation pattern, the polariton lifetime or group velocity must significantly decrease beyond the emission peak. This contradicts the results of the selective-area photoluminescence imaging measurement in Fig. 10.4, where the population distribution of LP branch polaritons does not change. Furthermore, we also observe a similar halo-like emission intensity pattern from TM guided modes in the same sample (see Fig. 10.5d) and the high-*k* substrate mode in the control sample without DBR (Fig. 10.6), both of which are weakly coupled to the DBP exciton radiation field. This suggests that particle-like properties such as strong interaction between polaritons is not responsible for the halo-like emission pattern. Instead, the wave-like nature of polaritons leads to the patterns observed in both TM and TE emission. [7]

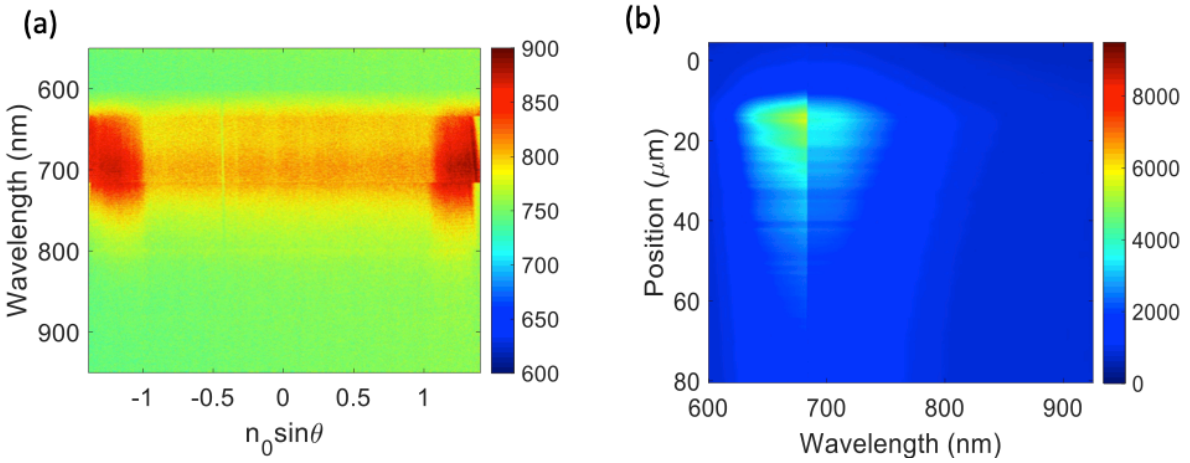

Figure 10.6 Photoluminescence spectra of an uncoupled 20 nm thick DBP film on a silica substrate. (a) TE angular photoluminescence spectrum showing significant emission weakly coupled to the substrate mode. (b) Energy-resolved PL image after filtering the low-k emission within the air cone, showing a halo centered at the pumping position L = 0 μm. Note that the right edge in (a) and vertical cut-line in (b) are measurement artifacts.

10.5 Summary

In conclusion, we have demonstrated exceptionally long-range transport of strongly coupled exciton-polaritons in a one-sided distributed Bragg reflector, which is orders of magnitude larger than expected for excitons in disordered organic semiconductors. Long-range transport is mediated by delocalization and propagation of exciton-polaritons supported by in-plane propagating Bloch surface mode. The observed polariton intensity shows a halo-like pattern which is explained by the self-interference of polariton modes, and whose scale is determined by the surprisingly long coherence length of the polariton mode. Compared with Forster and Dexter-mediated propagation, generation of polaritons provides an alternative path to transport of excitation energy. Furthermore, the simplicity of open dielectric optical structures enables a range of device architectures. For example, the robust nature of polaritons can reduce requirements for use of highly ordered solids, leading to efficient long-range energy harvesting in organic photovoltaics, while also advancing our understanding of polariton physics.

10.6 Reference

[1] D. M. Coles, P. Michetti, C. Clark, W. C. Tsoi, A. M. Adawi, J.-S. Kim, and D. G. Lidzey, Adv. Funct. Mater. **21**, 3691 (2011).

[2] S. Hou, Y. Qu, X. Liu, and S. R. Forrest, Phys. Rev. B **100**, 045410 (2019).

[3] J. C. Wiersum-Osselton, R. A. Middelburg, E. A. M. Beckers, A. J. W. van Tilborgh, P. Y. Zijlker-Jansen, A. Brand, J. G. van der Bom, and M. R. Schipperus, Transfusion **51**, 1278 (2011).

[4] D. M. Myers, S. Mukherjee, J. Beaumariage, D. W. Snoke, M. Steger, L. N. Pfeiffer, and K. West, Phys. Rev. B **98**, 235302 (2018).

[5] S. Aberra Guebrou, C. Symonds, E. Homeyer, J. C. Plenet, Y. N. Gartstein, V. M. Agranovich, and J. Bellessa, Phys. Rev. Lett. **108**, 1 (2012).

[6] K. S. Daskalakis, S. A. Maier, and S. Kéna-Cohen, Phys. Rev. Lett. **115**, 1 (2015).

[7] D. G. Suárez-Forero, V. Ardizzone, S. F. da Silva, M. Reindl, A. Fieramosca, L. Polimeno, M. de Giorgi, L. Dominici, L. N. Pfeiffer, G. Gigli, and others, ArXiv Prepr. ArXiv1908.03472 (2019).

Chapter 11

Future Work and Conclusions

11.1 Future work of organic light-emitting diodes

11.1.1 Light extraction of OLEDs

In Part I, we demonstrated several approaches to enhance light extraction efficiency, all of which are shown to extract waveguide and surface plasmon modes effectively. For bottom-emitting devices, the substrate mode extraction methods, which redirect into air ~80%, at most, of the optical power entering substrates, are becoming a new bottleneck to higher efficiency. This efficiency is limited if we can extract almost all waveguided light into the substrates. For example, in chapter 5, SEMLA shows extraction of 70% of generated optical power into the substrates, which is lowered to only 50% using external microlens arrays

Another important question is whether we can develop a theory [1] for light extraction to understand this problem in a coherent way. It would be helpful to have theoretical guidance for practical ideas. For example, to extract light from the high index to low index region, optical power must be concentrated into a smaller escape cone into air. For all the methods with no energy conversion involved, the optical étendue must be conserved. Therefore, the light extraction must be accompanied by the emission area expansion. For the application to displays, we want higher efficiency without blurring or enlarged pixel images. Theoretical work is able to

answer these questions without considering any specific optical structures. Quite similar to this is the theoretical works on optical concentrators, which have been studied in depth. [2,3] These two questions are so similar that some of the concentration structures can be used for light extraction without modifications. However, different from optical concentration theories, for light extraction we are able to modulate exciton emission profile, which gives us one more degree of freedom.

On the other hand, most existing light extraction methods do not involve energy conversions. Optical absorption and re-emission process can break the limit of étendue, which have been shown successfully in optical concentrators. [4,5] This idea can also be used in light extraction of OLEDs. For example, a thin layer of absorbers, which have a high radiative rate, deposited in the low index material near the interface between the low- and high-index regions, can absorb the optical power through evanescent waves and reemit into the low index region to mitigate the total internal reflection.

Finally, there may be many light extraction designs that are able to reach 80% external quantum efficiency. It is always important to reduce the complexity of the structure and the fabrication process. Due to the wide applications of lighting and displays, the best ideas are the simplest. In recent years, light extraction from OLEDs has been continuously improved. However, the most widely applied technique may not be the one guaranteeing the best device performance, but it must be simple and low-cost.

11.1.2 Purcell effect in OLEDs

The spontaneous emission rate can be enhanced using optical structures built in OLEDs. A shorter exciton lifetime reduces the steady state exciton density and, therefore, reduces inelastic bi-particle interactions which can mitigate the roll-off of device efficiency at a high

drive current and lower the possibility of molecular degradation. In Chapter 2, we showed that enhanced light extraction efficiency and SPPs could shorten the exciton lifetime in conventional device structures. Figure 11.1 shows a calculated exciton lifetime in a bottom-emitting OLED structure. This device uses two metal contacts to introduce a strong cavity and strong SPP coupling. The TiO_2 and MgF_2 pairs further enhance the cavity to achieve high outcoupling efficiency for emission wavelength λ = 450 nm.

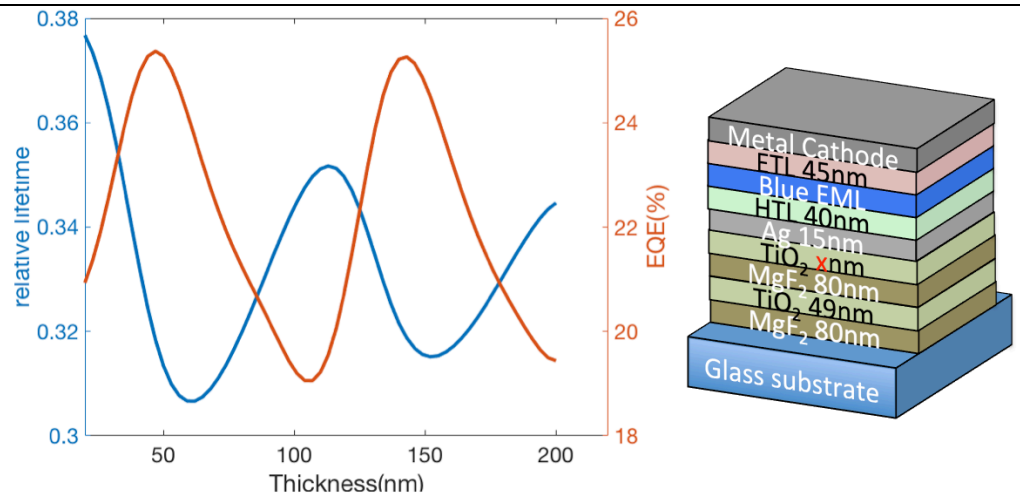

Figure 11.1 Relative exciton lifetimes in bottom-emitting OLED structures. The lifetime minimums are always accompanied with the highest device efficiency.

Intuitively, energy transfer through near-field coupling can shorten the exciton lifetime, which works as a decay channel additional to the far-field radiation, such as Förster transfer and SPP coupling. However, SPPs are non-radiative and lossy. Thus, a process involving near-field energy transfer and re-emission can modulate the exciton lifetime while maintaining high device performance. The re-emitters need to be spatially close to the organic emitters within the Förster radius. The Stoke shift of organic semiconductors prevents the energy transfer back from the re-emitters to the organic excitons. To prevent polaron-exciton quenching, the re-emitters should

not participate in charge transfer. One of candidates to realize this idea is quantum dots surrounded with a barrier.

The similar energy conversion idea appears functional for efficient outcoupling in the previous subsection. According to our calculation in Fig. 2.10 and Fig. 11.1, high outcoupling efficiency always increases the radiative decay. However, the outcoupling structures shown in the first part of this thesis may not able to accelerate the radiative decay, since they simply redirect the optical power already emitted from the excitons. A light extraction strategy leading to shorter exciton lifetime can be realized using energy conversion through Förster transfer.

11.2 Future work of organic strong-coupling regime

The polariton lasing threshold is still higher than that of conventional organic lasers, although in many organic systems, bi-exciton elastic interactions are shown to participate in stimulated scattering. One reason for the unexpected high thresholds is exciton-exciton quenching which starts to occur prior to polariton lasing. How to reduce exciton-exciton quenching while maintaining the nonlinear interactions favoring polariton relaxation is critical to further reduce the polariton lasing thresholds.

Under optical non-resonant pumping, bi-exciton quenching in the exciton reservoir prior to relaxation into polaritons, is a loss channel. Therefore, efficient and lossless relaxation from the exciton reservoir to the lower polariton branch is required. One possible solution is a host-guest system as the active materials. The cavity photons can couple strongly with the excitons on the host, forming polaritons. The host material also absorbs the optical pumping power and transfers the energy to form an exciton reservoir on the guest material. In this way, exciton quenching can be suppressed and the reservoir excitons can efficiently radiative pump the lower polariton branch. A similar idea has already been applied that one of the vibronic peaks of

excitons radiative pumps the polaritons. However, exciton quenching is more severe in the neat film than that in a host-guest system.

Another step for polariton lasers is realization of continuous-wave lasing. Like all organic solid-state lasers, triplet accumulation during extended pumping gradually quenches the laser emission due to triplet absorption. One simple and effective method is to use a triplet manager to sink the triplet in the system. [6] In the polariton microcavity, this idea can be achieved without a manager. If the polariton energy can be pushed lower than that of triplets, the pump photon energy can be chosen below the triplet in the system, preventing triplet generation from the outset. [7,8]

11.3 Conclusion

In conclusion, this thesis presents both practical applications of light emitting devices and offers a fundamental understanding of light-matter interactions. Specifically, the first part of this thesis presents classical models for OLED optical distribution and exciton lifetime, and four different light-extraction structures. The second part investigates the exciton-polariton lasing dynamics in a planar cavity, the coupling strength between excitons and Bloch surface photons, and long-range transport Bloch surface wave polaritons.

11.4 Reference

[1] A. Lenef, A. Piquette, and J. Kelso, ECS J. Solid State Sci. Technol. **7**, R3211 (2018).

[2] E. Yablonovitch, J. Opt. Soc. Am. **72**, 899 (1982).

[3] D. M. Callahan, J. N. Munday, and H. A. Atwater, Nano Lett. **12**, 214 (2012).

[4] M. J. Currie, J. K. Mapel, T. D. Heidel, S. Goffri, and M. A. Baldo, Science (80-.). **321**, 226 LP (2008).

[5] R. E. Alsaigh, R. Bauer, and M. P. J. Lavery, ArXiv Prepr. ArXiv1808.06973 (2018).

[6] Y. Zhang and S. R. Forrest, Phys. Rev. B - Condens. Matter Mater. Phys. **84**, 1 (2011).

[7] D. Polak, R. Jayaprakash, A. Leventis, K. J. Fallon, H. Coulthard, I. I. Petty, J. Anthony, J. Anthony, H. Bronstein, and D. G. Lidzey, ArXiv Prepr. ArXiv1806.09990 (2018).

[8] E. Eizner, L. A. Martínez-Martínez, J. Yuen-Zhou, and S. Kéna-Cohen, ArXiv Prepr. ArXiv1903.09251 (2019).

Appendix

Benchmark of outcoupling methods in this work with other reports

Method	η_{EQE} contr	η_{EQE}	*EF*	Comments*	Ref.
Sub-anode grid	15%	40%	×2.7	• Extracting all waveguide mode • w/ EES extracting all substrate mode	This work
Metallic grid	20%	30%	×1.5	• No SPPs	This work
SEMLA	25%	70%	×2.8	• Extracting all waveguide mode • w/ EES extracting all substrate mode	This work
Nanohole array	30%	78%	×2.6	• Extracting all waveguide mode • A thick ETL • w/ EES extracting all substrate mode	Jeon *et al* [1]
Cavity	25%	63%	×2.5	• Monochromatic • w/ EES extracting all substrate mode	Wang *et al* [2]
Diffuse reflector	15%	37%	×2.5	• No SPPs	Kim *et al* [3]
Low-index grid	15%	34%	×2.3	• w/ an eternal microlens array	Sun *et al* [4]
Sub-anode scattering layer	22%	46%	×2.1	• w/ EES extracting all substrate mode	Chang *et al* [5]
Polymer based scattering layer	18%	30%	×1.7	• Extracting substrate mode	Koh *et al* [6]

*EES is short for external extraction structures

Appendix

Bibliography

[1] S. Jeon, S. Lee, K.-H. Han, H. Shin, K.-H. Kim, J.-H. Jeong, and J.-J. Kim, Adv. Opt. Mater. 1701349 (n.d.).

[2] Z. B. Wang, M. G. Helander, J. Qiu, D. P. Puzzo, M. T. Greiner, Z. M. Hudson, S. Wang, Z. W. Liu, and Z. H. Lu, Nat. Photonics **5**, 753 (2011).

[3] J. Kim, Y. Qu, C. Coburn, and S. R. Forrest, ACS Photonics **5**, 3315 (2018).

[4] Y. Sun and S. R. Forrest, Nat Phot. **2**, 483 (2008).

[5] H.-W. Chang, J. Lee, S. Hofmann, Y. Hyun Kim, L. Müller-Meskamp, B. Lüssem, C.-C. Wu, K. Leo, and M. C. Gather, J. Appl. Phys. **113**, (2013).

[6] T.-W. Koh, J. A. Spechler, K. M. Lee, C. B. Arnold, and B. P. Rand, ACS Photonics **2**, 1366 (2015).